ALMA MATER STUDIORUM · UNIVERSITÀ DI BOLOGNA

Scuola di Scienze
Corso di Laurea Magistrale in Fisica

Quantum Simulation of (1+1)D QED via a Z_n Lattice Gauge Theory

Relatore:
Prof.ssa Elisa Ercolessi

Correlatore:
Prof. Fabio Ortolani

Presentata da:
Giuseppe Magnifico

Sessione II
Anno Accademico 2014/2015

"Give a man a fish, you feed him for a day;
teach a man to fish, you feed him for a lifetime"
To my family.

Abstract

La simulazione di un sistema quantistico complesso rappresenta ancora oggi una sfida estremamente impegnativa a causa degli elevati costi computazionali. La dimensione dello spazio di Hilbert cresce solitamente in modo esponenziale all'aumentare della taglia, rendendo di fatto impossibile una implementazione esatta anche sui più potenti calcolatori. Nel tentativo di superare queste difficoltà, sono stati sviluppati metodi stocastici classici, i quali tuttavia non garantiscono precisione per sistemi fermionici fortemente interagenti o teorie di campo in regimi di densità finita. Di qui, la necessità di un nuovo metodo di simulazione, ovvero la *simulazione quantistica.* L'idea di base è molto semplice: utilizzare un sistema completamente controllabile, chiamato *simulatore quantistico*, per analizzarne un altro meno accessibile. Seguendo tale idea, in questo lavoro di tesi si è utilizzata una teoria di gauge discreta con simmetria Z_n per una simulazione dell'elettrodinamica quantistica in (1+1)D, studiando alcuni fenomeni di attivo interesse di ricerca, come il diagramma di fase o la dinamica di *string-breaking,* che generalmente non sono accessibili mediante simulazioni classiche. Si propone un diagramma di fase del modello caratterizzato dalla presenza di una fase *confinata*, in cui emergono eccitazioni mesoniche ed antimesoniche, cioè stati legati particella-antiparticella, ed una fase *deconfinata.*

Contents

Introduction

"Nature isn't classical, dammit, and if you want to make a simulation of nature, you'd better make it quantum mechanical, and by golly it's a wonderful problem, because it doesn't look so easy." (R. P. Feynman, 1982).

This memorable words are an excellent starting point to approach the world of quantum simulation. Simulating quantum mechanics is still today a very challenging problem: suppose we have a generic quantum system with a Hamiltonian H. In order to perform a numerical analysis, we have to discretize the problem and to implement it on the computer. The amount of memory required for this purpose grows exponentially with the system size N due to the fact that the dimension of the Hilbert space generally increases according to a relation of the form $dim\mathcal{H} \propto a^N$. So, we must store in memory an $a^N \times a^N$-matrix for each observable of the system. This is surely a limit to a static analysis, but it imposes significant limitations especially in calculating the time evolution, which requires an exponentiation of these matrices. To have a concrete idea of the problem, just think that to store in a memory a single state of a spin-1/2 chain of lenght $N = 40$, about 4 terabytes are required.

To circumvent these considerable difficulties in the simulation of large quantum systems, classical stocastic methods, like *Monte Carlo*, have been developed: these algorithms generally evaluate the phase space of the system and the integrals defined on it (partition functions, correlators, mean values of the observables, etc.) in a polynonial time with respect to the number of components of the system. Nevertheless, these methods provide considerable accuracy only when the functions within integrals vary slow and do not change sign. In general, this does not occur in many quantum systems, expecially for strongly correlated fermionic systems in condensed matter physics and for fermionic field theories in finite-density regimes. So, in this sense, classical simulations are severely limited by this problem, which is known in

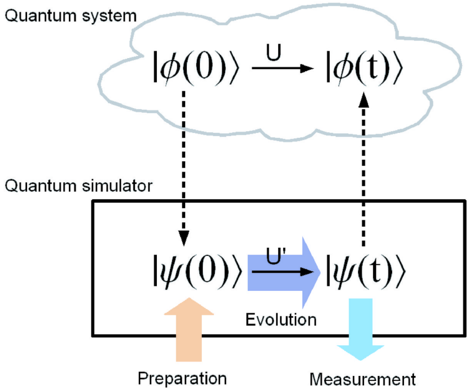

Figure 0.0.1: A quantum system and a corresponding quantum simulator.

literature as *the sign problem.*

From here we can infer the need for a new simulation method, i.e. *quantum simulation*. The basic idea is very simple: to use some fully controllable quantum system, called *quantum simulator*, to emulate and to analyze another less controllable or accessible quantum system. Suppose we have a system with an Hamiltonian H_{sys} and consider the unitary evolution, i.e. $U = e^{-iH_{sys}t/\hbar}$, from an initial state $|\phi(0)\rangle$ to $|\phi(t)\rangle$. In a quantum simulator, being a controllable system, the initial state $|\psi(0)\rangle$ can be prepared, the unitary evolution $U' = e^{-iH_{sim}t/\hbar}$, through a suitable Hamiltonian of the simulator H_{sim}, can be enginereed, and the final state $|\psi(t)\rangle$ can be measured, as shown in Fig. 0.0.1, taken from [12]. The quantum simulator must be built with a mapping of the initial system, so that this latter can be correctly simulated. More precisely, there must be a mapping between $|\phi(0)\rangle \leftrightarrow |\psi(0)\rangle$, $|\phi(t)\rangle \leftrightarrow |\psi(t)\rangle$, $H_{sys} \leftrightarrow H_{sim}$, $U \leftrightarrow U'$, so that a measurement on the simulator provides information about the simulated system. The main advantage of the quantum simulation consists in the fact that the simulator is "experimentally" accessible, while, in many cases, this is not true for the initial system: for example, to get an idea of this, just think that the propagation of sound waves in a two-component BEC has been proposed in [9] for the study of cosmic inflation.

A quantum simulator is generally realized by means of a *synthetic many-body system*, i.e. a system composed of many degrees of freedom, where interactions can be tailored at the microscopic level using external "knobs". These

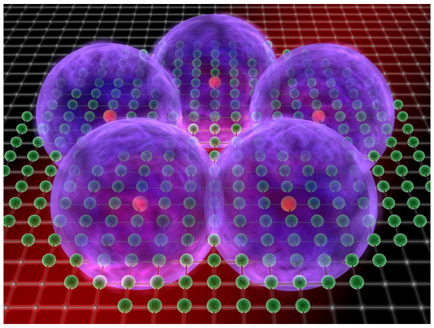

Figure 0.0.2: Rydberg atoms in a quantum gas form ordered structures that are suitable to emulate Hubbard models with different geometries. Image taken from [28].

systems usually consist of ultracold atoms or molecules in optical lattices, superconducting circuits, trapped ions, nuclear spins or photonic systems. Each platform has its own advantages and limitations, and different approaches often tackle with complementary aspects of quantum simulation. However, these realistic setups are finding many applications in many different areas of physics and chemistry [35]. Fig. 0.0.2 shows a pictorial scheme of a quantum simulator with Rydberg atoms.

An important area for the application of the quantum simulation is the study of gauge theories, which, in the context of high-energy physics, play a central role in the dynamics of the Standard Model, or, in condensed matter physics, allow to describe strongly correlated systems (quantum spin liquids, high-T_c superconductors, etc.). Solving a gauge theory is generally very challenging: a representative example is the theory of strong interactions, quantum chromodynamics (QCD). One of the reasons for the difficulties is that a gauge theory, like QCD, generally may present non perturbative effects that are hard to capture with a perturbative or analytical approach. In this framework, it becomes particularly attractive to develop a quantum simulator of a gauge theory.

The conceptual passages for this purpose are the following. First, you have to pass from the considered (continuum) gauge theory to a discrete version of it: this is generally achieved basing on the numerous works developed in the context of lattice gauge theories (LTGs). At this point, it is necessary a suitable formalism to estabilish the connection between the lattice gauge theory and the system that potentially will be able to be used as a quantum simulator: this can be done by using the consolidated quantum link model

(QLM), which, for example, allows an identification of degrees of freedom in terms of spin operators [6]. Precisely in this passage, in the context of (1+1)D QED as Abelian lattice gauge theory, a new Z_n model has been recently proposed for quantum simulations [27]: it allows an interesting mapping to a particular fermionic system, in which the interaction between the Abelian gauge (electromagnetic) field and the matter is achieved through a unitary operator in a very natural way.

This master degree thesis inserts itself in this contest: by identifying a suitable way to numerically engineer the gauge symmetries of the Z_n model, a quantum simulation of the (1+1) QED is performed, studying some important phenomena of active research interest, such as the QED-phase diagram and the dynamics of string breaking.

The outline of this work is the following. In Chapter 1, we start from the study of the Dirac and electromagnetic fields in the classical Lagrangian formulation, showing how it is possible to derive an interacting theory through the introduction of gauge symmetries and how it is consequently possible to obtain a Lagrangian for the classical electrodynamics in the context of Abelian gauge theories. Then, we perform a quantization of the fermionic and the electromagnetic sectors, examining, in particular, the operators that represent, in the quantum formalism, the gauge trasformations. In this way, we get to a coherent formulation of QED.

In Chapter 2, we examine the problems related to the discretization of the QED-Hamiltonian on a lattice, focusing on the *fermion doubling problem* and its possible solutions. In particular, we explain in detail how the use of *staggered fermions* can solve this problem, allowing for the formulation of (1+1)D QED as lattice gauge theory.

In Chapter 3 we present the QLM and the Z_n lattice model, showing how they capture the gauge invariance of our lattice gauge theory with different approaches and how are suitable to quantum simulations due to a general reduction of the degrees of freedom.

In Chapter 4, we consider the Z_n model and propose a way to engineer the gauge symmetries and to constrain the system in the physical (gauge invariant) subspace. So, first by means of a *Mathematica* program and then using the DMRG algorithm, we perform a systematic study of the static phase diagram, of the properties of the ground-state and of some important quantities such as free energy, energetic gap and entropy, highlighting the possible presence of a phase transition.

In Chapter 5, we introduce the symmetries of the model, investigating in

particular a charge-symmetry breaking and proposing an important starting point for further researchs.
Finally in Chapter 6, with a suitable implementation of the *Mathematica* algorithm, we study (with small size of the system) the real-time dynamics of string-breaking, which usually can not be accessed using classical lattice simulations due to effects of the sign problem. We stress that the implementation of the dynamics at numerical level, which has been performed, may represent a "platform" for the study of other interesting non-perturbative effects of (1+1)QED.

Chapter 1

Introduction to Abelian gauge theories

The starting point of this chapter is the treatment of classical field theory for the Dirac and the electromagnetic fields. Therefore, we focus on the connection between the fermionic theory and the $U(1)$ Abelian gauge theory with the introduction of local gauge trasformations and covariant derivatives. Finally, the quantization of fields is presented.

1.1 Basic definitions and conventions

The physical space on which the fields are defined is the Minkowski space $\mathcal{M}$: it is a four dimensional space in which the three spatial dimensions are combined with a single dimension of time to form a four-dimensional manifold (spacetime). We impose $c = \hbar = e = 1$.
Each physical event is uniquely identified by a suitable four-vector

$$\underline{\mathbf{x}} = (x^0, \mathbf{x}) \tag{1.1.1}$$

where x^0 is the temporal coordinate, $\mathbf{x} = (x^1, x^2, x^3)$ the spatial three dimensional vector. These coordinates both spatial and temporal are called "contravariant" and are indicated by x^μ with Greek index $\mu = 0, 1, 2, 3$. Conversely, a Latin index i runs over spatial components 1, 2, 3. The metric tensor is conventionally

$$\eta_{\mu\nu} = \begin{bmatrix} 1 & 0 & 0 & 0 \\ 0 & -1 & 0 & 0 \\ 0 & 0 & -1 & 0 \\ 0 & 0 & 0 & -1 \end{bmatrix} \tag{1.1.2}$$

where the spatial part is negative. We define the “covariant” coordinates of four-vector $\underline{\mathbf{x}}$ as

$$x_\mu = \eta_{\mu\nu} x^\nu = \begin{cases} x_0 = x^0 \\ x_i = -x^i \end{cases} . \tag{1.1.3}$$

Consequently, the scalar product of two four-vector $\underline{\mathbf{a}}$ and $\underline{\mathbf{b}}$ is

$$\underline{\mathbf{a}} \cdot \underline{\mathbf{b}} = a^\mu \eta_{\mu\nu} b^\nu = a^\mu b_\mu = a^0 b^0 - \sum_i a^i b^i \tag{1.1.4}$$

and the squared norm of $\underline{\mathbf{a}}$

$$\|\underline{\mathbf{a}}\|^2 = a^\mu \eta_{\mu\nu} a^\nu = a^\mu a_\mu = (a^0)^2 - \sum_i (a^i)^2. \tag{1.1.5}$$

The derivates of a function in the Minkowski space are compacted in a particular four-vector

$$\partial^\mu \equiv \frac{\partial}{\partial x^\mu} = (\frac{\partial}{\partial x^0}, \nabla). \tag{1.1.6}$$

In the Minkowski space there is a specific trasformation law for the coordinates

$$x^\mu \to (x^\mu)' = \Lambda^\mu_\nu x^\nu \tag{1.1.7}$$

where $\Lambda^\mu_\nu \in SO^+(1,3)$, the proper and orthochronous Lorentz group ($det\mathit{\Lambda} = 1,\ \mathit{\Lambda}^0_0 \geq 1$). Each element of this group is a Lorentz trasformation, i.e. a composition of a spatial rotation and a boost. Therefore it is identified by six parameters: $\theta = (\theta_1, \theta_2, \theta_3)$ for the spatial rotation, $\beta = (\beta_1, \beta_2, \beta_3)$ for the boost.

A classical relativistic field consists of a collection of real or complex functions defined on the Minkowski space $\mathcal{M}$

$$\mathit{\Upsilon}(x) = \begin{cases} \mathit{\Upsilon}_1(x) \\ \mathit{\Upsilon}_2(x) \\ \ldots \end{cases}$$

with a well defined trasformation law under the action of $SO^+(1,3)$. This law depends on the representation of the Lorentz group for which the field is defined.

1.2 Free Dirac field

The Lorentz group has two important, irriducible, two-dimensional representations $\tau_{\frac{1}{2}0}$ and $\tau_{0\frac{1}{2}}$ which can be realized by means of the group of complex 2×2 matrices of unit determinant $SL(2,C)$ [32]. The matrices related to $\tau_{\frac{1}{2}0}$ act upon the left Weyl's two-component spinors ψ_L, while the matrices related to $\tau_{0\frac{1}{2}}$ act upon the right Weyl's two-component spinors ψ_R.
These matrices have the following exponential form

$$\Lambda_L = \exp\{(-i\theta_k - \beta_k)\frac{1}{2}\sigma_k\} \tag{1.2.1}$$

$$\Lambda_R = \exp\{(-i\theta_k + \beta_k)\frac{1}{2}\sigma_k\} \tag{1.2.2}$$

where σ_k are the Pauli matrices (a set of three 2×2 complex matrices which are Hermitian and unitary):

$$\sigma_1 = \begin{bmatrix} 0 & 1 \\ 1 & 0 \end{bmatrix} \; \sigma_2 = \begin{bmatrix} 0 & -i \\ i & 0 \end{bmatrix} \; \sigma_3 = \begin{bmatrix} 1 & 0 \\ 0 & -1 \end{bmatrix}. \tag{1.2.3}$$

These matrices are directly connected to generators of $\tau_{\frac{1}{2}0}$ and $\tau_{0\frac{1}{2}}$ representations, as seen respectively in (1.2.1) and (1.2.2). Notice that

$$[\sigma_j, \sigma_k] = 2i\varepsilon_{jkl}\sigma_l. \tag{1.2.4}$$

From (1.2.4) we can easily understand that the generators in (1.2.1) and (1.2.2) satisfy the general propriety $[I_a, I_b] = C_{abc}I_c$ with a particular structure constants.
The left and right Weyl's two-component spinors trasform according to

$$\psi_L^{'} = \Lambda_L\psi_L \tag{1.2.5}$$

$$\psi_R^{'} = \Lambda_R\psi_R. \tag{1.2.6}$$

The Weyl's spinors describe spin-$\frac{1}{2}$ particles with different helicity: it is a physical quantity defined as the projection of the spin onto the direction of

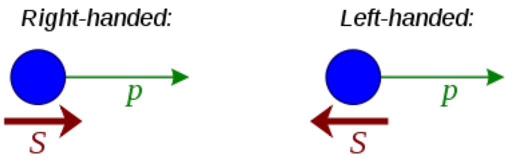

Figure 1.2.1: Left-handed and right-handed particles.

momentum. Left-handed spinor have $h = -\frac{1}{2}$, right-handed $h = \frac{1}{2}$ (Fig. 1.2.1).
To describe spin-$\frac{1}{2}$ particles with four deegres of freedom $s = \pm\frac{1}{2}$ and $h = \pm\frac{1}{2}$ (i.e. electrons, positrons) and to guarantee parity preservation (all massive fermions are known to obey parity conservation unlike Weyl's two-component spinors) we introduce the four-components Dirac spinors [33] in the Weyl or chiral representation:

$$\psi = \begin{bmatrix} \psi_L \\ \psi_R \end{bmatrix} = \begin{bmatrix} \psi_{L1} \\ \psi_{L2} \\ \psi_{R1} \\ \psi_{R2} \end{bmatrix}. \tag{1.2.7}$$

Starting from the matrices (1.2.3), we can define a new set of 4×4 matrices that correctly acts upon Dirac spinors (1.2.7) in this representation

$$\gamma^0 = \begin{bmatrix} \mathbf{0} & \mathbf{1} \\ \mathbf{1} & \mathbf{0} \end{bmatrix} \quad \gamma^i = \begin{bmatrix} \mathbf{0} & \sigma_i \\ -\sigma_i & \mathbf{0} \end{bmatrix}. \tag{1.2.8}$$

These matrices allow to obtain the Dirac equation [8], which describes the evolution of spin-$\frac{1}{2}$ particles with mass m:

$$(i\gamma^\mu \partial_\mu - m)\psi(x) = 0. \tag{1.2.9}$$

Equation (1.2.9) can also be obatined from the Lagrangian density [21]

$$\mathcal{L}_{\mathcal{D}} = \overline{\psi}(i\gamma^\mu \partial_\mu - m)\psi \tag{1.2.10}$$

with $\overline{\psi} = \psi^\dagger \gamma^0$.
The Dirac equation has four indipendent solutions

$$\psi(x) = u_r(p)e^{-ipx} = u_r(p)e^{-iEx^0 + i\mathbf{p}\mathbf{x}} \tag{1.2.11}$$

$$\psi(x) = v_r(p)e^{+ipx} = v_r(p)e^{+iEx^0 - i\mathbf{px}} \tag{1.2.12}$$

with $r = 1, 2$, $u_r(p)$, $v_r(p)$ costant spinors, $p = (E, \mathbf{p})$ the four-momentum. (1.2.11) and (1.2.12) are respectively plane-wawe solutions with positive and negative energy, i.e. particles, antiparticles. The two-fold degeneracies for a given momentum, $r = 1, 2$, correspond to solutions with opposite spin orientations along a reference axis.
Therefore, the most general solution of the Dirac equation is [21]

$$\psi(x) = \sum_{\mathbf{p},r}[c_{\mathbf{p},r}u_r(p)e^{-i\mathbf{px}} + d^*_{\mathbf{p},r}v_r(p)e^{i\mathbf{px}}]|_{p^0=E_\mathbf{p}} \tag{1.2.13}$$

where $p^0 = E_\mathbf{p} = (\mathbf{p^2} + m^2)$. $c_{\mathbf{p},r}$ and $d_{\mathbf{p},r}$ are anti-commuting numbers [32], also named Grassmann numbers, which have the following properties ($\forall r, s = 1, 2;\ \mathbf{p}, \mathbf{q} \in \mathrm{R}^3$):

$$\{c_{\mathbf{p},r}, c_{\mathbf{q},s}\} = \{c^*_{\mathbf{p},r}, c^*_{\mathbf{q},s}\} = 0 \Rightarrow (c_{\mathbf{p},r})^2 = (c^*_{\mathbf{p},r})^2 = 0 \tag{1.2.14}$$

$$\{d_{\mathbf{p},r}, d_{\mathbf{q},s}\} = \{d^*_{\mathbf{p},r}, d^*_{\mathbf{q},s}\} = 0 \Rightarrow (d_{\mathbf{p},r})^2 = (d^*_{\mathbf{p},r})^2 = 0. \tag{1.2.15}$$

$$\{c_{\mathbf{p},r}, d_{\mathbf{q},s}\} = \{c_{\mathbf{p},r}, d^*_{\mathbf{q},s}\} = \{c^*_{\mathbf{p},r}, d_{\mathbf{q},s}\} = \{c^*_{\mathbf{p},r}, d^*_{\mathbf{q},s}\} = 0 \tag{1.2.16}$$

From this equations, we can easily notice that the classical relativistic Dirac spinors satisfy the following relations:

$$\{\psi(x), \psi(y)\} = \{\psi^\dagger(x), \psi^\dagger(y)\} = \{\psi(x), \psi^\dagger(y)\} = 0. \tag{1.2.17}$$

1.3 Free electromagnetic field

We introduce the four-vector potential

$$\underline{\mathbf{A}} = (\phi, \mathbf{A}) = A^\mu \tag{1.3.1}$$

where ϕ is the electric potential and $\mathbf{A}$ the vector potential such that the electric and magnetic fields result

$$\begin{aligned} \mathbf{E} &= -\nabla\phi - \frac{\partial \mathbf{A}}{\partial t} && (1.3.2) \\ \mathbf{B} &= \nabla \times \mathbf{A}. && (1.3.3) \end{aligned}$$

Starting from the A^μ, we can define the electromagnetic field tensor

$$F^{\mu\nu} = \partial^\mu A^\nu - \partial^\nu A^\mu. \tag{1.3.4}$$

It is antisymmetric, thus it has six independent components, i.e. the three components of **E** and the three of **B** [4].
The electomagnetic field is uniquely determined by the tensor $F^{\mu\nu}$: the relations (1.3.1) and (1.3.3) can be written as

$$\begin{aligned} F^{i0} &= E^i & (1.3.5) \\ F^{ij} &= -\varepsilon^{ijk}B^k. & (1.3.6) \end{aligned}$$

An important property of the electromagnetic tensor is the gauge-invariance: if we define a gauge trasformation of the potential A^μ as follows

$$(A^\mu)' = A^\mu - \partial^\mu\varphi(x) \tag{1.3.7}$$

where $\varphi(x)$ is a smooth function, we notice that

$$(F^{\mu\nu})' = F^{\mu\nu}. \tag{1.3.8}$$

The Lagrangian density for the free electromagnetic field is

$$\mathcal{L}_{\text{em}} = -\frac{1}{4}F_{\mu\nu}F^{\mu\nu}. \tag{1.3.9}$$

in which the dynamic variables are the four components A^μ.

1.4 Local gauge symmetry and interaction

A way to write interaction terms in the Lagrangian formalism is the request of local symmetries (gauge symmetries): in fact, by promoting a global symmetry of the Lagrangian, which describes a generic field, into a local symmetry (i.e. symmetry under a space-time dependent trasformation), it is possible to introduce a gauge field as a dynamical variable and to derive in a natural way interaction terms between the original field and the gauge field.
We notice that under $U(1)$ global trasformations with a real number α

$$\psi^{'}(x) = \psi(x)e^{i\alpha} \tag{1.4.1}$$

the Lagrangian density (1.2.10) is invariant:

$$\mathcal{L}_{\mathcal{D}}^{'} = \mathcal{L}_{\mathcal{D}}. \tag{1.4.2}$$

Thus, the free Dirac field exhibits a global $U(1)$ symmetry.
We now impose that this symmetry is local by definition of a parameter as a real function of the Minkowski space $\alpha = \alpha(x)$. Therefore, the local $U(1)$ trasformation acts on fields as

$$\psi^{'}(x) = \psi(x)e^{i\alpha(x)}. \tag{1.4.3}$$

The mass term in the Lagrangian density (1.2.10) is invariant, while the kinetic term is not. In fact, we have

$$(\overline{\psi}i\gamma^{\mu}\partial_{\mu}\psi)^{'} = \overline{\psi}\gamma^{\mu}\partial_{\mu}\psi + i\overline{\psi}\gamma^{\mu}\psi\partial_{\mu}\alpha(x) \tag{1.4.4}$$

where there is an additional term due to the dependence of trasformation (1.4.1) on the spacetime-point x. Therefore, we must properly extend the Lagrangian density to restore the symmetry. We introduce the covariant derivative as

$$D_{\mu} = \partial_{\mu} + iA_{\mu} \tag{1.4.5}$$

where A_{μ} is the gauge field which coincides with the four-vector potential (1.3.1). Then, if we operate a local gauge trasformation as follows

$$\begin{aligned} \psi'(x) &= \psi(x)e^{i\alpha(x)} \\ A^{'}_{\mu} &= A_{\mu} - \partial_{\mu}\alpha(x) \\ D^{'}_{\mu} &= \partial_{\mu} + i(A_{\mu} - \partial_{\mu}\alpha(x)) \end{aligned} \tag{1.4.6}$$

we have that

$$(\overline{\psi}(x)i\gamma^{\mu}D_{\mu}\psi(x))' = \overline{\psi}(x)i\gamma^{\mu}D_{\mu}\psi(x). \tag{1.4.7}$$

Therefore, we can replace the derivative ∂_{μ} in the kinetic term of (1.2.10) with the covariant derivative D_{μ} to obtain a local gauge symmetry. In this way, we introduce de facto an interaction between the two fields due to the presence of A_{μ} in the definition (1.4.5). This new kinetic term combined with the Lagrangian density of electromagnetic free field (1.3.9) gives us the complete Lagrangian density:

$$\mathcal{L} = \overline{\psi}(x)(i\gamma^{\mu}D_{\mu} - m)\psi(x) - \frac{1}{4}F_{\mu\nu}F^{\mu\nu}. \tag{1.4.8}$$

1.5 The comparator U

We have seen in (1.4.4) that the kinetic term including derivatives is not gauge invariant under the local trasformation (1.4.1). This is not a simple mathematical "consequence", but it follows from a general geometrical property. The derivative of $\psi(x)$ in the direction of a generic four-vector η^μ is defined as

$$\partial_\eta \psi(x) = \eta^\mu \partial_\mu \psi(x) = \lim_{\epsilon \to 0} \frac{1}{\epsilon} \left[\psi(x + \epsilon\eta) - \psi(x) \right]. \tag{1.5.1}$$

The two fields $\psi(x + \epsilon n)$, $\psi(x)$ are calculated at different points, so they have completely different transformations. Therefore, the quantity $\partial_\mu \psi$ has no simple trasformation law and no useful geometric interpretation [29].
To compensate for this phase-difference between the two points, we can introduce a quantity, called the comparator, that depends on the two points and trasforms under (1.4.1) as:

$$U^{'}(x, y) = e^{i\alpha(x)} U(x, y) e^{-i\alpha(y)} \tag{1.5.2}$$

We assume that $U(x, y)$ is unitary, therefore $U(x, y) = e^{i\phi(x,y)}$, and $U(x, x) = 1$ when $y = x$. The introduction of this comparator has a significant effect: the quantities $U(x, y)\psi(y)$ and $\psi(y)$ trasform in the same way, so they can be subtracted from each other respecting the local symmetry. Then, we define a new derivative with this difference (setting $y = x + \epsilon\eta$), called the covariant derivative [29]:

$$D_\eta \psi(x) = \lim_{\epsilon \to 0} \frac{1}{\epsilon} [U(x, x + \epsilon\eta)\psi(x + \epsilon\eta) - \psi(x)]. \tag{1.5.3}$$

It can be shown that the this is a gauge-covariant quantity:

$$\begin{aligned} \left(D_\eta \psi(x)\right)^{'} &= \lim_{\epsilon \to 0} \frac{1}{\epsilon} [U(x, x + \epsilon\eta)\psi(x + \epsilon\eta) e^{i\alpha(x)} - \psi(x) e^{i\alpha(x)}] \\ &= e^{i\alpha(x)} D_\eta \psi(x) \end{aligned} \tag{1.5.4}$$

i.e. it transforms like a spinor.
We can now analyze the properties of this covariant derivative and its connection with the previous definition (1.4.5).
Assuming that the phase $\phi(x, y)$ is a regular function, we can expand in ϵ the comparator $U(x, y)$:

$$U(x, x + \epsilon\eta) = U(x, x) + \epsilon\eta^\mu \frac{\partial U}{\partial y^\mu}|_{y=x} + \mathcal{O}(\epsilon^2) \tag{1.5.5}$$

whence

$$U(x, x + \epsilon\eta) = 1 + i\epsilon\eta^{\mu} V_{\mu} + \mathcal{O}(\epsilon^2) \tag{1.5.6}$$

where $V_{\mu} = \frac{\partial\phi(x,y)}{\partial y^{\mu}}|_{y=x}$. If we apply the trasformation law (1.5.2)

$$\begin{aligned} U^{'}(x, x + \epsilon\eta) &\simeq e^{i\alpha(x)}(1 + i\epsilon\eta^{\mu}V_{\mu})e^{-i\alpha(x+\epsilon\eta)} \\ &\simeq e^{i\alpha(x)}(1 + i\epsilon\eta^{\mu}V_{\mu})(1 - i\epsilon\eta^{\mu}\partial_{\mu}\alpha(x))e^{-i\alpha(x)} \\ &= 1 + i\epsilon\eta^{\mu}(V_{\mu} - \partial_{\mu}\alpha(x)) \end{aligned}$$

we notice immediatly that V_{μ} must have the same trasformation law of A_{μ}. So, we can identify it with the four-vector potential (1.3.1): this is significant because we have defined the covariant derivative (1.5.3) in a very general way and now we find the four-vector potential as a consequence of the comparator trasformation law (1.5.2).

Starting from this results, we can now evaluate the definition (1.5.3)

$$\begin{aligned} \eta^{\mu} D_{\mu}\psi(x) &= \lim_{\epsilon\to 0} \frac{1}{\epsilon}[(1 + i\epsilon\eta^{\mu}A_{\mu})\psi(x + \epsilon\eta) - \psi(x)] \\ &= \eta^{\mu}(\partial_{\mu} + iA_{\mu})\psi(x). \end{aligned} \tag{1.5.7}$$

from which it follows that this "new" covariant derivative coincides with the covariant derivative defined in (1.4.5). This is an important result because it allows us to understand from a new point of view that the request of local symmetry implies a general geometric construction of the covariant derivative and the very existence of the vector field A_{μ}. This is the essence of a gauge theory.

At this point it is useful to introduce an explicit form of the comparator [38] which respects all its properties, in particular its trasformation law:

$$U(x, y) = \exp\left\{ i \int_{x}^{y} dx^{\mu} A_{\mu} \right\}. \tag{1.5.8}$$

Starting from this expression, we can analyze some important properties: first we note that $U(x, x)$ is gauge invariant, then we take two unit vectors in the Minkowski space:

$$\underline{\mathbf{v_1}} = (0, 1, 0, 0) \tag{1.5.9}$$

$$\underline{\mathbf{v_2}} = (0, 0, 1, 0). \tag{1.5.10}$$

Therefore, we value the comparator along a square closed path with side ϵ (a plaquette) from initial point x:

$$\mathbf{U}(x) = U(x, x_1)U(x_1, x_2)U(x_2, x_3)U(x_3, x) \tag{1.5.11}$$

where $x_1 = x + \epsilon v_1$, $x_2 = x + \epsilon v_1 + \epsilon v_2$, $x_3 = x + \epsilon v_2$. It can easily show [29] that $\mathbf{U}(x)$ is a gauge invariant quantity and can be written as

$$\begin{aligned} \mathbf{U}(x) &= 1 + i\epsilon^2[\partial_1 A_2(x) - \partial_2 A_1(x)] + \mathcal{O}(\epsilon^3) \\ &= 1 + i\epsilon^2 B_3(x) + \mathcal{O}(\epsilon^3) \end{aligned} \tag{1.5.12}$$

where in the second term appears the flux of the third component of the magnetic field across the above infinitesimal plaquette of area ϵ^2. This formula allows us to understand that, since $\mathbf{U}(x)$ is gauge invariant, also the quantity $\partial_1 A_2(x) - \partial_2 A_1(x)$ must have the same property. If we repeat the previous reasoning with other directions in the Minkowski space, we notice immediately that all the components of the tensor $F_{\mu\nu} = \partial_\mu A_\nu - \partial_\nu A_\mu$ must be gauge invariant. This is the geometrical origin of the electromagnetic field tensor (1.3.4) in the view of a gauge theory.

1.6 Quantization of the Dirac field

In the Lagrangian formulation of the free Dirac field, the spinor $\psi(x)$ is the dynamical variable. Starting from the Lagrangian density (1.2.10), the conjugate momentum results

$$\Omega_\alpha(x) = \frac{\partial \mathcal{L}}{\partial(\partial_0 \psi_\alpha(x))} = i\psi^\dagger_\alpha(x) \tag{1.6.1}$$

in which the index $\alpha = 1L, 2L, 1R, 2R$ identifies the spinorial components. The canonical quantization is achieved by promoting the classical spinorial fields $\psi(x)$ and $\psi^\dagger(x)$ to fields operators and, due to the nature of the Grassman algebra of the classical solutions of the Dirac equation, the classical relations (1.2.17) to suitable egual-time anticommutation relations:

$$\{\hat{\psi}_\alpha(x^0, \mathbf{x}), \hat{\psi}^\dagger_\beta(x^0, \mathbf{y})\} = \delta_{\alpha,\beta}\delta^{(3)}(\mathbf{x} - \mathbf{y}) \tag{1.6.2}$$

$$\begin{aligned} \{\hat{\psi}_\alpha(x^0, \mathbf{x}), \hat{\psi}_\beta(x^0, \mathbf{y})\} &= 0 \\ \{\hat{\psi}^\dagger_\alpha(x^0, \mathbf{x}), \hat{\psi}^\dagger_\beta(x^0, \mathbf{y})\} &= 0 \end{aligned} \tag{1.6.3}$$

From these equations, we obtain the usual anticommutation relation of conjugate variables:

$$\{\hat{\psi}_\alpha(x^0,\mathbf{x}),\hat{\Omega}_\beta(x^0,\mathbf{y})\} = i\delta_{\alpha,\beta}\delta^{(3)}(\mathbf{x}-\mathbf{y}). \tag{1.6.4}$$

In the expansion (1.2.13) of the Dirac field, we have now a set of operators, $\hat{c}_{\mathbf{p},r}$ and $\hat{d}_{\mathbf{p},r}$, with fermionc feature:

$$\{\hat{c}_{\mathbf{p},r},\hat{c}^\dagger_{\mathbf{q},s}\} = \delta_{r,s}\delta^{(3)}(\mathbf{p}-\mathbf{q}) \tag{1.6.5}$$

$$\{\hat{d}_{\mathbf{p},r},\hat{d}^\dagger_{\mathbf{q},s}\} = \delta_{r,s}\delta^{(3)}(\mathbf{p}-\mathbf{q}) \tag{1.6.6}$$

$$all\, the\, other\, anticommutators\, vanish. \tag{1.6.7}$$

In the formalism of the canonical quantization, it results that the Hamiltonian density operator of the Dirac field has the following form:

$$\hat{H} = \hat{\overline{\psi}}(-i\gamma^i\partial_i + m)\hat{\psi}. \tag{1.6.8}$$

The operators $\hat{c}_{\mathbf{p},r}$ and $\hat{d}_{\mathbf{p},r}$ allow us to define the Hilbert space $\mathcal{H}_\mathcal{D}$ on which this Hamiltonian is defined: it is a Fock space, i.e. the direct sum of tensor products of copies of a single-particle Hilbert space H.

$$\mathcal{H}_\mathcal{D} = \bigoplus_{n=0}^{\infty} A\mathrm{H}^{\otimes n} = \mathrm{H}_0 \oplus \mathrm{H} \oplus A(\mathrm{H}\otimes\mathrm{H}) \oplus A(\mathrm{H}\otimes\mathrm{H}\otimes\mathrm{H}) \oplus .... \tag{1.6.9}$$

in which H_0 is the quantum space state with zero particles and A is the operator which antisymmetrizes the tensor products, due to the fermionic nature of the particles. In this space, first we define a vacuum state $|0\rangle$ as follows:

$$\hat{c}_{\mathbf{p},r}\,|0\rangle = 0 \quad \forall\,\mathbf{p},s \tag{1.6.10}$$

$$\hat{d}_{\mathbf{p},r}\,|0\rangle = 0 \tag{1.6.11}$$

then, we can build a one particle/antiparticle states as

$$|\mathbf{p},r,-\rangle = \hat{c}^\dagger_{\mathbf{p},r}\,|0\rangle \tag{1.6.12}$$

$$|\mathbf{p},r,+\rangle = \hat{d}^\dagger_{\mathbf{p},r}\,|0\rangle \tag{1.6.13}$$

in which the sign refers to the electric charge of particle/antiparticle. Similarly, we can build a generic antisymmetric state with a particles and b antiparticles as

$$|\phi\rangle = \prod_{m=1}^{a}\prod_{n=1}^{b} \hat{c}^{\dagger}_{\mathbf{p}_m,r_m}\hat{d}^{\dagger}_{\mathbf{p}_n,r_n}|0\rangle\,. \tag{1.6.14}$$

We have seen in (1.4.2) that the classical Lagrangian density of the Dirac field is invariant under global $U(1)$ trasformation. In the quantum formalism, this is translated into a symmetry of the Hamiltonian density (1.6.8) under a trasformation performed by a suitable operator. If we define the operator

$$\hat{T}(x^0,\alpha(x)) = \exp\left\{i\int d^3\mathbf{x}\,\alpha(x)\hat{\psi}^{\dagger}(x^0,\mathbf{x})\hat{\psi}(x^0,\mathbf{x})\right\} \tag{1.6.15}$$

it can easily show [26] that it trasforms the spinor as

$$\hat{T}^{\dagger}(y^0)\hat{\psi}(y)\hat{T}(y^0) = \hat{\psi}(y)e^{i\alpha(y)} \tag{1.6.16}$$

which coincides with the local $U(1)$ trasformation of the quantum Dirac field. We notice that it results

$$\left[\hat{H},\hat{T}\right] = 0 \rightarrow \hat{T}^{\dagger}\hat{H}\hat{T} = \hat{H} \tag{1.6.17}$$

only if α is a constant, rediscovering the global $U(1)$ symmetry of the Dirac theory.

1.7 Quantization of the electromagnetic field

When we try to perform the canonical quantization of the free electromagnetic field, we encounter a problem: starting from the Lagrangian density (1.3.9) and proceeding to determine the conjugate momenta of the four variables A_μ, we find

$$\Pi_\mu = \frac{\partial\mathcal{L}_{em}}{\partial(\partial_0 A^\mu)} \Rightarrow \left\{\begin{array}{c}\Pi_0 = 0\\ \Pi_i = -E_i\end{array}\right. \tag{1.7.1}$$

in which the momentum Π_0 is identically zero: it shows that the evolution of A_0 is not fixed by any dinamical law and is arbitrary, as we can modify it by a gauge trasformation. Indeed it is always possible to find a gauge trasformation with a function $\varphi(x)$ such that $\partial_0\varphi(x) = A_0$. In this way, the new dynamic variables result

$$A_0 = 0 \quad A_i = A_i - \partial_i\varphi(x). \tag{1.7.2}$$

This condition does not completely eliminate the gauge freedom: a residual set of gauge time-indipendent trasformations are still allowed.
Now we can apply the canonical formalism by promoting A_i and Π_i to field (conjugate) operators, such that at equal time it results

$$\left[\hat{A}_i(x^0,\mathbf{x}), \hat{\Pi}_j(x^0,\mathbf{y})\right] = i\delta_{i,j}\delta^{(3)}(\mathbf{x}-\mathbf{y}) \tag{1.7.3}$$

or, in terms of the electric field:

$$\left[\hat{A}_i(x^0,\mathbf{x}), \hat{E}_j(x^0,\mathbf{y})\right] = -i\delta_{i,j}\delta^{(3)}(\mathbf{x}-\mathbf{y}) \tag{1.7.4}$$

In this gauge, the Hamiltonian density operator of the free electromagnetic field can be written in the form

$$\hat{H} = \frac{1}{2}(\hat{\mathbf{E}}^2 + \hat{\mathbf{B}}^2). \tag{1.7.5}$$

Let us now determine the Hilbert space of the quantum electromagnetic field, $\mathcal{H}_{\text{el}}$: being $\hat{A}_i$ and $\hat{E}_i$ conjugate operators (such as $\hat{x}$ and $\hat{p}$ in the quantum mechanics), we can consider a space of states $|\Psi\rangle$ with wave functions which, in the $\hat{A}$-representation, have the form $\Psi(\{A_i\})$. In this representation, the operator $\hat{A}_i(x^0,\mathbf{x})$ is multiplicative, while the electric field becomes the differential operator [10]

$$\hat{E}_i(x^0,\mathbf{x}) = i\frac{\delta}{\delta\hat{A}_i(x^0,\mathbf{x})}. \tag{1.7.6}$$

We define now an operator which performs the gauge trasformations with a time-indipendent function $\varphi(\mathbf{z})$:

$$\hat{R}(\varphi(\mathbf{z})) = \exp\left\{-i\int d^3\mathbf{z}\,\varphi(\mathbf{z})\nabla\cdot\hat{\mathbf{E}}(x^0,\mathbf{z})\right\}. \tag{1.7.7}$$

It can be easily shown [10] that

$$\hat{R}^\dagger(\varphi(\mathbf{z}))\hat{A}_i(x^0,\mathbf{x})\hat{R}(\varphi(\mathbf{z})) = \hat{A}_i(x^0,\mathbf{x}) - \partial_i\varphi(\mathbf{z}) \tag{1.7.8}$$

recovering the trasformation (1.7.2). Due to the gauge symmetry, this trasformation does not change the physics of the electromagnetic field and its states (i.e. states that differ by gauge trasformations are physically equivalent). Therefore, the Hilbert space defined previously is too large: it contains also non-physical states. We must restrict the Hilbert space to the space of gauge-invariant physical states by imposing the following constraint:

$$\hat{R}(\varphi(\mathbf{z}))\left|\Psi\right\rangle = \left|\Psi\right\rangle \tag{1.7.9}$$

whence

$$\nabla \cdot \hat{\mathbf{E}}(x^0, \mathbf{x})\left|\Psi\right\rangle = 0 \quad \forall x^0, \mathbf{x} \tag{1.7.10}$$

which is the quantum version of the classical Gauss' law for the free electromagnetic field. So finally, only the states which obey this law define the physical Hilbert space.

1.8 Quantum gauge theory: QED

Starting from the classical form of the comparator (1.5.8), we perform its quantization in the gauge $A^0 = 0$, obtainig the following operator:

$$\hat{U}(x^0, \mathbf{x}, \mathbf{y}) = \exp\left\{-i\int_{\mathbf{x}}^{\mathbf{y}} d\mathbf{z} \cdot \hat{\mathbf{A}}(x^0, \mathbf{z})\right\}. \tag{1.8.1}$$

It can be shown [26] that, in quantum formalism, it trasforms according to (1.5.2) under local gauge trasformation, namely

$$\hat{R}^{\dagger}(\varphi(\mathbf{z}))\hat{U}(x^0, \mathbf{x}, \mathbf{y})\hat{R}(\varphi(\mathbf{z})) = e^{i\varphi(\mathbf{x})}\hat{U}(x^0, \mathbf{x}, \mathbf{y})e^{-i\varphi(\mathbf{y})}. \tag{1.8.2}$$

We define a quantistic counterpart of the covariante derivative (1.5.3) as

$$\hat{D}_{\eta}\hat{\psi}(x) = \lim_{\epsilon \to 0}\frac{1}{\epsilon}\left[\hat{U}(x, x+\epsilon\eta)\hat{\psi}(x+\epsilon\eta) - \hat{\psi}(x)\right]. \tag{1.8.3}$$

Therefore, taking into account the definitions (1.6.8) and (1.7.5) and the classical interaction theory, we can define the Hamiltonian density operator of a system in which the Dirac and the electromagnetic fields interact with each other, i.e. quantum electrodynamics, as

$$\hat{H} = \hat{\bar{\psi}}(-i\gamma^i\hat{D}_i + m)\hat{\psi} + \frac{1}{2}(\hat{\mathbf{E}}^2 + \hat{\mathbf{B}}^2). \tag{1.8.4}$$

This operator is invariant under an appropriate gauge trasformation which operates simultaneously on the Dirac field and the electromagnetic field and represents the quantum counterpart of the classical local trasformations (1.4.6). This trasformation can be performed by the operators $\hat{T}$ and $\hat{R}$ as follows

$$(\hat{T} \otimes \hat{R})^{\dagger} \hat{H} (\hat{T} \otimes \hat{R}) = \hat{H}. \tag{1.8.5}$$

The Hilbert space of the system is the tensor product of the Dirac and electromagnetic Hilbert spaces, thus a generic state can be written as linear combination of vectors of the form$|\Phi\rangle = |\phi\rangle_{\mathcal{D}} \otimes |\psi\rangle_{el}$. Due to the gauge symmetry, in this case too, we must restrict the Hilbert space to the space of gauge-invariant physical state by imposing a new constraint:

$$(\hat{T} \otimes \hat{R}) \, |\phi\rangle_{\mathcal{D}} \otimes |\psi\rangle_{el} = 0 \tag{1.8.6}$$

whence

$$(\hat{\psi}^{\dagger} \hat{\psi} - \nabla \cdot \hat{\mathbf{E}}) \, |\Phi\rangle = 0 \tag{1.8.7}$$

which is the Gauss'law in presence of charges.

Chapter 2

Regularization on a lattice

We now analyze the formulation of the QED, that we have described in the previous chapter as a continuum gauge theory, on a discrete lattice. This formulation is an example of what is usually called *lattice gauge theory*. We will introduce the fermion doubling problem, which comes out in the transition from continuous to discrete space and we will implement the gauge fields and the gauge transformations on the lattice. At the end of this chapter, we will get to a lattice one dimensional formulation of QED.

2.1 Fermion doubling problem

In the continuum space, the euclidean action of the free Dirac field is [37]

$$S_E = \int d^4x_E\, \overline{\psi}(\gamma^E_\mu \partial_\mu + m)\psi \tag{2.1.1}$$

in which $\mu = 1, 2, 3, 4$ and $x_{E\mu} \equiv (x^i, ix^0)$, $\gamma^E_4 \equiv \gamma^0$, $\gamma^E_i \equiv -i\gamma^i$. The Feynman propagator results

$$G_F(x-y) = \int \frac{d^4p_E}{(2\pi)^4} \frac{[(-i)\sum_\mu \gamma^E_\mu p_{E\mu} + m]}{\sum_\mu p^2_{E\mu} + m^2} e^{ip_E(x_E - y_E)}. \tag{2.1.2}$$

in which $p_{E\mu} \equiv (p^i, ip^0)$. If we suppose to discretize the space-time with a four-dimensional lattice, the fermion field $\psi(x)$ must be replaced by a suitable variable ψ_x, which lives on the lattice point x, and the derivatives ∂_μ must be discretized by finite differences. In this way, the action can be written in the following form

$$S_E = a^4 \sum_{x,\mu} \left\{ \frac{1}{2a} (\overline{\psi}_x \gamma_\mu^E \psi_{x+\hat{\mu}} - \overline{\psi}_x \gamma_\mu^E \psi_{x-\hat{\mu}}) + m\overline{\psi}_x \psi_x \right\} \tag{2.1.3}$$

in which a is the lattice spacing and the integral over space-time is replaced by a lattice sum. In addition, to regain correctly the continuum limit in (2.1.3), the lattice variables have been defined in a dimensionless way, i.e.

$$\begin{aligned} \psi(x) &\rightarrow \frac{1}{a^{3/2}} \psi_x \\ \bar{\psi}(x) &\rightarrow \frac{1}{a^{3/2}} \bar{\psi}_x \\ m &\rightarrow \frac{1}{a} m. \end{aligned} \tag{2.1.4}$$

It can be shown [37] that the lattice fermion propagator becomes (we neglect the subscript of the euclidean four-vectors $\mathbf{x}_E$ and $\mathbf{p}_E$)

$$G_F^{latt}(x-y) = \int_{BZ} \frac{d^4\tilde{p}}{(2\pi)^4} \frac{[(-i)\sum_\mu \gamma_\mu^E \tilde{p_\mu} + m]}{\sum_\mu \tilde{p_\mu}^2 + m^2} e^{ip(x-y)} \tag{2.1.5}$$

where BZ is a four-dimensional Brillouin zone $\left[-\frac{\pi}{a}, \frac{\pi}{a}\right]^4$ with periodic boundary conditions and

$$\tilde{p_\mu} = \frac{1}{a} \sin(p_\mu a) \tag{2.1.6}$$

In the continuum limit $a \rightarrow 0$, the lattice propagator would reduce to the fermion propagator in the euclidean formulation, but in this case there is a problem due to the definition of $\tilde{p_\mu}$. In Fig. 2.1.1, the blue line corresponds to $\tilde{p_\mu}$ as a function of p_μ in the one-dimensional Brillouin zone, while the violet line represents the condition $\tilde{p_\mu} = p_\mu$ (expected continuum limit). In the half Brillouin zone $[-\frac{\pi}{2a}, \frac{\pi}{2a}]$, there is a deviation from the continuum limit only for large momenta where p_μ and $\tilde{p_\mu}$ are of order $\frac{1}{a}$. Therefore, when a is very small, this deviation becomes very negligible in the integral which defines the propagator $G_F(x-y)$. The problem arises from the presence of zeros of the sine-function at the edges of the Brillouin zone: whatever is the value of a, there are regions (in the one dimensional case $[\frac{\pi}{2a}, \frac{\pi}{a})$ and $(-\frac{\pi}{a}, -\frac{\pi}{2a}]$) where $\tilde{p_\mu}$ has significantly different values from p_μ: this values remain finite in the limit $a \rightarrow 0$ and give contributions in $G_F^{latt}(x-y)$ which are absent in

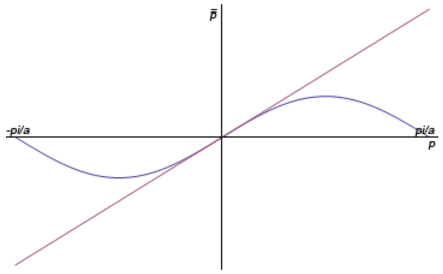

Figure 2.1.1: $\tilde{p}_\mu$ as a function of p_μ in the Brillouin zone (blue line) with the expected continuum limit (violet line).

$G_F(x-y)$. This can easily be seen in a one dimensional case in which we have only one component of the moment, for example p_1. We can compute the lattice propagator as follows:

$$\begin{aligned} G_F^{latt}(x-y) &= \int_{-\frac{\pi}{a}}^{\frac{\pi}{a}} \frac{d\tilde{p_1}}{2\pi} \frac{[(-i)\gamma_1^E \tilde{p_1} + m]}{\tilde{p_1}^2 + m^2} e^{i\tilde{p_1}(x_1-y_1)} \\ &= \int_{-\frac{\pi}{2a}}^{\frac{\pi}{2a}} \frac{d\tilde{p_1}}{2\pi} \frac{[(-i)\gamma_1^E \tilde{p_1} + m]}{\tilde{p_1}^2 + m^2} e^{i\tilde{p_1}(x_1-y_1)} \\ &+ \int_{\frac{\pi}{2a}}^{\frac{\pi}{a}} \frac{d\tilde{p_1}}{2\pi} \frac{[(-i)\gamma_1^E \tilde{p_1} + m]}{\tilde{p_1}^2 + m^2} e^{i\tilde{p_1}(x_1-y_1)} \\ &+ \int_{-\frac{\pi}{a}}^{-\frac{\pi}{2a}} \frac{d\tilde{p_1}}{2\pi} \frac{[(-i)\gamma_1^E \tilde{p_1} + m]}{\tilde{p_1}^2 + m^2} e^{i\tilde{p_1}(x_1-y_1)} \end{aligned} \tag{2.1.7}$$

In the first integral, being in the half Brillouin zone, we can replace $\tilde{p_1}$ with p_1 when a is very small. In the second and third integral we can approximate the relation (2.1.6) with an expansion in $\pm\frac{\pi}{a}$ respectively, so that $\tilde{p_1} \approx -p_1 \pm \frac{\pi}{a}$. We obtain

$$\begin{aligned} G_F^{latt}(x-y) &\approx \int_{-\frac{\pi}{2a}}^{\frac{\pi}{2a}} \frac{dp_1}{2\pi} \frac{[(-i)\gamma_1^E p_1 + m]}{p_1^2 + m^2} e^{ip_1(x_1-y_1)} \\ &+ \int_{-\frac{\pi}{a}}^{-\frac{\pi}{2a}} \frac{dp_1}{2\pi} \frac{[(-i)\gamma_1^E(-p_1 + \frac{\pi}{a}) + m]}{(-p_1 + \frac{\pi}{a})^2 + m^2} e^{i(-p_1+\frac{\pi}{a})(x_1-y_1)} \\ &+ \int_{\frac{\pi}{2a}}^{\frac{\pi}{a}} \frac{dp_1}{2\pi} \frac{[(-i)\gamma_1^E(-p_1 - \frac{\pi}{a}) + m]}{(-p_1 - \frac{\pi}{a})^2 + m^2} e^{i(-p_1-\frac{\pi}{a})(x_1-y_1)}. \end{aligned} \tag{2.1.8}$$

We perform now the following substitutions: $p = p_1 - \frac{\pi}{a}$ in the second integral, $p = p_1 + \frac{\pi}{a}$ in the third. Due to periodicity in the momentuum space, we can retrieve the integration limits in the Brillouin zone. Thus, we get

$$\begin{aligned} G_F^{latt}(x-y) \approx & \int_{-\frac{\pi}{2a}}^{\frac{\pi}{2a}} \frac{dp_1}{2\pi} \frac{[(-i)\gamma_1^E p_1 + m]}{p_1^2+m^2} e^{ip_1(x_1-y_1)} \\ & + \int_0^{\frac{\pi}{2a}} \frac{dp}{2\pi} \frac{[(-i)\gamma_1^E(-p) + m]}{p^2+m^2} e^{i(-p)(x_1-y_1)} \\ & + \int_{-\frac{\pi}{2a}}^{0} \frac{dp}{2\pi} \frac{[(-i)\gamma_1^E(-p) + m]}{p^2+m^2} e^{i(-p)(x_1-y_1)}. \end{aligned} \tag{2.1.9}$$

By replacing $p_1 = -p$ in the second and third integral, we obtain

$$\begin{aligned} G_F^{latt}(x-y) = & \int_{-\frac{\pi}{2a}}^{\frac{\pi}{2a}} \frac{dp_1}{2\pi} \frac{[(-i)\gamma_1^E p_1 + m]}{p_1^2+m^2} e^{ip_1(x_1-y_1)} \\ & + \int_{-\frac{\pi}{2a}}^{\frac{\pi}{2a}} \frac{dp_1}{2\pi} \frac{[(-i)\gamma_1^E p_1 + m]}{p_1^2+m^2} e^{ip_1(x_1-y_1)} \\ & \approx 2\, G_F(x-y) \quad \text{when } a \to 0 \end{aligned} \tag{2.1.10}$$

This result tells us that when we try to retrieve the limit $a \to 0$ in a one-dimensional lattice, an additional "fermion", which is a pure lattice artefact and has no continuum analog, emerges. This is the central point of the *fermion doubling problem*: when we try to put fermionic fields on a lattice, spurious states appear and the propagator receives contributions from all fermions, also the ones that do not really exist in the original continumm theory. In a d-dimensional lattice, there are $2^d - 1$ of this spurious excitations.

2.2 Relation to chiral anomaly

Let us go back for a moment to the classical electrodynamics. The Lagragian density (1.4.8), in addition to the gauge invariance, has another particular symmetry in the massless case. If we set $m = 0$ and perform the following trasformation

$$\psi' = e^{i\theta\gamma^5}\psi \tag{2.2.1}$$

where $\theta \in \mathbb{R}$ and $\gamma^5 = \gamma^0\gamma^1\gamma^2\gamma^3$, it results that $\mathcal{L}$ is invariant. This property is called *chiral symmetry.* In agreement with Noether's theorem, there is a conserved current, which has density

$$j^{u5} = \bar{\psi}\gamma^{\mu}\gamma^{5}\psi \tag{2.2.2}$$

such that the conservation law results

$$\partial_{\mu}j^{\mu 5} = 0. \tag{2.2.3}$$

Once performed the quantization, it can be shown, using a method known as *Fujikawa method* [11], that in the QED-framework the chiral current is not conserved. This effect, which implies quantum nonconservation of a conserved current in the classical scheme, is called *chiral anomaly.*

In the lattice formulation of a chiral theory based on a discretization of the Lagrangian, the chiral symmetry implies that the associated current is strickly conserved for any lattice spacing, therefore the anomaly is totally absent. Thus, lattice regularization generates extra fermions needed to cancel this anomaly of the continuum theory. This is the fundamental reason of the fermion doubling.

2.3 Nielsen and Ninomiya theorem

If we want to prevent the fermion doubling when we perfom the regularization on lattice, we must first consider a theorem by Nielsen and Ninomiya [25].

This theorem states that a local, hermitian, lattice fermion action, which has translational invariance and chiral symmetry (even if only in the massless case), necessarily has fermion doubling.

As a result, the only way to get rid of the doublers is by violating one of the presuppositions of the theorem. There are several solutions for this purpose.

A first method is known as *Wilson fermions* [30]: in this scheme, a term which explicity breaks the chiral symmetry and vanishes in the continuum limit, is added to the lattice action (2.1.3). This term de facto associates an "infinite" mass to extra-fermions at the edges of the Brillouin zone. The result is that the continuum limit is now dominated by the fermion only in the origin and doubling is prevented. Obviously, with this method, the theory completely loses the original chirally invariance for $m = 0$.

An alternative method is known in the literature as *Staggered Fermions* [34] [3]: in order to understand the basic idea of this formulation, we recall that the fermion doubling problem arises from the fact that the lattice propagator (2.1.5) is dominated not only by values of p_μ near the origin (physical fermion), but also at the edges of the Brillouin zone (no-physical excitations). If somehow we could reduce the Brillouin zone to half of its initial size, the problem would disappear. This can be done by placing different fermions on adjacent lattice site, so the periodicity becomes $2a$ and the Brillouin zone in a d-dimensional case is effectively reduced to $[-\frac{\pi}{2a}, \frac{\pi}{2a}]^d$. This is the central point of staggered fermions method. In this case, the presupposition of the Nielsen and Ninomiya theorem which is violated is the locality, while the chiral symmetry is preserved.

We will use staggered fermions in the following, so we will explain this method in detail in the next section.

2.4 Staggered fermions

Now we restart from the classical Dirac Hamiltonian:

$$H = \int d^3x \, \bar{\psi}(-i\gamma^i\partial_i + m)\psi \tag{2.4.1}$$

in which we have used the chiral representation (1.2.7). We want to change representation for the Dirac spinors and for γ^μ matrices, by switching from chiral to standard representation. In this scheme the four-components Dirac spinor can be written as

$$\psi = \begin{bmatrix} \psi_+ \\ \psi_- \end{bmatrix} = \begin{bmatrix} \psi_{+,1} \\ \psi_{+,2} \\ \psi_{-,1} \\ \psi_{-,2} \end{bmatrix} \tag{2.4.2}$$

i.e. ψ is composed now by a positive energy two-component spinor (particle) and by a negative two-component energy spinor (antiparticle), and the γ^μ matrices become

$$\gamma^0 = \begin{bmatrix} \mathbf{1} & \mathbf{0} \\ \mathbf{0} & -\mathbf{1} \end{bmatrix} \quad \gamma^i = \begin{bmatrix} \mathbf{0} & \sigma_i \\ -\sigma_i & \mathbf{0} \end{bmatrix}. \tag{2.4.3}$$

Suppose we consider a spinless model in a (1+1) dimensional space: in this framework the Dirac spinor has only two components

$$\psi(x) = \begin{bmatrix} \chi_1(x) \\ \chi_2(x) \end{bmatrix} \tag{2.4.4}$$

and the 2×2 γ-matrices result

$$\gamma^0 = \begin{bmatrix} 1 & 0 \\ 0 & -1 \end{bmatrix} \quad \gamma^1 = \begin{bmatrix} 0 & 1 \\ -1 & 0 \end{bmatrix}. \tag{2.4.5}$$

Therefore, the Dirac equation (1.2.9) reduces to

$$(i\gamma^0\partial_0 + i\gamma^1\partial_1 + -m) \begin{bmatrix} \chi_1(x) \\ \chi_2(x) \end{bmatrix} = 0 \tag{2.4.6}$$

whence

$$\left\{ \begin{array}{l} i\partial_t\chi_1(x) = +m\chi_1(x) - i\partial_x\chi_2(x) \\ i\partial_t\chi_2(x) = -m\chi_2(x) - i\partial_x\chi_1(x) \end{array} \right. . \tag{2.4.7}$$

We implement this model on a one-dimensional lattice with spacing a, assuming that time remains continuous and discretizing the x-derivative by the finite difference of the two neighbouring points. We obtain:

$$\left\{ \begin{array}{l} i\partial_t\chi_{1,x} = +m\chi_{1,x} - \frac{i}{2a}(\chi_{2,x+1} - \chi_{2,x-1}) \\ i\partial_t\chi_{2,x} = -m\chi_{2,x} - \frac{i}{2a}(\chi_{1,x+1} - \chi_{1,x-1}) \end{array} \right. . \tag{2.4.8}$$

Remembering that our purpose is to prevent the fermion doubling problem, this discretization looks very interesting. In fact we can see in (2.4.8) that the first spinor component χ_1 is connected to the second component χ_2 only on sites with different parity and viceversa. Thus, altought we have two components on each site, de facto this lattice variables form two independent sets: if x has even parity for example, $\chi_{1,x}$ depends only on $\chi_{2,x\pm1}$ and $\chi_{2,x\pm1}$only on $\chi_{1,x\pm2}$ and so on. Viceversa for $\chi_{2,x}$. Therefore, we can consider only one of these two connected groups by defining a single component lattice fermion field ζ_x that must be correctly reduced to χ_1 or χ_2 depending on parity of the site [24]:

$$\zeta_x = \left\{ \begin{array}{ll} \chi_{1,x} & x - odd \\ \chi_{2,x} & x - even \end{array} \right. \tag{2.4.9}$$

The two spinor components of the fermions sit on different sites now: on even sites there are positive energy solutions, on odd sites negative energy solutions. As a result, the number of degrees of freedom is divided by two and the fermion doubling problem is pratically eliminated. In other words, we can imagine to divide the initial one dimensional lattice with spacing a into blocks of two sites with alternating spinor components. The periodicity of the system becomes $2a$ and so we avoid the extra excitation at the edges of the Brillouin zone. The price that one pays in the use of staggered fermions is the locality of the Hamiltonian density, or equivalently of the corresponding action, because the initital spinor fields $\psi(x)$ are now delocalised over two sites.

We stress that in the model exhibited in this section the time is considered continuous, so the fermion doubling problem could arise only by discretizing the spatial x-axis. Hence the presence of only one and not three extra excitations.

2.5 Staggered fermion Hamiltonian

The use of staggered fermions in a one dimensional lattice model allows us to write the classical free Dirac Hamiltonian (2.4.1) in the following form [34]:

$$H = \left(-\frac{i}{2a}\right) \sum_x \zeta_x^\dagger \zeta_{x+1} + \text{h.c.} + m \sum_x (-1)^x \zeta_x^\dagger \zeta_x \tag{2.5.1}$$

We note immediately that the staggered structure corresponds to having particles with a positive mass term on even sites, antiparticles with a negative mass term on odd sites. Furthermore, the global $U(1)$ symmetry of the continuum Dirac theory is preserved in this lattice formulation: infact if we perform the analogous of the trasformation (1.4.1) as follows

$$\zeta_x^{'} = \zeta_x e^{i\alpha} \tag{2.5.2}$$

the Hamiltonian results invariant.

In the continuum space, there was another particulary symmetry that we have presented in section 2.2: the chiral symmetry for $m = 0$. In a one-dimensional lattice model, it results that

$$\gamma^5 = \gamma^0 \gamma^1 = \begin{bmatrix} 0 & 1 \\ 1 & 0 \end{bmatrix} \tag{2.5.3}$$

from which

$$\gamma^5 \psi_x = \begin{bmatrix} 0 & 1 \\ 1 & 0 \end{bmatrix} \begin{bmatrix} \chi_{1,x} \\ \chi_{2,x} \end{bmatrix} = \begin{bmatrix} \chi_{2,x} \\ \chi_{1,x} \end{bmatrix} \tag{2.5.4}$$

i.e. the chiral trasformation is equivalent to the interchange of the two spinor components. In the staggered structure that we have introduced in (2.4.9) this interchange can be done by performing a lattice shift with an odd integer k:

$$\begin{aligned}\zeta_x &\to \zeta_{x+k}\\ \zeta_x^\dagger &\to \zeta_{x+k}^\dagger\end{aligned} \tag{2.5.5}$$

Now, in the staggered Hamiltonian (2.5.1), the kinetic term has odd-shift invariance, while the mass term doesn't. Therefore, also the chiral symmetry for $m = 0$ is preserved.

In addition, it can be easily seen that the kinetic and mass term both have even-shift invariance (trasformations (2.5.5) with k even): this is the lattice analogous of translational symmetry of the continuum Hamiltonian.

Now it is easy to perform the quantization by following the guidelines of section 1.6. First we can promote the lattice variables to fields operator $\hat{\zeta}_x$ and $\hat{\zeta}_x^\dagger$, then we can implement on lattice the fermionic anticommutation relations as follows:

$$\left\{\hat{\zeta}_x, \hat{\zeta}_y^\dagger\right\} = \delta_{x,y} \quad \left\{\hat{\zeta}_x, \hat{\zeta}_y^\dagger\right\} = 0 \quad \left\{\hat{\zeta}_x^\dagger, \hat{\zeta}_y^\dagger\right\} = 0 \ . \tag{2.5.6}$$

The discrete version of the operator (1.6.15), which performs the $U(1)$ trasformation of quantum fermionic fields, results

$$\hat{T}(\alpha_x) = \prod_y e^{i\alpha_y\left\{\hat{\zeta}_y^\dagger\hat{\zeta}_y + \frac{1}{2}[(-1)^y - 1]\right\}} \tag{2.5.7}$$

in which the presence of the additional term $\frac{1}{2}[(-1)^y - 1]$ is solely due to the use of staggered fermions. In this way, it can be easily verified that

$$\hat{T}^\dagger\hat{\zeta}_x\hat{T} = e^{i\alpha_x}\hat{\zeta}_x. \tag{2.5.8}$$

Due to the $U(1)$ global symmetry, which is preserved in our lattice formulation, when α is a constant, it results

$$[\hat{T}, \hat{H}] = 0. \tag{2.5.9}$$

The ground state of the free staggered Hamiltonian (2.5.1) consists in a filled Dirac sea of negative energy states, which corresponds to the complete occupation of the odd sites.

2.6 Lattice gauge theory

Our goal now is to reach a one dimensional lattice formulation of QED, namely a discrete version of the Hamiltonian density (1.8.4) that reflects its properties and, in particular, the local gauge symmetry (1.8.5).
We can start right from the continuum Hamiltonian

$$\hat{H} = \int d^3x \, \hat{\bar{\psi}}(-i\gamma^i \hat{D}_i + m)\hat{\psi} + \frac{1}{2}(\hat{\mathbf{E}}^2 + \hat{\mathbf{B}}^2). \tag{2.6.1}$$

When we get in a one dimensional space, there cannot be magnetic field. Also, we have the two component spinor (2.4.4) and the 2 × 2 γ-matrices (2.4.5). So, it results

$$\hat{H} = \int dx \, \hat{\bar{\psi}}(-i\gamma^1 \hat{D}_1 + m)\hat{\psi} + \frac{1}{2}\hat{\mathbf{E}}^2 \tag{2.6.2}$$

If we use the definition of covariant derivative (1.8.3), the kinetic term results:

$$\hat{H}_{kin} = \lim_{\epsilon \to 0} \int dx \left(-\frac{i}{\epsilon}\right) \left\{ \hat{\psi}^\dagger(x)\gamma^0\gamma^1 \hat{U}(x, x+\epsilon)\hat{\psi}(x+\epsilon) - \hat{\psi}^\dagger(x)\gamma^0\gamma^1\hat{\psi}(x) \right\} \tag{2.6.3}$$

Now consider the first term in this expression:

$$\begin{aligned} &\hat{\psi}^\dagger(x)\gamma^0\gamma^1\hat{U}(x, x+\epsilon)\hat{\psi}(x+\epsilon) = \\ &= \begin{bmatrix} \hat{\chi}_1^\dagger(x) & \hat{\chi}_2^\dagger(x) \end{bmatrix} \begin{bmatrix} 0 & 1 \\ 1 & 0 \end{bmatrix} \begin{bmatrix} \hat{\chi}_1(x+\epsilon) \\ \hat{\chi}_2(x+\epsilon) \end{bmatrix} \hat{U}(x, x+\epsilon) \\ &= \hat{\chi}_1^\dagger(x)\hat{U}(x, x+\epsilon)\hat{\chi}_2(x+\epsilon) + \hat{\chi}_2^\dagger(x)\hat{U}(x, x+\epsilon)\hat{\chi}_1(x+\epsilon). \end{aligned} \tag{2.6.4}$$

When we consider the lattice discretization, it becomes:

$$\hat{\chi}_{1,x}^\dagger \hat{U}(x, x+a)\hat{\chi}_{2,x+a} + \hat{\chi}_{2,x}^\dagger \hat{U}(x, x+a)\hat{\chi}_{1,x+a} \tag{2.6.5}$$

Due to the use of the staggered fermions, we know that we have to consider only one of the two decoupled sets of spinor components. Therefore, we can remove the second term in this expression. For the same reason also the second term in (2.6.3) can be removed. Setting $a = 1$, it results

$$\hat{H}_{kin} = (-i)\sum_x \hat{\zeta}_x^\dagger \hat{U}(x, x+1)\hat{\zeta}_{x+1} + \text{h.c.} \tag{2.6.6}$$

In the same way, the mass term in (2.6.2) becomes

$$\hat{H}_m = m \sum_x (-1)^x \hat{\zeta}_x^\dagger \hat{\zeta}_x \tag{2.6.7}$$

that is clearly the same expression of the staggered Hamiltonian (2.5.1). Now what is left is to understand how the electric field term can be implemented on a lattice. An indication for this purpose comes from the structure of the kinetic term, which contains the comparator $\hat{U}(x, x+1)$. We recall for a moment its general definition (1.8.1):

$$\hat{U}(x, y) = \exp\left\{-i \int_x^y d\mathbf{z} \cdot \hat{\mathbf{A}}(\mathbf{z})\right\} \tag{2.6.8}$$

In a one dimensional space the vector potential has only one component, so it results:

$$\hat{U}(x, x+1) = \exp\left\{-i \int_x^{x+1} dz \, \hat{A}(z)\right\}. \tag{2.6.9}$$

Analyzing this expression and, in particular, the line integral in it, we can see that a natural way to implement the gauge field on lattice is to define the vector potential $\hat{A}$ and, consequently, the electric field $\hat{E}$, on the links between the lattice sites. To do this, we can introduce a link operators $\hat{A}_{x,x+1}$ and $\hat{E}_{x,x+1}$ such that there is the following correspondences in the transition from continuous to discrete space:

$$\int_x^{x+1} dz \, \hat{A}(z) \quad \rightarrow \quad \hat{A}_{x,x+1} \tag{2.6.10}$$

$$\left[\hat{A}(\mathbf{x}), \hat{E}(\mathbf{y})\right] = -i\delta^{(3)}_{\mathbf{x},\mathbf{y}} \quad \rightarrow \quad \left[\hat{A}_{x,x+1}, \hat{E}_{x',x'+1}\right] = -i\delta_{x,x'} \tag{2.6.11}$$

In this way, it is easy to obtain a correct implementation of the comparator on the links, by defining

$$\hat{U}_{x,x+1} \equiv e^{-i\hat{A}_{x,x+1}}. \tag{2.6.12}$$

In order to verifiy that this is a correct choice, we recall that the kinetic term (2.6.6) must be gauge invariant. This occurs only if $\hat{U}_{x,x+1}$ trasforms in an appropriate way, which corresponds to the trasformation law (1.8.2) adapted on the lattice. Therefore, we can introduce the discrete version of the operator (1.7.7), which performs the gauge trasformation of the quantum vector potential in the following way

$$\hat{R}(\alpha_x) = \prod_y e^{-i\alpha_y(\hat{E}_{y,y+1} - \hat{E}_{y,y-1})} \tag{2.6.13}$$

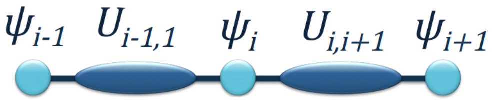

Figure 2.6.1: Implementation of the fermionic field and the gauge field on a one-dimensional lattice.

in which we have discretized the electric field divergence. If we compute the trasformation law of $\hat{U}_{x,x+1}$ using the commutation relation (2.6.11), we get

$$\hat{R}^{\dagger}\hat{U}_{x,x+1}\hat{R} = e^{i\alpha_x}\hat{U}_{x,x+1}e^{-i\alpha_{x+1}} \tag{2.6.14}$$

which is exactly the discrete analogous of the trasformation law (1.8.2), as desidered. This is enough to ensure the local invariance of the kinetic term under the complete lattice gauge trasformation which operates simultaneously on the Dirac and the electromagnetic field, i.e.:

$$(\hat{T} \otimes \hat{R})^{\dagger}\hat{H}_{kin}(\hat{T} \otimes \hat{R}) = \hat{H}_{kin}. \tag{2.6.15}$$

As a result, we can finally write a lattice version of the one dimensional QED Hamiltonian (2.6.2) (we rename the staggered fermionic field with $\hat{\psi}_x$):

$$\hat{H} = -t\sum_x \hat{\psi}_x^{\dagger}\hat{U}_{x,x+1}\hat{\psi}_{x+1} + \text{h.c.} + m\sum_x (-1)^x\hat{\psi}_x^{\dagger}\hat{\psi}_x + \frac{g^2}{2}\sum_x \hat{E}_{x,x+1}^2 \tag{2.6.16}$$

in which we have introduced a general hopping constant t and a coupling constant g. This Hamiltonian is clearly gauge invariant and describes, in a very general way, a quantized Abelian lattice gauge theory, in which the gauge field is coupled with a spinless Dirac field.

Let us summarize the main findings of this section. We have implemented the fermionic field on the sites of a one dimensional lattice by using staggered fermions, which provide an elegant way of simultaneously incorporating matter and antimatter fields. Then, we have defined the gauge field, represented by the comparator, on the links between the lattice sites, as shown in Fig 2.6.1. The two fields are coupled due to the kinetic term in (2.6.16): a fermion tunneling from site i to $i+1$ corresponds, in general, to a change of the electric field on the link in between. Futhermore, the local symmetry

(2.6.15) makes the coupling more "physical": if we write the operator $\hat{T} \otimes \hat{R}$ in a more compact way as

$$\hat{T} \otimes \hat{R} = \prod_x e^{i\alpha_x \hat{G}_x} \tag{2.6.17}$$

in which the generators are

$$\hat{G}_x = \hat{\psi}_x^\dagger \hat{\psi}_x - (\hat{E}_{x,x+1} - \hat{E}_{x,x-1}) + \frac{1}{2}[(-1)^x - 1] \tag{2.6.18}$$

we can easily understand that, as in the continuum case of section 1.8, we have to perform a restriction to a gauge invariant subspace, which is defined by the condition

$$\hat{G}_x \left|\Psi\right\rangle = 0 \quad \forall x. \tag{2.6.19}$$

This relation represents nothing else but equation (1.8.7). Therefore, the local gauge symmetry allows us to select correctly only physical states which respect the Gauss law.

Chapter 3

Quantum simulation models

In this chapter we want to introduce a generic class of models that capture gauge invariance of our lattice gauge theory and at the same time are suitable for quantum simulations. This latter purpose involves a general reduction of the degrees of freedom of the system, so that it is possible to work with a finite number of states and values. However, this models share an important feature: in a suitable thermodynamic limit they should recover the corresponding continuous gauge theory that, in our case, is the QED.

3.1 Quantum Link Model

In the one dimensional lattice QED Hamiltonian that we have presented in the section 2.6, the fermionic operators live in a finite space, while the link operators $\hat{U}_{x,x+1}$ are defined in an infinite dimensional Hilbert space: indeed the electric field, in principle, can assume arbitrary values on each link. Futhermore, this operators involve a particular set of commutation relations, which are summarized as

$$[\hat{E}_{x,x+1}, \hat{U}_{x',x'+1}] \;=\; \delta_{x,x'}\hat{U}_{x,x+1}. \tag{3.1.1}$$

The main point of the Quantum Link Model (QLM) [38] is the introduction of link operators which span a finite dimensional Hilbert space and, at the same time, retain the commutation relations (3.1.1). The solution performed in the QLM consists in a substitution of the quantum link operator as well as the electric field operator with a quantum spin operator associated with a given link. In more technical terms, we consider the spin operators $\hat{S}^i$ with

$i = 1, 2, 3$ and the ladder corresponding operators $\hat{S}^{\pm} = \hat{S}^1 \pm i\hat{S}^2$, which satisfy the following commutation relations

$$[\hat{S}^3, \hat{S}^{\pm}] = \pm \hat{S}^{\pm}. \tag{3.1.2}$$

Therefore, a smart link correspondence is established:

$$\begin{aligned} \hat{U}_{x,x+1} &\rightarrow \hat{S}^{+}_{x,x+1} && (3.1.3) \\ \hat{U}^{\dagger}_{x,x+1} &\rightarrow \hat{S}^{-}_{x,x+1} && (3.1.4) \\ \hat{E}_{x,x+1} &\rightarrow \hat{S}^{3}_{x,x+1}. && (3.1.5) \end{aligned}$$

In this way, due to the (3.1.2), the initial commutation relation (3.1.1) is automatically satisfied.

The advantage of this formulation is that now, if S is the modulus of the spin, the electric field on a link can take only discrete values $\{-S, -S+1, \ldots, S\}$. So, the link Hilbert space is (2S+1)-dimensional.

We can now write the Hamiltonian (2.6.16) in a QLM-version:

$$\hat{H} = -t \sum_{x} \hat{\psi}^{\dagger}_{x} \hat{S}^{+}_{x,x+1} \hat{\psi}_{x+1} + \text{h.c.} + m \sum_{x} (-1)^{x} \hat{\psi}^{\dagger}_{x} \hat{\psi}_{x} + \frac{g^2}{2} \sum_{x} {\hat{S}^{3}}^{2}_{x,x+1}. \tag{3.1.6}$$

The Hilbert space on which this Hamiltonian acts is the tensor product of the Hilbert spaces relative to each site and each link, which have respectively the following form:

$$\begin{aligned} \mathcal{H}_x &= \{ |0\rangle, |1\rangle \} && (3.1.7) \\ \mathcal{H}_{x,x+1} &= \{ |k_{x,x+1}\rangle, \; k_{x,x+1} = -S, -S+1, \ldots, S \}. && (3.1.8) \end{aligned}$$

In this scheme, we can have a clear interpretation of the kinetic term in (3.1.6): when a fermion passes from site $x+1$ to x, the electric field on the link in between is increased from $|k_{x,x+1}\rangle$ to $|k_{x,x+1}+1\rangle$. Conversely, when a fermion passes from site x to $x+1$, it is decremented from $|k_{x,x+1}\rangle$ to $|k_{x,x+1}-1\rangle$. Clearly, the $U(1)$ local gauge invariance of the Hamiltonian is preserved in the QLM: in fact, if we write the generators (2.6.18) as follows

$$\hat{G}_x = \hat{\psi}^{\dagger}_{x} \hat{\psi}_{x} - (\hat{S}^{3}_{x,x+1} - \hat{S}^{3}_{x,x-1}) + \frac{1}{2}[(-1)^x - 1] \tag{3.1.9}$$

it results, once again, that

$$[\hat{G}_x, \hat{H}] = 0 \quad \forall x. \tag{3.1.10}$$

So, we have to select for the system only the physical gauge invariant states. This states, which satisfy the Gauss law, have now a specific property: the condition (2.6.19) becomes a local equation for the eigenvalues of the operators $\hat{G}_x$:

$$n_x - (k_{x,x+1} - k_{x,x-1}) + \frac{1}{2}[(-1)^x - 1] = 0 \quad \forall x \tag{3.1.11}$$

in which n_x is the fermion site occupation number.
We emphasize one point of the QLM formulation: the substitutions (3.1.3), (3.1.4) and (3.1.5) preserve the algebra relation (3.1.1), but the structure of the gauge coupling is altered: the new comparator is no longer unitary since

$$(\hat{S}^{+}_{x,x+1})^{\dagger}\hat{S}^{+}_{x,x+1} = \hat{S}^{-}_{x,x+1}\hat{S}^{+}_{x,x+1} \neq 1. \tag{3.1.12}$$

3.1.1 Quantum simulators

The QLM formulation represents the starting point for a great variety of quantum simulations: thanks to its discrete nature, quantum link models can be embodied by the quantum states of ultracold atoms in an optical lattice. A fermionic species will be used to define the matter field, while bosonic atoms are generally used to implement the electric field and the comparator. For example, in [2], using a Fermi-Bose mixture of ultracold atoms (one fermionic and two bosonic species) in an 3-strand optical lattice, a quantum simulator for our QED theory is proposed. In this realization, each fermion is allowed to tunnel along the whole lattice, while each boson is confined on a fixed couple of sites, which can be identified with a link. There are $2S$ bosonic atoms on each link which allow to have the same eigenvalues of the QLM electric field. A fermion hopping from x to $x+1$ is necessarily accompanied by a boson hopping the other way, i.e. a change in the electric field on the link in between, in order to conserve energy. Thus, the energy conservation ensures the gauge invariance. This process is well illustrated in Fig. 3.1.1a. This quantum simulator can be used to study the dynamics of *string breaking*, a non perturbative phenomenon that quantum electrodynamics (QED) in one spatial dimension shares the with quantum chromodynamics (QCD) [15]. Infact, differently from (3+1)d QED, in (1+1)d electrons and positrons interact via a long-range potential which increases linearly with distance [39]. So, when they (one electron and one positron) separate themselves, at some point it is more energetically favorable for a new electron–positron pair to

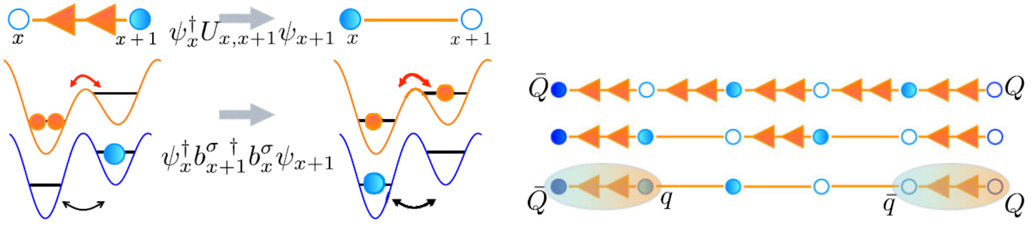

(a) (b)

Figure 3.1.1: (a) Scheme of the quantum simulator with a Fermi-Bose mixture of ultracold atoms. (b) String breaking phenomenon.

spontaneously appear, than to allow the "tube" of electric field to extend further: this is the string breaking phenomenon. As a result of this, instead of seeing the indivual fermion, we can see, in a detector for example, only particle-antiparticle states, called *mesons*. That is why we also speak of *confinement*, namely the impossibility of isolating, in this case, electrons and positrons. This mechanism is common to quarks, described by QCD, which always exhibit confinement.

In the context of the quantum simulator that we are describing, the string breaking effect has been observed dynamically, setting $S = 1$, in the following way: an external static quark-antiquark pair $Q\bar{Q}$ with a large separation is connected by a confining electric flux string and a vacuum fermionic state (due to the use of staggered fermions the vacuum consists in a filled Dirac sea of negative energy states, namely the complete occupation of the odd sites). In the dynamical evolution of this state, for sufficiently small fermion mass, the potential energy is converted into kinetic energy by fermion hopping, which amounts to the creation of a dynamical quark-antiquark pair $q\bar{q}$. At the end of the process, two mesons $\bar{Q}q$ and $\bar{q}Q$ result, separated by vacuum. The phenomenon is shown in Fig. 3.1.1b.

Another important feature, that this simulator suggests, is the presence in a possibile phase-diagram of a crossover between a "string" state characterized by a nonzero mean electric field and the vacumm Dirac sea with zero electric field.

Other quantum simulators of (1+1)QED, based on the QLM, have been built with a wide variety of techniques, such as ion trap in [14] or superconducting circuits in [22]. Setting, for example, $S = \frac{1}{2}$, i.e. two possible eletric field configurations on links, they allow the observation in realistic setups of spontaneous parity- and charge-symmetry breaking as well as the real-time dynamics, which are inaccessible to classical simulation methods. An attractive property of this simulators comes from a study of feasibility [19], which explores the effect of representing the gauge degrees of freedom with finite-dimensional systems and shows that the results converge rapidly to finite-size extrapolations of the lattice Schwinger model; thus even with small S it is possible to obtain a reasonable accuracy.

However, in a more general view, the quantum simulators find numerous applications in diverse areas of physics and chemistry. The general idea is the same: to use some controllable quantum system in order to study another less controllable or accessible quantum system or model. For example, a simulator of the Bose-Hubbard model with atoms in optical lattice has been proposed in [18] and implemented with rubidium atoms in [13]. This simulator has allowed the first observation of the quantum phase transition from a superfluid to a Mott insulator; similarly, in the context of superconductivity, by using a quantum simulator, it has been possible to observe a crossover between a BCS and a BEC superfluid as the strenght of attractive interactions between fermionic particles is varied. Also from a chemical point of view, quantum simulators play an important role: for example, it is possible to simulate the static and dynamical chemical properties of molecules (for example molecular energies as shown in [1]) or chemical reactions, as shown in [7].

These are just a few examples that allow us to understand how the quantum simulation is revolutionizing the physics research and because it represents, in the context of lattice gauge theories, one of the reasons of this thesis work.

3.2 Discrete Z_n Quantum Model

We have seen in the section 3.1 that in the QLM formulation, going from infinite to finite Hilbert spaces of the link operators, the comparator retains its algebra, that is the commutation relation (3.1.1), but loses its unitary nature, as shown in (3.1.12). Therefore, the formal structure of the hopping term is completely altered.

A different approach has recently been proposed in [27]. In this formulation, the structure of the original Hamiltonian (2.6.16), including the coupling of the matter fields with a unitary gauge operator, is completely preserved. As a result, the model exhibits a discrete gauge symmetry Z_n, approximating the $U(1)$ original symmetry for large n. We will use this model in our study, so we want to explain it in detail, by following the same logical steps as the original mentioned article.

3.2.1 Continuous Weyl group

We start with very general definitions. Consider two hermitian operators $\hat{E}$ and $\hat{A}$, defined in a continuous Hilbert space $\mathcal{H}$, such that they satisfy the Heisenberg commutation rule

$$[\hat{E}, \hat{A}] = i \tag{3.2.1}$$

and have the following eigenvalue equations

$$\begin{aligned} \hat{E}\,|\epsilon\rangle &= \epsilon\,|\epsilon\rangle && (3.2.2) \\ \hat{A}\,|\alpha\rangle &= \alpha\,|\alpha\rangle\,. && (3.2.3) \end{aligned}$$

The set of this operators and their polynomial function, equipped with the composition law (3.2.1), forms the Heisenberg's algebra. Starting from these definitions, we can introduce the following unitary operators, called Weyl operators:

$$\begin{aligned} \hat{U}(\eta) &= e^{-i\eta\hat{E}} && (3.2.4) \\ \hat{V}(\xi) &= e^{-i\xi\hat{A}} && (3.2.5) \\ \hat{W}(\eta,\xi) &= e^{-i(\eta\hat{E}+\xi\hat{A})} && (3.2.6) \end{aligned}$$

in which $\eta, \xi \in \mathbb{R}$. If we use the Baker-Hausdor formula[1], it results that

$$\hat{W}(\eta,\xi) = \hat{U}(\eta)\hat{V}(\xi)e^{\frac{1}{2}\eta\xi} \tag{3.2.7}$$

and also, changing the order of the addends in the exponent of $\hat{W}$,

$$\hat{W}(\eta,\xi) = \hat{V}(\xi)\hat{U}(\eta)e^{-\frac{1}{2}\eta\xi}. \tag{3.2.8}$$

As a result, taking into account the unitary character of $\hat{U}$ and $\hat{V}$, we can write

$$\hat{U}(\eta)\hat{V}(\xi) = e^{i\eta\xi}\hat{V}(\xi)\hat{U}(\eta). \tag{3.2.9}$$

---

[1] $e^{D+F} = e^{D}e^{F}e^{-\frac{1}{2}[D,F]}$ when $[D,[D,F]] = [F,[D,F]] = 0$

We can interprete to all effects this relation as the commutator between the Weyl operators. At this point, we can define the abstract continuous Weyl group: it is a two real parameters group whose generators obey the Heisenberg's algebra relation (3.2.1) and whose commutator have the form (3.2.9). The Weyl group elements are (3.2.4), (3.2.5), (3.2.6) and their compositions. We can now show how Weyl operators act on eigenstates of $\hat{E}$ or $\hat{A}$. If we use the usual representation for this operator in the position basis, i.e. $\hat{E} \to \epsilon$ and $\hat{A} \to -i\partial_\epsilon$, due to the presence of the traslation operator in the exponents, it results that

$$\hat{U}(\eta)\,|\epsilon\rangle \;=\; e^{-i\eta\hat{A}}\,|\epsilon\rangle = |\epsilon + \eta\rangle \tag{3.2.10}$$

while, if we use the representation in the momentum basis, i.e. $\hat{A} \to \alpha$ and $\hat{E} \to i\partial_\alpha$, for the same reason we have

$$\hat{V}(\xi)\,|\alpha\rangle = e^{-i\xi\hat{E}}\,|\alpha\rangle = |\alpha - \xi\rangle\,. \tag{3.2.11}$$

Thus, the Weyl operators act on this eigenstates as spectral translations in opposite directions. We stress also a general property: starting from (3.2.9), we can take the derivative as follows

$$\frac{\partial}{\partial\xi}|_{(\xi,\eta=0,1)}\left\{\hat{U}(\eta)\hat{V}(\xi)\right\} \;=\; \frac{\partial}{\partial\xi}|_{(\xi,\eta)=0,1}\left\{e^{i\eta\xi}\hat{V}(\xi)\hat{U}(\eta)\right\} \tag{3.2.12}$$

from which

$$\left[\hat{E},\hat{U}\right] = \hat{U} \tag{3.2.13}$$

in which $U = \hat{U}(1) = e^{-iA}$. Therefore, the Weyl relation (3.2.9) implies (3.2.13). If we interpret $\hat{E}$ as an electric field, $\hat{A}$ as a potential vector and $\hat{U}$ as a comparator, we immediately notice that the commutation relation (3.2.13) is exactly what we have found in the (1+1)d lattice QED with an infinite dimensional Hilbert space for each link. Therefore, in the continuous case, we have found a generalization of this commutation relation at the level of the Weyl group.

3.2.2 Discrete Schwinger-Weyl group

Let us consider a n-dimensional Hilbert space $\mathcal{H}$ with an orthonormal basis $\mathcal{B} = \{|a_l\rangle\}_{1\leq l\leq n}$. We can define a unitary operator $\hat{U}$ which rotates cyclically the basis states as [31]

$$\begin{aligned} \hat{U}\,|a_l\rangle &= |a_{l+1}\rangle && (3.2.14)\\ \hat{U}\,|a_n\rangle &= |a_1\rangle && (3.2.15)\\ \hat{U}^n &= \mathbf{1}. && (3.2.16) \end{aligned}$$

Note that the condition (3.2.15) distinguishes $\hat{U}$ from a ladder (increasing) operator, for which one would have $\hat{U}^+\,|a_n\rangle = 0$.
We consider now the eigenvalue equation of $\hat{U}$:

$$\hat{U}\,|u_k\rangle = u_k\,|u_k\rangle\,. \tag{3.2.17}$$

From (3.2.16), it follows that

$$\hat{U}^n\,|u_k\rangle = u_k^n\,|u_k\rangle = |u_k\rangle \tag{3.2.18}$$

therefore, the eigenvalues are the n roots of unity:

$$u_k = e^{-i\frac{2\pi}{n}k} \quad k = 1, 2, \dots n. \tag{3.2.19}$$

As a result, the eigenvalue equation (3.2.17) is satisfed for

$$|u_k\rangle = \frac{1}{\sqrt{n}}\sum_{l=1}^{n} e^{i\frac{2\pi}{n}kl}\,|a_l\rangle \quad k = 1, 2, \dots n. \tag{3.2.20}$$

This relation tells us that the eigenvectors of $\hat{U}$ are related to the basis vectors in $\mathcal{B}$ by the discrete Fourier transform. Now we introduce a new unitary operator $\hat{V}$, which cyclically permutes the eigenvectors of $\hat{U}$ (and not the basis states) as follows

$$\begin{aligned} \hat{V}\,|u_k\rangle &= |u_{k-1}\rangle && (3.2.21)\\ \hat{V}\,|u_1\rangle &= |u_n\rangle && (3.2.22)\\ \hat{V}^n &= \mathbf{1}. && (3.2.23) \end{aligned}$$

For the same reasons, if we consider the eigenvalue equation of $\hat{V}$,

$$\hat{V}\,|v_l\rangle = v_l\,|v_l\rangle \tag{3.2.24}$$

it can be easily demostrated that the eigenvalues are, once again, the n roots of unity

$$v_l = e^{-i\frac{2\pi}{n}l} \quad l = 1, 2, \dots n \tag{3.2.25}$$

while the eigenvectos this time are exactly the elements of the initial orthonormal basis, namely:

$$|v_l\rangle = |a_l\rangle \quad l = 1, 2, \ldots n. \tag{3.2.26}$$

In this way, we have constructed two operators, $\hat{U}$ and $\hat{V}$, called *conjugated operators*, which have the same spectrum and such that each of them permutes cyclically in opposite direction the eigenvectors relative to the other operator, i.e.

$$\begin{aligned} \hat{U}\,|v_l\rangle &= |v_{l+1}\rangle \ \mathit{with}\ |v_{l+n}\rangle = |v_l\rangle & (3.2.27)\\ \hat{V}\,|u_k\rangle &= |u_{k-1}\rangle \ \mathit{with}\ |u_{k-n}\rangle = |u_k\rangle\,. & (3.2.28)\end{aligned}$$

We can consider respectively these relations as the finite dimensional counterpart of the spectral translations (3.2.10) and (3.2.11), that we have obtained from the continuous Weyl operators.
The action of $\hat{U}$ and $\hat{V}$ on a state do not commute. In fact, it can be seen that

$$\begin{aligned} \hat{V}\hat{U}\,|u_k\rangle &= e^{-i\frac{2\pi}{n}k}\,|u_{k-1}\rangle & (3.2.29)\\ \hat{U}\hat{V}\,|u_k\rangle &= e^{-i\frac{2\pi}{n}(k-1)}\,|u_{k-1}\rangle & (3.2.30)\end{aligned}$$

from which it follows that

$$\hat{U}\hat{V} = e^{i\frac{2\pi}{n}}\hat{V}\hat{U}. \tag{3.2.31}$$

This relation can be generalized to all the integer powers of the operators into

$$\hat{U}^l\hat{V}^k = e^{i\frac{2\pi}{n}kl}\hat{V}^k\hat{U}^l. \tag{3.2.32}$$

In this way, we can define the discrete Schwinger-Weyl group as the set of all products between $\hat{U}$ and $\hat{V}$ and their integer power equipped with the commutator (3.2.32), that we can equivalently write in the following form

$$[\hat{U}^k, \hat{V}^l] = (e^{i\frac{2\pi}{n}kl} - 1)\hat{V}^k\hat{U}^l. \tag{3.2.33}$$

This commutation law represents the finite dimensional generalization of (3.2.9) that we have found for the continuos Weyl group. The difference in this case is that, being in a discrete group, it is impossible to perform a differentiation, as in (3.2.12), to obtain a commutation relation that involves the presence of a "generator", as in (3.2.13). Note that now, not being able to consider infinitesimal transformations, the same concept of "generators" (like $\hat{E}$ and $\hat{A}$ in the continuous case) is meaningless. However, the procedure leading to (3.2.32) is successful in preserving the unitarity of the operators involved and this commutation law is a valid starting point for a gauge theory in which the local fields act on finite dimensional Hilbert spaces. Furhtermore, it can be shown [17] that by taking the limit $n \to \infty$, the Weyl continuous group is reached.

3.2.3 New approach: Schwinger-Weyl comparator

One might wonder what have to do the Weyl groups of the previous sections with our physical model of the lattice (1+1)d QED, defined in 2.6. The answer lies in the fact that, in the model, we have two hermitian operators on each link, $\hat{E}_{x,x+1}$ and $\hat{A}_{x,x+1}$, defined in a infinite dimensional Hilbert space, whose commutation relation is

$$[\hat{E}_{x,x+1}, \hat{A}_{x,x+1}] = i \tag{3.2.34}$$

that is the Heisenberg's algebra product. Therefore, if we consider their exponentials

$$\hat{U}_{x,x+1} = e^{-i\hat{A}_{x,x+1}} \tag{3.2.35}$$

$$\hat{V}_{x,x+1} = e^{-i\hat{E}_{x,x+1}} \tag{3.2.36}$$

they form a continuous Weyl group. Note that the first operator is exactly the comparator of the physical model, the second is related to the electric field. The group commutator (3.2.9) becomes

$$\hat{U}_{x,x+1}\hat{V}_{x,x+1} = e^{i}\hat{V}_{x,x+1}\hat{U}_{x,x+1} \tag{3.2.37}$$

which, as we have seen, implies the commutation relation (3.1.1) of our model. Our goal now is to pass from infinite to finite Hilbert spaces of the link operators. The innovative approach, compared to the QLM, consists in the use of the discrete Schwinger-Weyl group. Consider a n-dimensional Hilbert space for each link. We can then define on it two conjugated operators, $\widetilde{U}_{x,x+1}$ and $\widetilde{V}_{x,x+1}$, which have the same features of the operators described in the subsection 3.2.2. As a result, we have

$$\widetilde{U}^{n}_{x,x+1} = \mathbf{1} \tag{3.2.38}$$

$$\widetilde{V}^{n}_{x,x+1} = \mathbf{1} \tag{3.2.39}$$

$$\widetilde{U}^{k}_{x,x+1}\widetilde{V}^{l}_{x,x+1} = e^{i\frac{2\pi}{n}kl}\widetilde{V}^{l}_{x,x+1}\widetilde{U}^{k}_{x,x+1} \tag{3.2.40}$$

in which $k, l \in \mathbb{Z}$. We consider on each link the orthonormal bases of eigenvectors of $\widetilde{V}_{x,x+1} \Rightarrow \{|v_{k,x,x+1}\rangle\}_{1\leq k\leq n}$, called electric field basis, so it follows that

$$\begin{aligned}
\widetilde{V}_{x,x+1}\,|v_{k,x,x+1}\rangle &= e^{i\frac{2\pi}{n}k_{x,x+1}}\,|v_{k,x,x+1}\rangle \quad k_{x,x+1} = 1, \ldots n & (3.2.41)\\
\widetilde{U}_{x,x+1}\,|v_{k,x,x+1}\rangle &= |v_{k+1,x,x+1}\rangle & (3.2.42)\\
\widetilde{U}_{x,x+1}\,|v_{n,x,x+1}\rangle &= |v_{1,x,x+1}\rangle & (3.2.43)
\end{aligned}$$

We choose the unitary operator $\widetilde{U}_{x,x+1}$ as the new comparator in our model and $\widetilde{V}_{x,x+1}$ as the new conjugated operator. As a result, we have a significant difference respect to QLM. In fact, if we consider the electric field eigenvectors corresponding to the maximum and minimum eigenvalues, in QLM it results that

$$\begin{aligned}
\hat{U}_{QLM}\,|+S\rangle = \hat{S}^{+}_{x,x+1}\,|+S\rangle &= 0 & (3.2.44)\\
\hat{U}^{\dagger}_{QLM}\,|-S\rangle = \hat{S}^{-}_{x,x+1}\,|-S\rangle &= 0 & (3.2.45)
\end{aligned}$$

while with the new comparator, it follows

$$\begin{aligned}
\widetilde{U}_{x,x+1}\,|v_{n,x,x+1}\rangle &= |v_{1,x,x+1}\rangle & (3.2.46)\\
\widetilde{U}^{\dagger}_{x,x+1}\,|v_{1,x,x+1}\rangle &= |v_{n,x,x+1}\rangle\,. & (3.2.47)
\end{aligned}$$

So, we get a truly cyclicity of the electric field values in our model, which can be represented as n equidistant points placed on a circle.

3.2.4 Z_n lattice model

We shall start once again from the lattice (1+1)d QED Hamiltonian (2.6.16) and we consider, in particular, the electric field term in it

$$\frac{g^2}{2}\sum_x \hat{E}^2_{x,x+1}. \tag{3.2.48}$$

Under the new approach, we have established the correspondence $\hat{E}_{x,x+1} \rightarrow \widetilde{V}_{x,x+1} = e^{-i\hat{E}_{x,x+1}}$. As a result, this term, which is positive, unbounded and vanishes only when the electric field is zero on each link, must be replaced with a suitable function of the operators $\widetilde{V}_{x,x+1}$. Obviously, this function must be diagonal in the electric field basis and in the continuum limit $n \rightarrow \infty$, has to tend to the original term (3.2.48). Although there is arbitrariness, a simple choice is [26]

$$f(\widetilde{V}_{x,x+1}) = \frac{(\widetilde{V}_{x,x+1} - \mathbf{1})(\widetilde{V}^{\dagger}_{x,x+1} - \mathbf{1})}{(2\pi/n)}. \tag{3.2.49}$$

This new operator on each link is Hermitian, its bounded and discrete eigenvalues are

$$S(k_{x,x+1}) = \frac{4\sin^2(\pi k_{x,x+1}/n)}{(2\pi/n)^2}. \tag{3.2.50}$$

This relation has a single minimum, which is zero and corresponds to $k_{x,x+1} = 0$. Also, this spectrum is quadratic around this minimum, like a $\hat{E}^2$term, but compared to the latter, it is deformed at the edges of the $k_{x,x+1}$-domain. As a result, $f(\widetilde{V}_{x,x+1})$ approximates the electric field energy only for low energy states: however the approximation improves when n increases. In addition, if we consider the continuum limit, it results that

$$\lim_{n\to\infty} \frac{4\sin^2(\pi k_{x,x+1}/n)}{(2\pi/n)^2} = k^2_{x,x+1} \tag{3.2.51}$$

that is the required condition.
Finally, we can write the Hamiltonian of our lattice (1+1)d QED model

$$\hat{H} = -t\sum_x \hat{\psi}^{\dagger}_x \widetilde{U}_{x,x+1}\hat{\psi}_{x+1} + \text{h.c.} + m\sum_x (-1)^x \hat{\psi}^{\dagger}_x\hat{\psi}_x + \frac{g^2}{2}\sum_x f(\widetilde{V}_{x,x+1}). \tag{3.2.52}$$

The Hilbert space is the tensor product of the Hilbert spaces relative to each site and each link:

$$\mathcal{H} = \left\{ \prod_x |n^F_x\rangle \otimes \prod_k |v_{k,x,x+1}\rangle \right\} \tag{3.2.53}$$

in which $n^F_x = 0, 1$ is the fermion occupation number of a site and $|v_{k,x,x+1}\rangle$ is an element of the electric field basis, which represents the electric field on a link.
It can be easily shown that, due to the commutation law (3.2.40), the Hamiltonian (3.2.48) is invariant under the local gauge trasformation performed by the operator

$$\hat{T}[\alpha_x] = \prod_x T_x(\alpha_x) = \prod_x e^{i\alpha_x \frac{2\pi}{n}(\hat{\psi}^{\dagger}_x\hat{\psi}_x + \frac{(-1)^x - 1}{2})} \widetilde{V}_{x,x+1}\widetilde{V}^{\dagger}_{x,x+1} \tag{3.2.54}$$

in which $\alpha_x \in \mathbb{Z}$. Since it results that $T_x^n = \mathbf{1}$, the $U(1)$ gauge symmetry of the original theory, which we have proved in the section 2.6, becomes a Z_n symmetry.

In this framework, the Hilbert subspace of physical gauge invariant states is determined by a generalized Gauss's law:

$$T_x \left|\phi\right\rangle = 0 \quad \forall x \tag{3.2.55}$$

which translates into a condition on the eigenvalues n_x^F and $v_{k,x,x+1}$ relative to physical states:

$$e^{i\frac{2\pi}{n}(n_x^F + \frac{(-1)^x - 1}{2})} v_{k,x,x+1} v_{k,x-1,x}^* = 1. \tag{3.2.56}$$

This equation allows us to understand how the physical states can be built: if an even site x is empty, i.e. $n_x^F = 0$, the eigenvalues of $\widetilde{V}$ in neighboring links must be equal, while if it is occupied, i.e. $n_x^F = 1$, it must result that $v_{k,x,x+1} = e^{-i\frac{2\pi}{n}} v_{k,x-1,x}$. Instead, if a odd site x is empty, it follows that $v_{k,x,x+1} = e^{i\frac{2\pi}{n}} v_{k,x-1,x}$, while if it is occupied, the eigenvalues of $\widetilde{V}$ are equal. Note that, in agreement to the definition of staggered vacuum, the absence of a particle in a odd site (negative energy state) is equivalent to the presence of an antiparticle. Furthermore, the equation (3.2.42) tells us that the operator $\widetilde{U}_{x,x+1}$ performs a counterclockwise discrete rotation of the eigenstates of $\widetilde{V}$, while $\widetilde{U}_{x,x+1}^\dagger$ a clockwise rotation.

In the next chapters, we will study some interesting aspects of this Z_n lattice model of (1+1)d QED.

Chapter 4

Numerical analysis

In this chapter, we analyze the discrete Z_n lattice model, which represents the lattice version of the QED in (1+1) dimensions, setting $n = 3$.

4.1 Characterization of a suitable Hilbert space

Due to the use of staggered fermions in our lattice model, as we have seen, a split between even and odd sites occurs: the first ones correspond to positive energy states, the latter to negative energy states. As a result, the presence (absence) of a fermion on a even (odd) site can be considered as the presence of a particle (antiparticle), also called quark (antiquark). If x is an even site, the fermionic configurations are shown in Fig. 4.1.1.

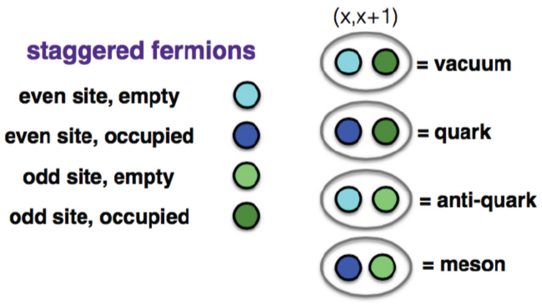

Figure 4.1.1: Fermionic configurations on a couple of sites $(x, x + 1)$.

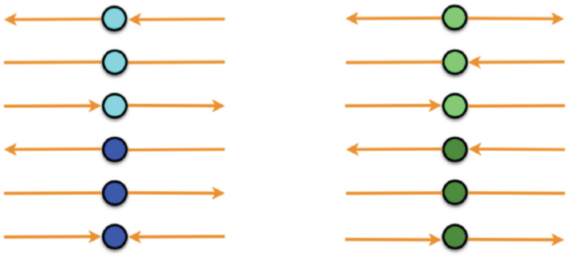

Figure 4.1.2: Even/odd site configurations which respect the Gauss law.

We work with $n = 3$, so there are three possible electric field states on a link, i.e. the three eigenvectors of the operator $\widetilde{V}_{x,x+1}$ that we can label with $k_{x,x+1} = -1, 0, 1$. We pictorially interpreted this states as configurations in which the electric field is respectively oriented to the left, non-oriented, oriented to the right.

The Hilbert space associated to a site x and the two neighboring links is, in principle, $d_1 = 3\times2\times3 = 18$ dimensional, but, due to the Gauss law (3.2.56), the allowed configurations decrease, as it can be seen in Fig. 4.1.2, so $d_1 = 6$. We can denote this states by $\left|k_x^L, n_x^F, k_x^R\right\rangle$, in which $k_x^L, k_x^R = -1, 0, 1$ and $n_x^F = 0, 1$.

The Hilbert space of N neighboring sites, with open boundary conditions, can be constructed with linear combinations of states having the tensor product form

$$\left|k_1^L, n_1^F, k_1^R\right\rangle \otimes \left|k_2^L, n_2^F, k_2^R\right\rangle \otimes \ldots \otimes \left|k_N^L, n_N^F, k_N^R\right\rangle \tag{4.1.1}$$

in which the right electric field of a site must be egual to the left electric field of the next site, so $k_{x_j}^R = k_{x_{j+1}}^L$. The whole configuration of the chain, due to the Gauss law, depends only on the presence/absence of fermions on all sites (2^N possibilities) and on the left electric field of the first site (3 possible configurations). As a result, the Hilbert space of the N-chain has total dimension $d_N = 3 \times 2^N$.

In our numerical analysis, we will use the physical Hilbert space $\mathcal{H}_\alpha$ associated to a couple of neighboring sites $(x, x+1)$, in which the first is even, the latter is odd. According to the previous reasoning, it follows that

$$\mathcal{H}_\alpha = Span\left\{\left|n_1^F, n_2^F, M\right\rangle = \left|k_1^L, n_1^F, k_1^R\right\rangle \otimes \left|k_1^R, n_2^F, k_2^R\right\rangle\right\} \tag{4.1.2}$$

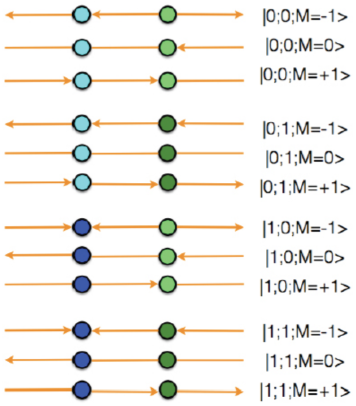

Figure 4.1.3: Hilbert space basis for a couple of sites.

in which $n^F_{1/2} = 0, 1$ and $M = k^L_1 = -1, 0, 1$. Its dimension is $d_\alpha = 12$ and it is convenient to make explicit all these basis elements in Fig. 4.1.3, because we will use them, in a ordered way, as the starting point of our study. Notice that the Hilbert space is composed of four subspaces, labelled by the fermionic occupation numbers, each of which is three-dimensional due to the presence of three electric field configurations on the first link.

4.2 Hamiltonian decomposition

Recall that the Hamiltonian of our model is written in the following form

$$\hat{H} = -t\sum_x \hat{\psi}^\dagger_x \widetilde{U}_{x,x+1}\hat{\psi}_{x+1} + \text{h.c.} + m\sum_x (-1)^x \hat{\psi}^\dagger_x \hat{\psi}_x + \frac{g^2}{2}\sum_x f(\widetilde{V}_{x,x+1}). \quad (4.2.1)$$

Working with a Z_3 symmetry, we can choose the function $f(\widetilde{V}_{x,x+1})$ in the simplest way: we associate an energy $\frac{g^2}{2}$ to each link with nonzero electric field. Clearly, this energy vanishes when the electric field on a link is zero. Therefore, we can replace the above function with a term proportional to $\hat{E}^2_{x,x+1}$. It follows that

$$\hat{H} = -t\sum_x \hat{\psi}^\dagger_x \widetilde{U}_{x,x+1}\hat{\psi}_{x+1} + \text{h.c.} + m\sum_x (-1)^x \hat{\psi}^\dagger_x \hat{\psi}_x + \frac{g^2}{2}\sum_x \hat{E}^2_{x,x+1}. \quad (4.2.2)$$

This Hamiltonian is written as a sum over all lattice sites. We can group this sites two by two (even and odd) and rewrite it as a sum over couples: (henceforth we neglect the operatorial notation)

$$\begin{aligned} H &= -t\sum_{\alpha}(\psi^{\dagger}_{\alpha E}U_{\alpha E,\alpha O}\psi_{\alpha O} + \text{H.c.}) && (4.2.3)\\ &+ -t\sum_{\alpha}(\psi^{\dagger}_{\alpha O}U_{\alpha O,\alpha+1,E}\psi_{\alpha+1E} + \text{H.c.}) && (4.2.4)\\ &+ m\sum_{\alpha}(\psi^{\dagger}_{\alpha E}\psi_{\alpha E} - \psi^{\dagger}_{\alpha O}\psi_{\alpha O}) && (4.2.5)\\ &+ \frac{g^2}{2}\sum_{\alpha}(E^2_{\alpha-1O,\alpha E} + E^2_{aE,\alpha O} + E^2_{\alpha O,\alpha+1E}). && (4.2.6)\end{aligned}$$

The term (4.2.3) describes the hopping of a fermion between the even and odd sites inside the same couple. The term (4.2.4) instead moves a fermion from the odd site of the couple α to the even site of the next couple $\alpha+1$ and viceversa. The term (4.2.5) is relative to the staggered mass energy. The last term (4.2.6) represents the energy of the electric field on each link included in the couple or between two couples.
Our goal now is to write any term in the sums as a tensor products of operators defined on $\mathcal{H}_{\alpha}\otimes\mathcal{H}_{\alpha+1}$, which are respectively the Hilbert space of the couple α and $\alpha+1$, by using the ordered basis of Fig. 4.1.3.

- Kinetic term (4.2.3): the first piece of the kinetic energy acts on fixed couple and can be written in the form:

  $$(-t)(\mathbb{K}+\mathbb{K}^{\dagger})_{\alpha}\otimes\mathbb{I}_{\alpha+1}. \tag{4.2.7}$$

  The 12×12 matrix $\mathbb{K}$ gives non-zero only when the odd site is occupied and the even site is empty. Viceversa for the $\mathbb{K}^{\dagger}$ matrix. $\mathbb{I}_{\alpha+1}$ is the identity matrix in the space $\mathcal{H}_{\alpha+1}$. If we define a three dimensional matrix

  $$\mathbb{P} = \begin{bmatrix} 0 & 0 & 1\\ 1 & 0 & 0\\ 0 & 1 & 0 \end{bmatrix} \tag{4.2.8}$$

  it follows that

  $$\mathbb{K} = \begin{bmatrix} 0 & 0 & 0 & 0\\ 0 & 0 & 0 & 0\\ 0 & \mathbb{P} & 0 & 0\\ 0 & 0 & 0 & 0 \end{bmatrix} \Rightarrow \mathbb{K}+\mathbb{K}^{\dagger} = \begin{bmatrix} 0 & 0 & 0 & 0\\ 0 & 0 & \mathbb{P}^{\dagger} & 0\\ 0 & \mathbb{P} & 0 & 0\\ 0 & 0 & 0 & 0 \end{bmatrix}. \tag{4.2.9}$$

- Kinetic term (4.2.4): the second piece of the kinetic energy acts between two nearby couples and it can be written in the form

$$(-t)(\mathbb{J}_\alpha \otimes \mathbb{T}_{\alpha+1} + \mathbb{J}^\dagger{}_\alpha \otimes \mathbb{T}^\dagger_{\alpha+1}). \tag{4.2.10}$$

  in which, due to the use of our ordered basis, the matrices $\mathbb{J}$ and $\mathbb{T}$ look as

$$\mathbb{J} = \begin{bmatrix} 0 & 0 & 0 & 0 \\ \mathbb{I} & 0 & 0 & 0 \\ 0 & 0 & 0 & 0 \\ 0 & 0 & \mathbb{I} & 0 \end{bmatrix} \qquad \mathbb{T} = \begin{bmatrix} 0 & 0 & \mathbb{I} & 0 \\ 0 & 0 & 0 & \mathbb{I} \\ 0 & 0 & 0 & 0 \\ 0 & 0 & 0 & 0 \end{bmatrix} \tag{4.2.11}$$

  in which $\mathbb{I}$ is the 3×3 identity matrix.

- Mass term (4.2.5): it can be easily written as

$$m(\mathbb{M}_\alpha \otimes \mathbb{I}_{\alpha+1}) \tag{4.2.12}$$

  with

$$\mathbb{M} = \begin{bmatrix} 0 & 0 & 0 & 0 \\ 0 & -\mathbb{I} & 0 & 0 \\ 0 & 0 & \mathbb{I} & 0 \\ 0 & 0 & 0 & 0 \end{bmatrix}. \tag{4.2.13}$$

- Electric field term(4.2.6): if we consider the left link and the central link of the couple α, this term can be written as

$$\frac{g^2}{2}(\mathbb{L}^2 + \mathbb{C}^2) \otimes \mathbb{I}_{\alpha+1} \tag{4.2.14}$$

  provided that a term which represents the configuration of the right link of the last couple on the chain is added. This last term can be written as

$$\frac{g^2}{2}(\mathbb{I}_1 \otimes \mathbb{I}_2 \otimes \ldots \otimes \mathbb{I}_\alpha \otimes \mathbb{I}_{\alpha+1} \otimes \ldots \otimes \mathbb{R}^2). \tag{4.2.15}$$

  In this relations, $\mathbb{L}, \mathbb{C}, \mathbb{R}$ are the following diagonal matrices:

$$\mathbb{L} = \begin{bmatrix} \mathbb{M}_0 & 0 & 0 & 0 \\ 0 & \mathbb{M}_0 & 0 & 0 \\ 0 & 0 & \mathbb{M}_- & 0 \\ 0 & 0 & 0 & \mathbb{M}_- \end{bmatrix} \tag{4.2.16}$$

$$\mathbb{C} = \begin{bmatrix} \mathbb{M}_0 & 0 & 0 & 0 \\ 0 & \mathbb{M}_0 & 0 & 0 \\ 0 & 0 & \mathbb{M}_0 & 0 \\ 0 & 0 & 0 & \mathbb{M}_0 \end{bmatrix} \tag{4.2.17}$$

$$\mathbb{R} = \begin{bmatrix} \mathbb{M}_- & 0 & 0 & 0 \\ 0 & \mathbb{M}_0 & 0 & 0 \\ 0 & 0 & \mathbb{M}_- & 0 \\ 0 & 0 & 0 & \mathbb{M}_0 \end{bmatrix} \tag{4.2.18}$$

in which we have used the 3×3 diagonal matrices

$$\mathbb{M}_0 = diag\,[-1, 0, +1] \tag{4.2.19}$$

$$\mathbb{M}_- = diag\,[+1, -1, 0] \tag{4.2.20}$$

$$\mathbb{M}_+ = diag\,[0, +1, -1]\,. \tag{4.2.21}$$

This decomposition allows us to write the entire Hamiltonian of L couples as a sum of tensor products of the previous matrices. This is a significant starting point for numerical processing. In the following analysis, we consider a number of particles equal to the number of couples (as in the staggered vacuum). This, in the quark/antiquark picture, means to consider the sector of the Hilbert space with a total charge $Q = 0$.

4.3 Exact diagonalization for small sizes

Suppose we consider a generic number of couples L. If we write the Hamiltonian of the whole system with the decomposition of the previous section, it will be defined in an Hilbert space of dimension $d = 12^L$. However, this space is too large because it contains also non-physical states: in fact, in the tensor product of matrices, it is not taken into account that the right link of a couple must coincide with the left link of the next couple. Due to this, each state of the ordered basis (Fig. 4.1.3) can be connected only with four states of the next couples. As a result, the physical Hilbert space has dimension $d_L = 12 \times 4^{L-1} = 3 \times 4^L$. This result, taking into account that we are using the number of couples L instead of N (number of sites), coincides with the dimension of the Hilbert space that we have found in section 4.1.

In this thesis work, the first step has consisted in the developing of a program in *Mathematica* that can restrict the Hamiltonian on the physical subspace

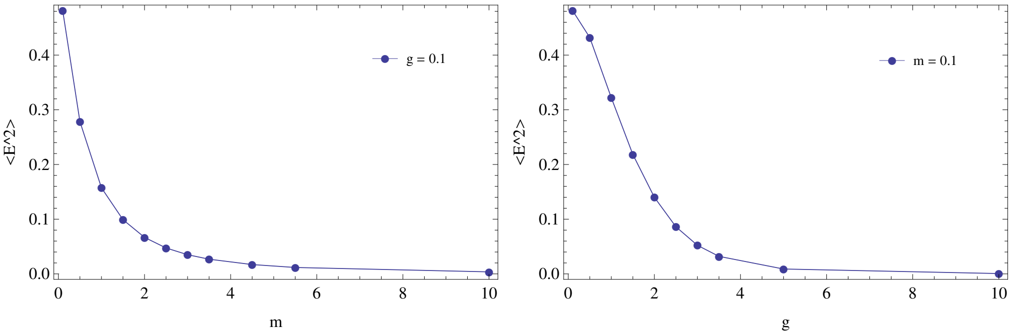

Figure 4.3.1: Plots of $\langle E^2 \rangle$ as a function of m (left), of g (right) for $L = 2$.

and perfom an exact diagonalization for small L (see Appendix A).
Our goal is the characterization of the phase diagram (g, m), by varying this two parameters and setting $t = 1$. For this purpose it is convenient to consider some limit cases first.
We can reasonably expect that, when $m \gg g$, the ground-state (GS) coincides with the staggered fermions vacuum, i.e. a filled Dirac sea of negative energy states (all odd sites filled) with a zero electric field on each link. The same for $g \gg m$, since the presence of a non vanishing electric field would be energetically disadvantaged. When m and g are of the same order and comparable to the value of t, there is a particular competition between the kinetic term on the one hand and the mass and the electric field terms on the other: in fact, due to the particular coupling, the kinetic term tends to move the fermions, activating mass and electric field excitations. For our study, it is convenient to define as order parameter the expectation value of the whole "quadratic" electric field in the GS:

$$\langle E^2 \rangle = \frac{1}{L} \sum_x \langle E^2_{x,x+1} \rangle_{GS} \,. \tag{4.3.1}$$

The square is needed in order to distinguish the vacuum, which has identically $E_{x,x+1} = 0$, from the other possible configurations with positive and negative electric fields on the various links.
We shall start studying the introductory, but interesting, case, with $L = 2$. With an exact diagonalization of the physical Hamiltonian, it is calculated the order parameter with various values of m and g. The results are presented in Fig. 4.3.1. It is clearly visible an exponential decay of $\langle E^2 \rangle$ when we move in the phase diagram along the horizontal line $g = 0.1$ or along the vertical

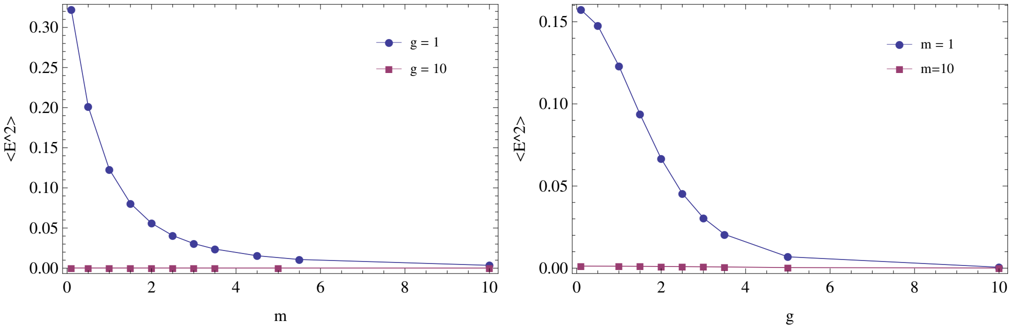

Figure 4.3.2: Plots of $\langle E^2 \rangle$ as a function of m (left) and g (right), $L = 2$.

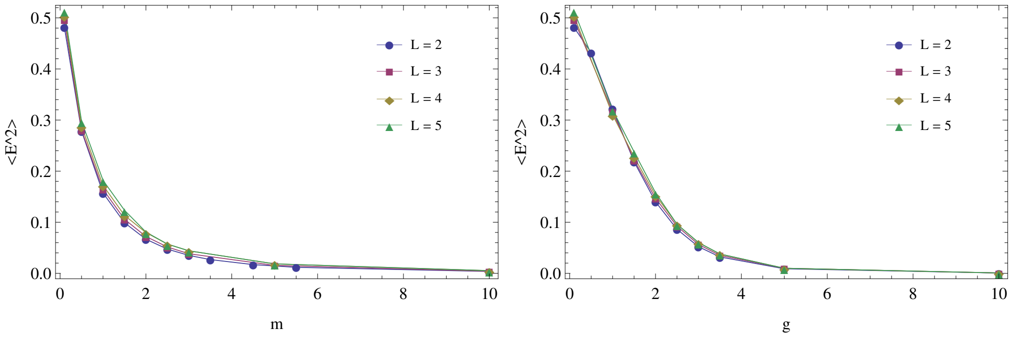

Figure 4.3.3: Plots with $g = 0.1$ (left) and $m = 0.1$ (right) for different L.

line $m = 0.1$ with increasing values of the other parameter. This situation persists when we consider the lines $g = 1$ or $m = 1$, while it is completely absent when we set $g = 10$ or $m = 10$: in this case, the order parameter is pratically zero everywhere, as we can see in Fig. 4.3.2.

Altought in the present case these trends might be due to finite-size effects and, in principle, we can not say anything about the presence of a crossover or a phase transition, it is interesting to note that the case with $L = 2$ captures many physical properties which remain unaffected by increasing the size of the system. In fact, if we consider the cases with $L = 3, 4, 5$, which have been solved exactly as well, the trends of the order parameter are very similar, as it results in the comparative plots of Fig. 4.3.3.

In order to understand what happens to the system while we vary g and m, we can characterize its GS by studying two local properties: the expectation value of n_x^F and $E_{x,x+1}$, i.e. the fermionic lattice density and the mean electric field on each link. It results that, regardless of the size $L = 2, 3, 4, 5$,

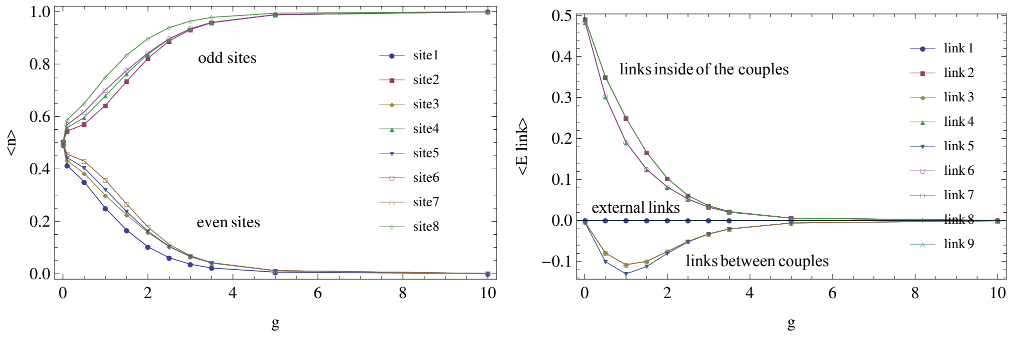

Figure 4.3.4: Plots of $\left\langle n_x^F \right\rangle$ (left) and $\langle E_{x,x+1}\rangle$ (right) as a function of g, with $m = 0.01$ and $L = 4$

the system passes from a configuration in which we have

$$\left\langle n_x^F \right\rangle \approx \frac{1}{2} \quad \forall x \tag{4.3.2}$$

$$\langle E_{x,x+1}\rangle \approx \begin{cases} 0 & x \text{ even} \\ \frac{1}{2} & x \text{ odd} \end{cases} \tag{4.3.3}$$

to another in which

$$\left\langle n_x^F \right\rangle \approx \begin{cases} 0 & x \text{ even} \\ 1 & x \text{ odd} \end{cases} \tag{4.3.4}$$

$$\langle E_{x,x+1}\rangle \approx 0 \quad \forall x \tag{4.3.5}$$

by increasing the values of m or g, as it is shown in Fig. 4.3.4. This means that when m or g are larger than certain values, the GS coincides with the filled Dirac sea, as expected. When m and g tend to zero the GS of the system is a delocalized state, in which the expectation value of the occupation number is the same for each site, and with a particular configuration of the electric field: on the external links of the chain its expectation value is identically zero; on the links inside of couples, it is large and positive; on the links between couples it is zero.

A better characterization is possible if we understand which elements of our ordered basis appear in GS. With $L = 2$, it results that the GS is a superposition of the states listed in Fig. 4.3.5a. In the associated quark picture, this states correspond to the vacuum, meson states, an antimeson state, a pairs

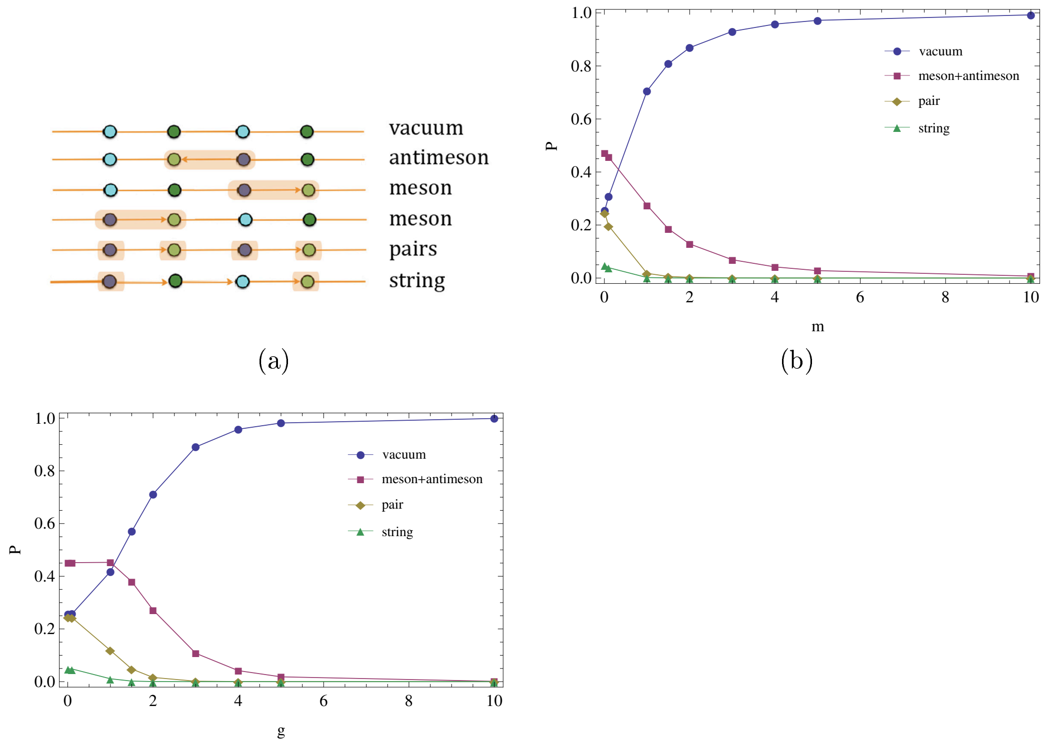

(a) (b)

(c)

Figure 4.3.5: (a) Components of the GS for $L = 2$. (b) Probability amplitudes as a function of m with $g = 0.01$ for $L = 2$. (c) Probability amplitudes as a function of g with $m = 0.01$ for $L = 2$.

state and a string state. Note that on the external links the electric field is always zero and, a consequence, the mesons can only be created inside of the couples, while the antimeson states only between couples with an opposite electric field. Furthermore, in the pair state all the masses are excited forming charge-anticharge pairs, while in the string state two mass excitations are present at the boundaries, and all electric fields connecting the two are positive. It is interesting to analyze the probability amplitudes of these different components of the GS (Fig. 4.3.5b and Fig. 4.3.5c): when m and g are very small, the GS is dominated by the meson states (including equivalently the antimeson state). When we increase m or g, there is a particular coexistence of the meson/antimeson states, the vacuum and the pair state as long as the vacumm becomes completely dominant.

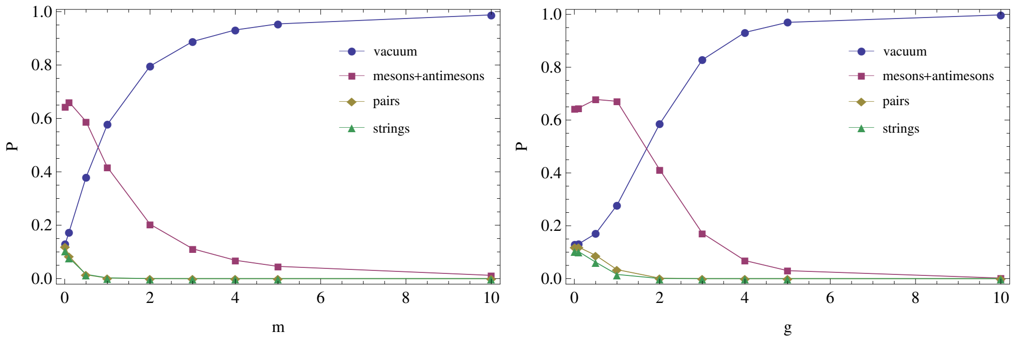

(a) (b)

Figure 4.3.6: (a) Proability amplitudes as a function of m with $g = 0.01$ for $L = 3$. (b) Proability amplitudes as a function of g with $m = 0.01$ for $L = 3$.

This behavior is also found in a clear manner in the cases with $L = 3, 4, 5$: in fact, increasing the size of the system, there is a remarkable rise of the total meson/antimeson amplitudes at the expense of the other components, as shown in Fig. 4.3.6a and Fig. 4.3.6b for $L = 3$. In these plots we can also see that in the transition between the two limit configurations, identified by the local properties (4.3.2) and (4.3.4), the involved components become essentially two: meson/antimeson states and vacuum. Recalling that the meson states can be created only inside the couples (with a positive electric field), while the antimeson states only between couples (with a negative electric field), let us go back to what we have found by studying the fermionic lattice density $\langle n_x^F \rangle$ and the mean electric field on each link $\langle E_{x,x+1} \rangle$ in Fig. 4.3.4: the fact that on the links between couples $\langle E_{x,x+1} \rangle$ is pratically zero when m and g are very small (~ 0.01), tells us that the GS in this case corresponds to a superposition of meson states (with multiple possible mesons) without antimesons. The "hopping" of this mesons on the whole chain justifies the limit occupation value $\langle n_x^F \rangle = \frac{1}{2}$ on each site and determines the condition $\langle E_{x,x+1} \rangle = \frac{1}{2}$ on the links inside of the couples. All of this is possible because the probability amplitudes of the meson components in the GS, which have been calculated in our computation, have the same value, so for example when $L = 3$ and m and g are very small, we are approximately in the following situation for the GS (excluding the components with small amplitudes that, as we have seen, decrease with increasing L):

$$\begin{aligned}|GS\rangle &\approx \frac{1}{\sqrt{6}}\{|9,5,5\rangle + |5,9,5\rangle + |5,5,9\rangle \\ &+ |9,9,5\rangle + |9,5,9\rangle + |5,9,9\rangle\}\end{aligned} \tag{4.3.6}$$

in which $|a,b,c\rangle = |a\rangle\,|b\rangle\,|c\rangle$ represents the states of the three couples in our ordered basis of Fig. 4.1.3. The state $|9\rangle$ corresponds to a meson, the state $|5\rangle$ to the vacuum, so $|GS\rangle$ is a superposition of states in which one or two mesons move on the chain. It is easy to see that on this state it results that $\left\langle n_x^F \right\rangle = \frac{1}{2}$ for each site, $\langle E_{x,x+1}\rangle = \frac{1}{2}$ for the links inside of couples and $\langle E_{x,x+1}\rangle = 0$ for the links between couples, exactly as we have found in our analysis.

The absence of antimeson components in the GS may be due to the finite (small) size of the system, which can break a possible degeneration of the fundamental energy level, favouring a completely meson state at the expenses of the antimesonic components.

However, we can note that when we increase slightly m or g, there is a small rise of the amplitudes of the total meson/antimeson components (Fig. 4.3.6a and Fig. 4.3.6b): we can attribute this rise to the "activation" of antimeson components in order to justify the small negative peak of the mean electric field on the links between couples, Fig. 4.3.4.

To sum up, we have found an interesting property in our analysis with small sizes: there is a particular region in the phase diagram (m, g), in which the GS of the system does not correspond to the vacumm, but a state with mass and field excitations due to the presence of mesons and antimesons.

Starting from these considerations, we can study in detail the phase diagram with different values of L. We have considered the value $\langle E^2\rangle_0$ of the order parameter in ($m = 0.01$, $g = 0.01$) as reference and have determined the points (m, g) in which $\langle E^2\rangle = 0.03\,\langle E^2\rangle_0$. The phase diagram obtained with $L = 2, 3, 4, 5$ is shown in Fig.4.3.7a. It is possible to note a slight shift of the transition line with the increasing of the size. This effect has been quantitatively estimated by evaluating the distances δ between the points with $g = 1$. A logarithmic plot of this parameter shows us a clear exponential decay, Fig. 4.3.7b. As a result, we can reasonably expect that by increasing the size of the system at large values of L, the phase diagram retains the properties that have been analyzed in this section.

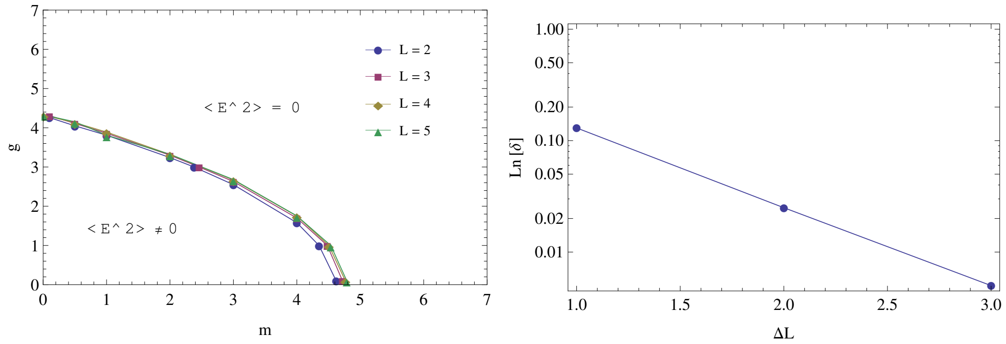

(a) (b)

Figure 4.3.7: (a) Phase diagram $g - m$ with different sizes L of the system. (b) Logarithmic plot of the δ as a function of differences between sizes.

4.4 DMRG - numerical results

The DMRG (Density Matrix Renormalization Group) algorithm is a variational method that enables us to study numerically our model, providing accurate information about the lowest part of the spectrum and various properties of the GS (see Appendix B). In this work, this algorithm has been used to study the phase diagram of our system with a considerable size L. The goal is to capture all the properties of the thermodynamic limit ($L \to \infty$). However, recalling that L is the number of couples and, therefore, we have a chain with a double number of sites and related links, it results that the computational costs for large sizes are very high (memory used, computation time, etc.). An efficient compromise is the case with $L = 20$ that we study in the following.

First of all, we analyze the order parameter as a function of g and m: as in the previous cases with small sizes, when we move along the orizontal/vertical lines with fixed m/g, it results an exponential decay of $\langle E^2 \rangle$ in a specific region of the phase diagram, i.e. when the fixed parameter exceeds a certain value this effect disappears, Fig. 4.4.1a and 4.4.1b.

We can study now two local properties of the GS: we consider the expectation values $\langle n_x^F \rangle$ and $\langle E_{x,x+1} \rangle$ as in the previous section. In Fig. 4.4.1c and 4.4.1d we can see the behavior of this quantities for two sites (even and odd) and for two links (one inside of a couple, the other between two couples) of the chain. On the other sites and links of the same type, the situation is quite

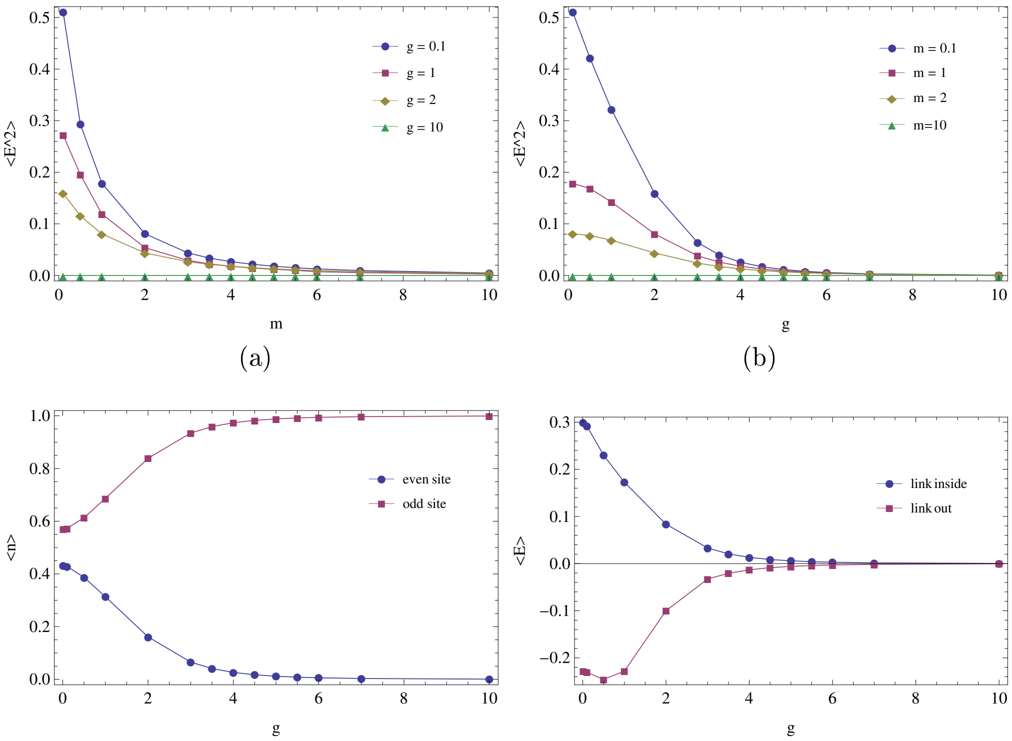

(a) (b)

(c) (d)

Figure 4.4.1: The order parameter $\langle E^2 \rangle$ as a function of m (a), g (b) with $L = 20$. (c) Plots of $\langle n_x^F \rangle$ for two sites (even and odd) as a function of g, with $m = 0.1$ and $L = 20$ (d) Plots of $\langle E_{x,x+1} \rangle$ for two links (inside of a couple/between couples) as a function of g, with $m = 0.1$ and $L = 20$.

identical. It is immediately noted that we have the same trends of the previous section: this is very important in order to characterize the GS, because with the DMRG-algorithm we do not get the probability amplitudes of the various components that flow in it. However, through the analysis with small sizes, we have shown that this typical trends are related to meson/antimeson states, which become completely dominant over the vacuum and the other components for small values of the parameters. We can note an important difference compared to the case with small sizes: here, when m and g are very small (~ 0.01), the mean electric field $\langle E_{x,x+1} \rangle$ on links between couples does not go to zero, but takes negative values comparable with those on the links inside of couples, which now are smaller than $\frac{1}{2}$. Moreover, the mean occupation value $\left\langle n_x^F \right\rangle$ does not tend to $\frac{1}{2}$, but it assumes greater values for the odd sites, smaller values for the even sites. This tells us that the antimeson components remain present in the GS. In fact, suppose to consider for simplicity an ideal chain with $L = 3$ without small size effects. Recalling that the probability amplitudes of the meson/antimeson components of the GS have essentially the same values as we have shown in the previous section, we can consider a generalization of the state (4.3.6) by including the antimeson components:

$$\begin{aligned} |GS\rangle &\approx \frac{1}{\sqrt{11}}\{|9,5,5\rangle + |5,9,5\rangle + |5,5,9\rangle + |9,9,5\rangle \\ &+ |9,5,9\rangle + |5,9,9\rangle + |2,11,5\rangle + |5,2,11\rangle \\ &+ |2,8,11\rangle + |2,11,9\rangle + |9,2,11\rangle\} \end{aligned} \tag{4.4.1}$$

in which the states $|5\rangle$ corresponds to the vacuum configuration for a couple, the state $|9\rangle$ to a meson, the $|2, 11\rangle = |2\rangle |11\rangle$ to an antimeson that can be created only between couples. In this configuration we have all possible states allowed by Gauss'law with a number of mesons and antimesons between 1 and $L - 1$. Recall that a state of the form $|9, 9, 9\rangle$ is a "pairs" state (Fig. 4.3.5a) and its probability amplitudes becomes pratically zero with the increase of the size, as we have seen in the previous section. For this reason we consider only states with a maximum of $L - 1$ mesons/antimesons in (4.4.1). It is easy to see that on this GS it results $\left\langle n_x^F \right\rangle \approx 0.45$ for even sites, $\left\langle n_x^F \right\rangle \approx 0.55$ for odd sites, $\langle E_{x,x+1}\rangle \approx 0.3$ for the links inside of couples, $\langle E_{x,x+1}\rangle \approx 0.25$ for the links between couples. If we consider a state of this type for the case with $L = 20$, this values are in agreement with what we have seen in the Fig. 4.4.1d.

As a result, we can conclude that the GS of the system, when m and g are small enough, is a superposition of meson and antimeson states. In a pictorial scheme, we can represent it as an hopping of multiple mesons and antimesons on the chain.

The relation (4.4.1) represents, clearly, a first approximation of the GS of the system, but it offers important cues for further researchs: for example, there might be a little difference in the probability amplitudes of meson and antimeson components, which could lead to a charge-symmetry breaking (see Chapter 5).

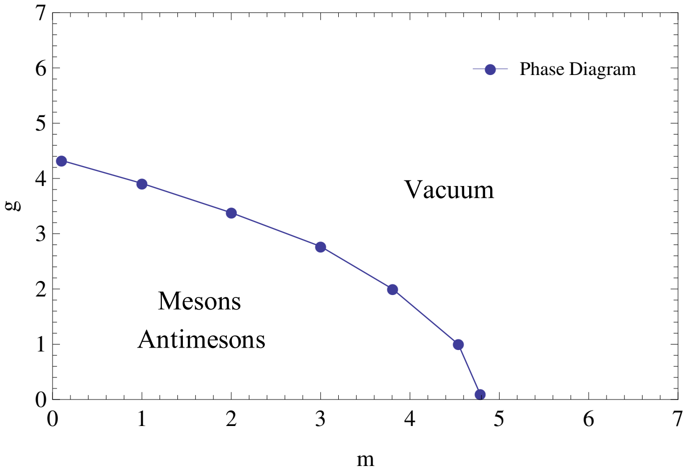

Figure 4.4.2: Phase diagram of the lattice Z_3 model for QED.

4.4.1 Finite size scaling

By a detailed study of the trends of the order parameter, which have been calculated by using the DMRG-algorithm, it is possible to determine the phase diagram of our model. The line has been traced with the same criterion of the previous section, i.e. $\langle E^2 \rangle = 0.03 \langle E^2 \rangle_0$ for $L = 20$. The result, which is one of the goals of this thesis work, is shown in Fig. 4.4.2.

We can perform now a finite size scaling of the order parameter $\langle E^2 \rangle$ in order to study how the phase diagram varies for different lattice sizes. We have considered three points: the first in “meson/antimeson” region ($m = 0.1, g = 0.1$), the second on the “transition” line ($m = 3.805, g = 2$), the third in the “vacuum” region ($m = 7, g = 7$). It results that $\langle E^2 \rangle$ always shows a particular behavior: it tends to saturate to a finite asymptotic value, as reported in Fig. 4.4.3. On the first point, this is immediately clear (Fig. 4.4.3a). On the second and third point, the data are in good agreement with a fit of the form $a - b/L$, in which a and b are two positive parameters. The analysis of the numerical values of these parameters (reported in Fig. 4.4.3b and Fig. 4.4.3c) tells us that when $L = 20$ the correction with respect to the asymptotic value of $\langle E^2 \rangle$ is extremely small ($b/L \approx 10^{-2}a$). Whereby, we can reasonably expect that the phase diagram, which in our analysis has been built with $L = 20$, remains practically unchanged when L further increases. This fact justifies the stability and the reliability of our phase diagram.

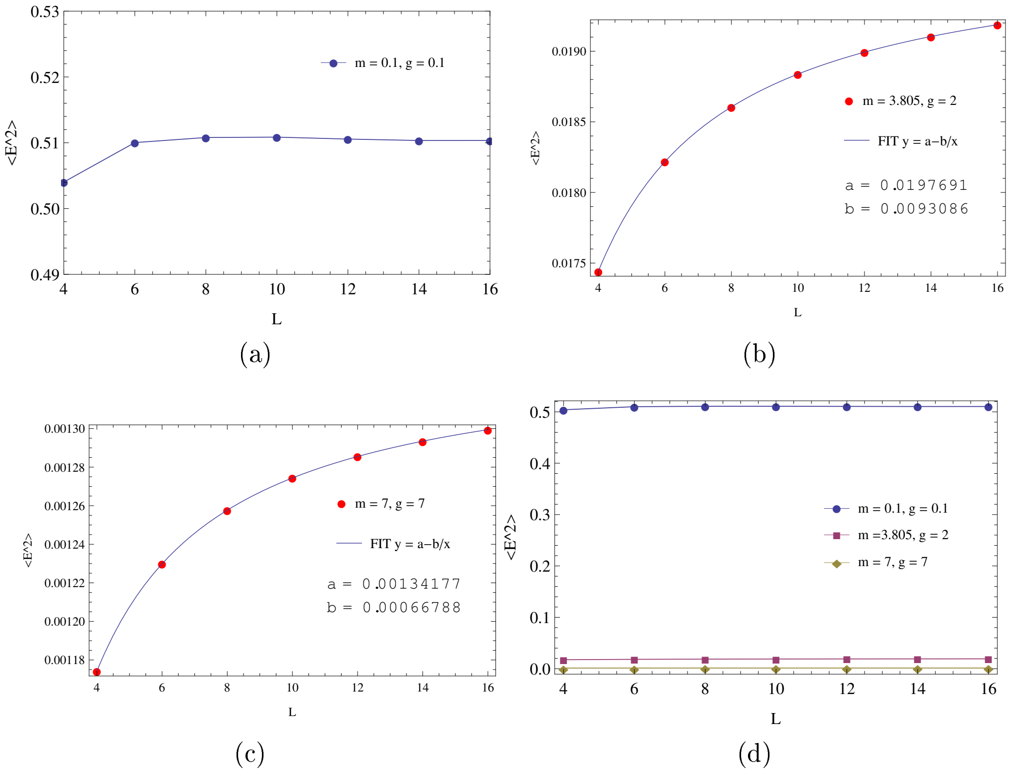

(a) (b)

(c) (d)

Figure 4.4.3: Finite size scaling of the order parameter for (a) $m = 0.1, g = 0.1$, (b) $m = 3.805, g = 2$, (c) $m = 7, g = 7$. (d) Comparative plot of the previous trends.

In Fig. 4.4.3d are overall shown the same trends: it can be qualitatively noted, in this case, as the dependence on L is really weak.

We can reasonably ask why the order parameter does not go to zero with the increase of the size L when $m = 7$ and $g = 7$, i.e. when we are completely in the "vacuum" phase. The answer lies in the boundary conditions: we are using open boundary conditions and this affects the values of the order parameter. We can analyze this effect by studying the mean (small) value of $\langle E_x \rangle$ on each link inside couples and between couples (here, the first and the last link of the chain correspond to the internal link of the first and the last couple): as we can see in Fig. 4.4.4a, inside couples $\langle E_x \rangle$ results positive (residual meson components) and tends to zero with increasing L except on the first and last link of the chain, where it increases. This is clearly a boundary effect, which determines the fact that the order parameter does

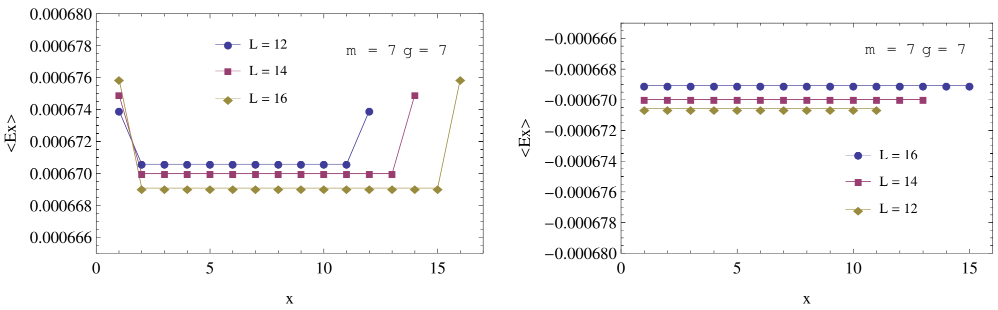

(a) (b)

Figure 4.4.4: (a) $\langle E_x \rangle$ on links inside couples. It is clearly visible a boundary effect. (b) $\langle E_x \rangle$ on links between couples.

not go exactly to zero. Instead, between couples $\langle E_x \rangle$, as we can expect, is negative (residual antimeson components) and tends to zero symmetrically with respect to the previous case, without boundary effects, Fig. 4.4.4b.
At this point, it is interesting to understand what happens to the system in the passage between the two configurations, i.e. mesons/antimesons↔vacuum. We can investigate this argument by studying the first two energy levels of the system (divided by size), E_0/L and E_1/L (the third level, in our numerical analysis, results always degenerate with the second). Suppose we move in the phase diagram along the two directions $g = 0.1$ (vertical) and $m = 0.1$ (horizontal): we obtain the trends of Fig. 4.4.5, in which there is also a comparison between the case with $L = 4$ and $L = 12$. We can notice some important features:

- the fundamental energy level $E0/L$ remains pratically unchanged with increasing size;
- the first level $E1/L$ instead tends to get closer to the fundamental energy in a range of g or m between zero and a certain maximum value;
- outside of the said range, the first level $E1/L$ tends to move away from the fundamental energy, as can be seen in the case with $L = 4$ and, more sharply, in the case with $L = 12$ (note in Fig. 4.4.5b the change of slope of $E1/L$ for $L = 12$ compared to the case with $L = 4$);

In order to understand if this effect persists in the case with $L \gg 1$, we can perform in both cases (vertical lines $m = 0.1$ and horizontal lines $g = 0.1$) a

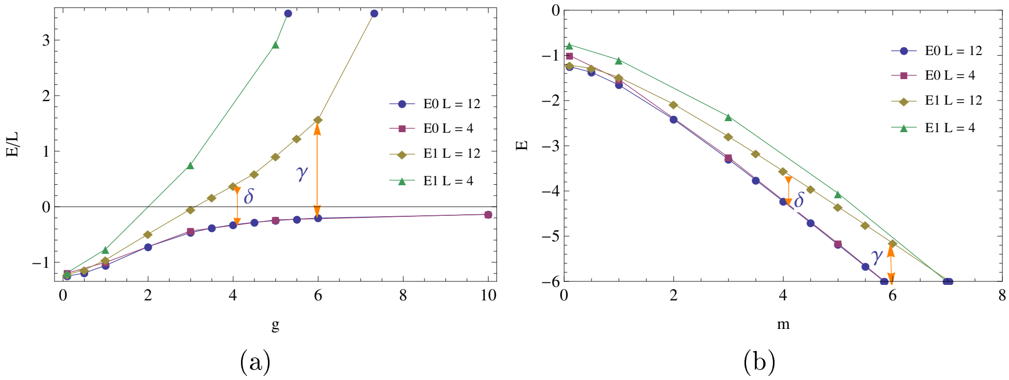

(a) (b)

Figure 4.4.5: Plots of $E0/L$ and $E1/L$ with $L = 4$, $L = 12$ as a function of g with $m = 0.1$ (a) and as a function of m with $g = 0.1$ (b). It is indicated the distance δ between the two levels with $L = 12$ on the corresponding transition point of the phase diagram and the distance γ on a point of the "vacuum" phase.

finite size scaling of δ (distance between the two levels on the corresponding transition point) and γ (distance between the two levels on a point of the "vacuum" phase belonging to the considered lines).

The trends of δ are shown in Fig. 4.4.6a and 4.4.6b. It is clearly visible a decrease of δ when the size increases. Furthemore, the data is in good agreement with a fit of the form $a + b/L$, in which the asymptotic value a (reported in the figures) is very small: this important fact tells us that on a transition point, δ approaches zero when L is very large.

The trends of γ, instead, are shown in Fig. 4.4.7a and Fig. 4.4.7b. In this case, γ increases with the size L and the data are in good agreement with a fit of the same form $a + b/x$, in which however the parameter b is negative and the asymptotic value a (reported in the figures) is large compared to zero.

As a result, when we move in the phase diagram along one of the previous lines, the energy levels tend to a situation, in which the energy gap between E_0/L and E_1/L approaches zero close to the transition point, while it tends to grow considerably in the "vacuum" region.

This behavior may be a sign of the presence of a phase transition between the two regions of our phase diagram. This hypothesis is also supported by the fact that if we consider a generic "transition" point, for example $(m = 3.805, g = 2)$ and perform a finite size scaling of the free energy density,

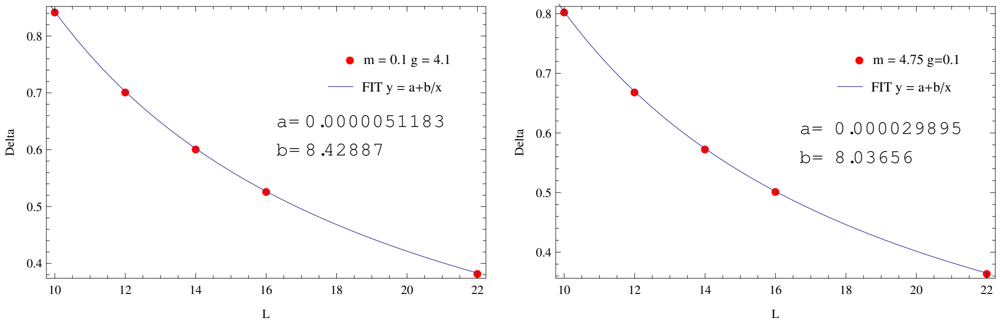

(a) (b)

Figure 4.4.6: Finite size scaling of δ on the transition point relative to vertical lines $m = 0.1$ (a) and on the transition point relative to horizontal lines $g = 0.1$ (b).

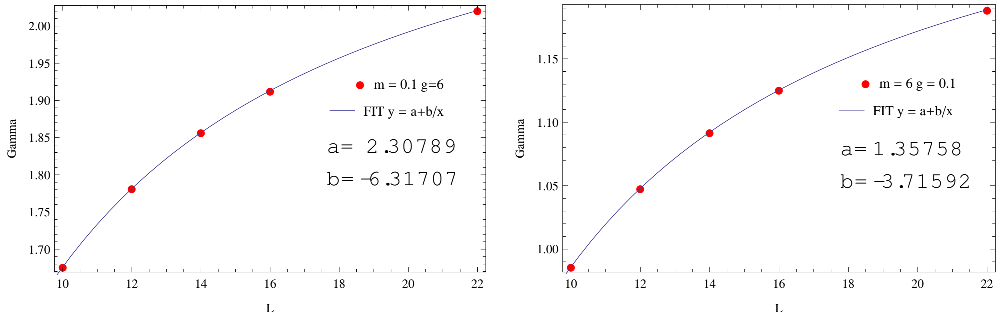

(a) (b)

Figure 4.4.7: Finite size scaling of γ on a point of the "vacuum" phase belonging to the vertical lines $m = 0.1$ (a) and to the horizontal lines $g = 0.1$ (b).

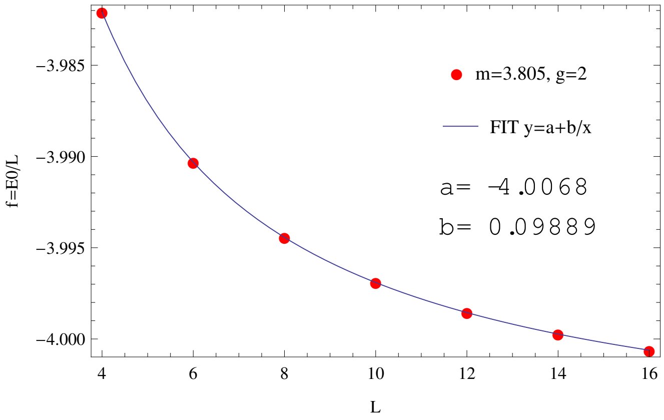

Figure 4.4.8: Finite size scaling of the free energy density $f = E_0/L$ on a transition point of the phase diagram.

evaluated as $f = E_0/L$, we obtain the trend shown in Fig. 4.4.8. It is clearly visible a functional dependence of the type $1/L$, as highlighted by a fit of this form. This behavior is in agreement with a general result for the finite size scaling of the free energy density close to a critical point [16], according to which it results $f_{sin} \sim L^{-d}$, in which f_{sin} represents the singular part of the free energy density and d the dimensionality of the system.

In order to further investigate the system behavior in the passage between the two configurations of our phase diagram, we can proceded in a systematic way: we have chosen in the phase diagram a generic straight line passing through a point (determined previously) of the transition line, as shown in Fig. 4.4.9a. We have fixed on this line a certain number of points, particularly concentrated in the transition zone. For each of these points, we have performed a finite size scaling of the difference δ between the two energy levels E_0/L and E_1/L: the trends, as we have previously seen along the horizontal and vertical lines, are always of the form $a + bL$, in which b results positive in the “meson/antimeson” region and negative in the “vacuum” region. In both cases, from these trends it has been possible to extrapolate the asymptotic value $\delta_{asym} = a$, which represents an estimate of δ for $L \gg 1$ at fixed m and g. At this point, we have plotted δ_{asym} as a function of m ($g = 0.512m + 0.048$) to obtain the trend of the gap between the two energy levels along the considered line in the phase diagram. The result is shown in Fig. 4.4.9b: in the “meson/antimeson” region the gap is very small and it

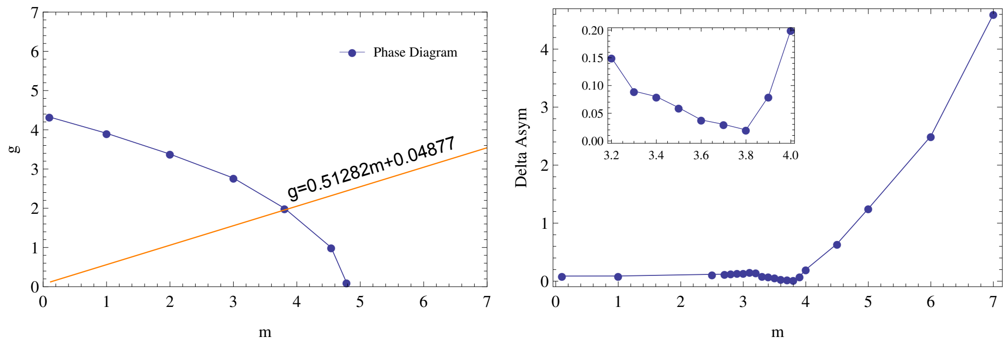

(a) (b)

Figure 4.4.9: (a) The considered line in the phase diagram. (b) Plot of δ_{asym} along the previous lines.

has an almost constant trend; close to the transition point the gap tends to zero, while, once inside the "vacuum" region, it tends to grow considerably. This behavior could be an important clue about the presence of a phase transition between a *critical phase* (with a zero energy gap), here represented by the "meson/antimeson region", and a *gapped phase*, here represented by the "vacuum" region.

We can study now the von Neumann entropy, which is defined as

$$S = -\mathrm{Tr}\left\{\rho \log_2(\rho)\right\} \tag{4.4.2}$$

in which ρ is the density matrix of the system. By using the density matrix decomposition $\rho = \sum_i \lambda_i \left|\psi_i\right\rangle \left\langle\psi_i\right|$ in which $\left|\psi_i\right\rangle$ is one of the basis elements and the quantity λ_i is its probability amplitude in the GS ($\lambda_i \geq 0$ and $\sum_i \lambda_i = 1$), the entropy can be calculated as follows:

$$S = -\sum_i \lambda_i \mathrm{log}_2(\lambda_{\mathrm{i}}). \tag{4.4.3}$$

This quantity takes value between $S = 0$ for a pure state and $S = \ln(d)$, in which d is the size of the Hilbert space of the system, for a maximally mixed state (a superposition of the states $\left|\psi_i\right\rangle$ with uniform probability amplitudes $\lambda_i = 1/d$). Thus, S quantifies the departure of the system from a pure state. In our framework, using the DMRG-algorithm, which computes the density matrix for a block of a fixed lenght, we consider the reduced density matrix

$\rho_{L/2} = \mathrm{Tr}_{i>L/2}\rho$ of the half chain (surrounded by the remaining part of the system) and we evaluate the corresponding entropy as

$$S_{L/2} = -\mathrm{Tr}\left\{\rho_{L/2}\log_2(\rho_{L/2})\right\} \tag{4.4.4}$$

which is also called *entanglement entropy.* In fact, if the half chain is in a maximally entagled state with the remaing part of the system, this quantity assumes large values. Conversely, if the half chain is in a pure state without significant correlations, it tends to zero. As a result, $S_{L/2}$ gives us an estimate of the correlations in the GS of the system.

Clearly this quantity is a function of L. Therefore, we can study this functional dependence adequately to our purpose, by considering again the previous three points of the phase diagram: the first in the "mesons/antimesons" region ($m = 0.1, g = 0.1$), the second on the "transition" line ($m = 3.805, g = 2$), the third in the "vacuum" region ($m = 7, g = 7$).

It results that the entropy on this points shows different behaviors, as reported in Fig. 4.4.10. On the first point we observe a particular growth with L, Fig. 4.4.10c: this trend seems to be logarithmic, but a fit of this type does not show a good agreement. A fit of the form ($a + be^{-|k|L}$), in which a, b, k are three parameters, instead, is in good agreement, showing that $S_{L/2}$ saturates to a finite value. On the second point, altought $S_{L/2}$ is very small, we have observed a logarithmic growth (Fig. 4.4.10a), as highlighted by the logarithmic plot in Fig.4.4.10b. Finally, on the third point we observe a constant trend with a very small value, showing that the GS in this case is almost factorised.

As a result of this, we are in the following situation:

$$S_{L/2}(L) \;=\; \begin{cases} a + be^{-|k|L} & (m = 0.1, g = 0.1) \\ c\log_2(L/2) & \textit{transition point} \\ b & (m = 7, g = 7) \end{cases} \tag{4.4.5}$$

in which a, b, c, k are constant values.

Therefore, the entropy behaves in a different way in the various parts of the phase diagram. This has an important consequence when we consider the case with $L \gg 1$, in which it follows that

$$S_{L/2} \approx \begin{cases} a & (m = 0.1, g = 0.1) \\ c\log_2(L/2) & \textit{transition point} \\ b & (m = 7, g = 7). \end{cases} \tag{4.4.6}$$

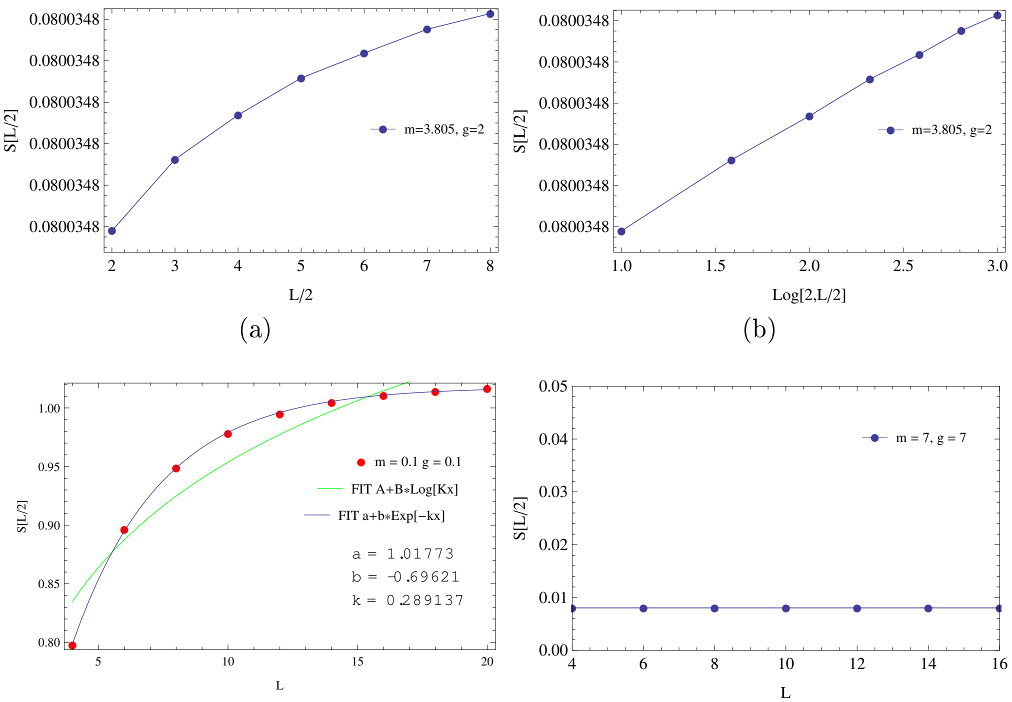

(a) (b)

(c) (d)

Figure 4.4.10: (a) Plot of entropy $S_{L/2}$ as a function of $L/2$ on the “transition” point. (b) Logarithmic plot of the previous quantity (c) Plot of $S_{L/2}$ as a function of L with $m = g = 0.1$. (d) Plot of $S_{L/2}$ as a function of L with $m = g = 7$.

The fact that on the “transition” point $S_{L/2}$ depends on L, in contrast to what happens in the other two regions, may suggest that on this point, when $L \gg 1$, the correlations tend to become increasingly large. This is a typical behavior in proximity to a phase transition. In support of this, we can note that the relation $S_l \sim \log_2(l)$ is a general result for a 1+1-dimensional QFT at a critical point, in which l is the lenght of the considered subsystem [5].
The trend of the entropy in the "meson/antimeson" region ($m = 0.1, g = 0.1$) provides an important starting point for future investigations: in fact, the above analysis on the energetic gap δ seems to highlight the presence of a critical phase, but in this case we should have a logarithmic trend of $S_{L/2}$ in this region instead of a saturation to a finite value. This argument will be deepened by considering a simulation with a greater number of couples and further points in the “meson/antimeson” region.

Chapter 5

Symmetries and final considerations

In this chapter we illustrate the symmetries of the Z_n lattice model for (1+1)d QED and we present some considerations related to the phase diagram and the behavior of the system that we have previously described.

5.1 Symmetries of the model

Consider again the initial Hamiltonian of our lattice Z_n model:

$$H = -t \sum_x^N \psi_x^\dagger U_{x,x+1} \psi_{x+1} + \text{h.c.} + m \sum_x^N (-1)^x \psi_x^\dagger \psi_x + \frac{g^2}{2} \sum_x^N E_{x,x+1}^2. \tag{5.1.1}$$

At this point, considering an even number of sites of the whole chain, we can note that this Hamiltonian is invariant under the parity trasformation (P), the charge-conjugation (C) and the combined trasformation (CP), defined as

$$\begin{aligned} P(\psi_x) &= \psi_{-x} && (5.1.2)\\ P(\psi_x^\dagger) &= \psi_{-x}^\dagger && (5.1.3)\\ P(U_{x,y}) &= U_{-y,-x}^\dagger && (5.1.4)\\ P(E_{x,y}) &= -E_{-y,-x} && (5.1.5) \end{aligned}$$

and

$$\begin{aligned} C(\psi_x) &= (-1)^{x+1}\psi^\dagger_{x+1} && (5.1.6)\\ C(\psi^\dagger_x) &= (-1)^{x+1}\psi_{x+1} && (5.1.7)\\ C(U_{x,y}) &= U^\dagger_{x+1,y+1} && (5.1.8)\\ C(E_{x,y}) &= -E_{x+1,y+1}. && (5.1.9)\end{aligned}$$

and

$$\begin{aligned} CP(\psi_x) &= (-1)^{-x+1}\psi^\dagger_{-x+1} && (5.1.10)\\ CP(\psi^\dagger_x) &= (-1)^{-x+1}\psi_{-x+1} && (5.1.11)\\ CP(U_{x,x+1}) &= U_{-x,-x+1} && (5.1.12)\\ CP(E_{x,x+1}) &= E_{-x,-x+1}. && (5.1.13)\end{aligned}$$

Besides, the initial Hamiltonian, exclusively for $m = 0$, is invariant under the chiral trasformation (χ), which in the context of staggered fermions, is defined as a shift of one lattice spacing:

$$\begin{aligned} \chi(\psi_x) &= \psi_{x+1} && (5.1.14)\\ \chi(\psi^\dagger_x) &= \psi^\dagger_{x+1} && (5.1.15)\\ \chi(U_{x,x+1}) &= U_{x+1,x+2} && (5.1.16)\\ \chi(E_{x,x+1}) &= E_{x+1,x+2.} && (5.1.17)\end{aligned}$$

This transformation preserves all terms in the Hamiltonian except the mass term. Furthermore, it is also explicity broken when one imposes the Gauss'law and considers only the subspace of the physical gauge invariant states: in fact, for example, if we try to trasform under χ the staggered vacuum, we obtain a state with all even sites full and the electric field everywhere zero. This is a non-physical state, for which $G_x \left|\psi\right\rangle \neq 0$.

Another important symmetry of the Hamiltonian is related to the conservation of the baryon number, i.e. the number of quark minus the number of antiquarks. In our framework, we can define a baryon number operator as

$$N_B = \sum_x \psi^\dagger_x \psi_x - \frac{N}{2} \tag{5.1.18}$$

in which N is the number of the sites. In this way, N_B is counted relative to the staggered vacuum and the symmetry is due to the fact that $[N_B, H] = 0$.

5.2 Considerations

Taking into account the results of our numerical analysis, we can introduce now a useful formalism: starting from the Fock vacuum $|0\rangle$, we can express the staggered vacuum as

$$|0\rangle_S = \prod_{x-odd} \psi_x^\dagger |0\rangle \tag{5.2.1}$$

i.e. the state with all odd sites filled.
If we consider the operator $\psi_x^\dagger U_{x,x+1}\psi_{x+1}$ it results that

$$\psi_x^\dagger U_{x,x+1}\psi_{x+1} |0\rangle_S = \begin{cases} |1_{m,x,x+1}\rangle & x - even \\ 0 & x - odd \end{cases} \tag{5.2.2}$$

in which $|1_{m,x,x+1}\rangle$ is a state with a meson on sites $(x, x+1)$. Therefore, we can identify the operators

$$c_{x,x+1}^\dagger = \frac{1}{2}[(-1)^x + 1]\psi_x^\dagger U_{x,x+1}\psi_{x+1} \tag{5.2.3}$$

$$c_{x,x+1} = \frac{1}{2}[(-1)^x + 1]\psi_{x+1}^\dagger U_{x,x+1}^\dagger \psi_x \tag{5.2.4}$$

as creation and annihilation operators of mesons, in which the factor $\frac{1}{2}[(-1)^x + 1]$ is due to the fact that the meson can be created only inside of a couple (even-odd sites).
In the same way, we can note that

$$\psi_{x+1}^\dagger U_{x,x+1}^\dagger \psi_x |0\rangle_S = \begin{cases} 0 & x - even \\ |1_{a,x,x+1}\rangle & x - odd \end{cases} \tag{5.2.5}$$

in which $|1_{a,x,x+1}\rangle$ is a state with an antimeson on sites $(x, x+1)$. Therefore, we can identify the operators

$$d_{x,x+1}^\dagger = \frac{1}{2}[1 - (-1)^x]\psi_{x+1}^\dagger U_{x,x+1}^\dagger \psi_x \tag{5.2.6}$$

$$d_{x,x+1} = \frac{1}{2}[1 - (-1)^x]\psi_x^\dagger U_{x,x+1}\psi_{x+1} \tag{5.2.7}$$

as creation and annihilation operators of antimesons, in which the factor $\frac{1}{2}[1-(-1)^x]$ is due to the fact that the antimeson can be created only between

couples (odd-even sites).
We can analyze now some important properties: the staggered vacuum $|0\rangle_S$ is cleary invariant under P, C and also the combination CP. In fact, if we consider for example the charge conjugation, it results

$$\begin{aligned} C\,|0\rangle_S &= C(\prod_{x-odd}\psi^\dagger_x\,|0\rangle) = C(\prod_{x-odd}\psi^\dagger_x\,|0\rangle + \prod_{x-even}\psi_x\,|0\rangle) \\ &= \prod_{x-odd} C(\psi^\dagger_x)\,|0\rangle + \prod_{x-even} C(\psi_x)\,|0\rangle \\ &= \prod_{x-odd}\psi_{x+1}\,|0\rangle + \prod_{x-even}\psi^\dagger_{x+1}\,|0\rangle \\ &= \prod_{x-odd}\psi^\dagger_x\,|0\rangle = |0\rangle_S\,. \end{aligned} \tag{5.2.8}$$

and the same for P or CP.
Now suppose we consider a state with a meson $|1_{m,x,x+1}\rangle$, x-even. It follows that

$$\begin{aligned} C\,|1_{m,x,x+1}\rangle &= C(c^\dagger_{x,x+1}\,|0\rangle_S) = C(\psi^\dagger_x U_{x,x+1}\psi_{x+1}\,|0\rangle_S) \\ &= -\psi_{x+1}U^\dagger_{x+1,x+2}\psi^\dagger_{x+2}\,|0\rangle_S = \psi^\dagger_{x+2}U^\dagger_{x+1,x+2}\psi_{x+1}\,|0\rangle_S \\ &= d^\dagger_{x+1,x+2}\,|0\rangle_S = |1_{a,x+1,x+2}\rangle \end{aligned} \tag{5.2.9}$$

i.e. a meson on $(x, x+1)$ becomes an antimeson on $(x+1, x+2)$. If we apply again C, it is easy to see that it results $C(|1_{a,x+1,x+2}\rangle) = |1_{m,x+2,x+3}\rangle$, i.e. a state with a meson on $(x+2, x+3)$, and so on. That is, the charge-conjugation is explicated by a shift of one lattice spacing, accompanied by an appropriate exchange of the fermionic operators.
If we consider the parity trasformation, instead, it results that

$$\begin{aligned} P\,|1_{m,x,x+1}\rangle &= P(c^\dagger_{x,x+1}\,|0\rangle_S) = P(\psi^\dagger_x U_{x,x+1}\psi_{x+1}\,|0\rangle_S) \\ &= \psi^\dagger_{-x}U^\dagger_{-(x+1),-x}\psi_{-(x+1)}\,|0\rangle_S = d^\dagger_{-x,-(x+1)}\,|0\rangle_S \\ &= \left|1_{a,-(x+1),-x}\right\rangle \end{aligned} \tag{5.2.10}$$

i.e. a meson on $(x, x+1)$ is symmetrically “reflected” into an antimeson on $(-x-1, -x)$. Clearly, if we apply again P, it follows that $P(\left|1_{a,-(x+1),-x}\right\rangle) = |1_{m,x,x+1}\rangle$, i.e. the initial meson. This tells us that, as we expect, the parity trasformation is explicated by a reflection with respect of the center of the whole chain (the site with $x = 0$).

At this point, we can easily note that if we consider the trasformation CP, we obtain

$$\begin{aligned} CP(|1_{m,x,x+1}\rangle) &= CP(c^{\dagger}_{x,x+1}\,|0\rangle_S) = CP(\psi^{\dagger}_x U_{x,x+1}\psi_{x+1}\,|0\rangle_S) \\ &= -\psi_{-x+1}U_{-x,-x+1}\psi^{\dagger}_{-x}\,|0\rangle_S \\ &= \psi^{\dagger}_{-x}U_{-x,-x+1}\psi_{-x+1}\,|0\rangle_S = c^{\dagger}_{-x,-x+1}\,|0\rangle_S \\ &= |1_{m,-x,-x+1}\rangle \end{aligned} \tag{5.2.11}$$

i.e. a meson on $(-x, -x+1)$. Again, it also results that $CP(|1_{m,-x,-x+1}\rangle) = |1_{m,x,x+1}\rangle$. So, the trasformation CP reflects the state but does not change the meson or antimeson nature.

All these properties allow us to make some qualitative observations about the transition that we have analyzed in the previous chapter: in the "vacuum" region, the GS coindices with the staggered vacuum $|0\rangle_S$, which, as we have shown, is C, P, CP-invariant and clearly has $N_B = 0$ (the number of quarks and the number of antiquarks are both zero).

Now, an important goal would be to understand what are the symmetries of the GS in the "meson/antimeson" region. However, apart from the conservation of the number of particles on the chain which still implies $N_B = 0$, this is not easy because we do not have an analytical expression for the ground-state $|\mathrm{GS}\rangle$. Moreover, even at numerical level, the trasformation P and CP can not be implemented in a simple way, due to their "non-locality" with respect to the space of the single couples that we have considered in our analysis.

On the contrary, we can briefly investigate the behavior of the GS under the charge-conjugation, by using the mean value of the operator C, i.e. the quantity $\langle C\rangle = \langle \mathrm{GS}|\, C\, |\mathrm{GS}\rangle$. Suppose we move in the phase diagram along the bisector $g = m$. The trend of $\langle C\rangle$ (for $L = 5$) is shown in Fig. 5.2.1. As we can see, in the "vacuum" region ($m > 2.86$) $\langle C\rangle$ tends to get closer to one, while when we pass in the "meson/antimeson" region, it decreases. Recalling that if a normalized state $|\psi\rangle$ is invariant under C, it must result $\langle\psi|\, C\, |\psi\rangle = 1$, this behavior may really indicate a spontaneous charge-symmetry breaking. Anyway, this analysis wants to be an indication for further research aimed at a careful study of all the simmetries of GS.

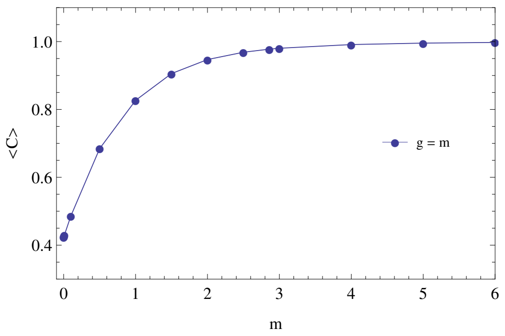

Figure 5.2.1: Plot of $\langle C\rangle$ as a function of m ($g = m$) for $L = 5$.

Chapter 6

Real time dynamics of string-breaking

In this chapter we analyze the real time dynamics of our Z_3 lattice model for QED. In particular, we show that the model exhibits the phenomenon of string-breaking, which is closely related to the phase diagram that we have obtained in the previous chapter.

6.1 String breaking

We have already mentioned the phenomenon of string-breaking in section 3.1.1. We can then summarize by saying that it is a non perturbative phenomenon that quantum electrodynamics in one spatial dimension shares with the quantum chromodynamics (QCD). It consists in a cutting of the electric field string that connects a particle-antiparticle pair by creating a new charge-anticharge pair. For this reason, it is closely related to the confinement, i.e. the impossibility of isolating, in this case, electrons and positrons (quarks and antiquarks in the QCD framework).

In our construction, an electric field string generated by a particle-antiparticle pair is represented by a suitable state, which respects the Gauss'law.

Suppose that the number of couples results $L = 5$: starting from the staggered vacuum, we can construct a string of lenght $l = 5$ (the length of a string is measured according to the number of links with a positive electric field) in the following way:

$$|\psi_{string}\rangle = |5\rangle \otimes |12\rangle \otimes |6\rangle \otimes |3\rangle \otimes |5\rangle \tag{6.1.1}$$

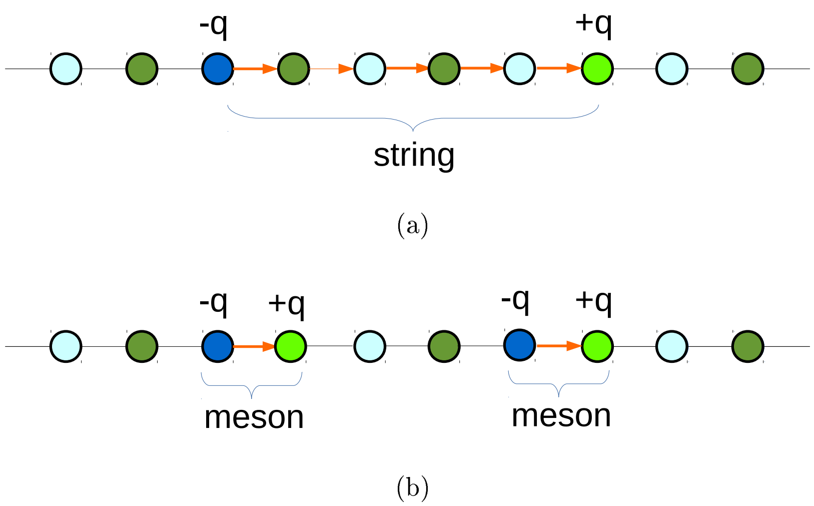

(a)

(b)

Figure 6.1.1: (a) String state of lenght $l = 5$. (b) Meson state with two mesons, which corresponds to the break of the initial string.

in which $|5\rangle$, $|12\rangle$, $|6\rangle$ and $|3\rangle$ are elements of our ordered basis of Fig. 4.1.3. In a static picture, this state is represented in Fig. 6.1.1a, in which we can clearly see how the string is surrounded by the vacuum and how the electric field extends itself between the two opposite charges of the particle-antiparticle pair. This state has an energy

$$E_{string}(l) = E_0 + 2m + \frac{g^2}{2}l \tag{6.1.2}$$

in which $E_0 = -mL$ is the vacuum energy. Instead, a two-mesons state, which can represent the break of the string is shown in Fig. 6.1.1b and has energy

$$E_{mesons} = E_0 + 4m + \frac{g^2}{2}. \tag{6.1.3}$$

In static terms, we can determine the minimal length of the string above which the mesons state is energetically favored over the string state:

$$E_{string}(l_{min}) = E_{mesons} \rightarrow l_{min} = \frac{4m}{g^2} + 2. \tag{6.1.4}$$

So, in order to have the possibility to observe the string breaking phenomenon, we must choose the values of g and m such that l_{min} results smaller

then the lenght of the string that we use for our simulations ($l = 5$).
Starting from this consideration, we can perform a dynamical evolution in the canonical way: if we assume that for $t = 0$ the state of the system results $|\psi(0)\rangle = |\psi_{string}\rangle$, for a generic $t \geq 0$ (here, times are given in units of the inverse of the hopping parameter) it follows

$$|\psi(t)\rangle = e^{-iHt} |\psi_{string}\rangle . \tag{6.1.5}$$

We stress an important property of this evolution: recalling that in our model we must select only the physical states, that respect the Gauss'law, one may wonder whether the evolution of an allowed state, like $|\psi_{string}\rangle$, remains in the physical subspace. The answer lies in the fact that the Hamiltonian (3.2.52) commutes with the gauge operator (3.2.54), as we have seen in the previous sections. Therefore, a physical state always evolves in a physical state, i.e. in mathematical formalism, if $|\psi(0)\rangle$ is a gauge-invariant state such that $T[a_x] |\psi(0)\rangle = 0$, it follows

$$T |\psi(t)\rangle = Te^{-iHt} |\psi(0)\rangle = e^{-iHt} T |\psi(0)\rangle = 0 \tag{6.1.6}$$

so that even $|\psi(t)\rangle$ is a physical state.
This is very importat in our numerical simulation because, having implemented in the program only the physical Hilbert space, we can be sure to reproduce the correct dynamical evolution. Besides, the dynamical gauge-invariance of a physical state remains unchanged even if we perform an expansion of the evolution operator e^{-iHt}.
In order to study the string-breaking phenomenon, starting from the state $|\psi_{string}\rangle$, we have simulated its evolution with a fourth-order expansion of the evolution operator and we have determined the time trend of the mean electric field $\langle E_{x,x+1}\rangle$ on each link. We have repeated the simulation for different values of g and m, considering, in reference to the phase diagram, a point in the meson/antimeson phase ($m = 0.1, g = 1$), a point on the transition line ($m = 1, g = 3.9$) and a point in the vacuum phase ($m = 7, g = 7$). The numerical coordinates of this points have been chosen taking into account that it must be $l_{min} \leq l = 5$. The results are shown in Fig. 6.1.2.
We can notice some importants features:

- when m and g are small, Fig. 6.1.2a, the initial string is clearly broken with a following formation of two mesons, which, surrounded by the vacuum, widen over the entire chain. This corresponds, in our pictorial

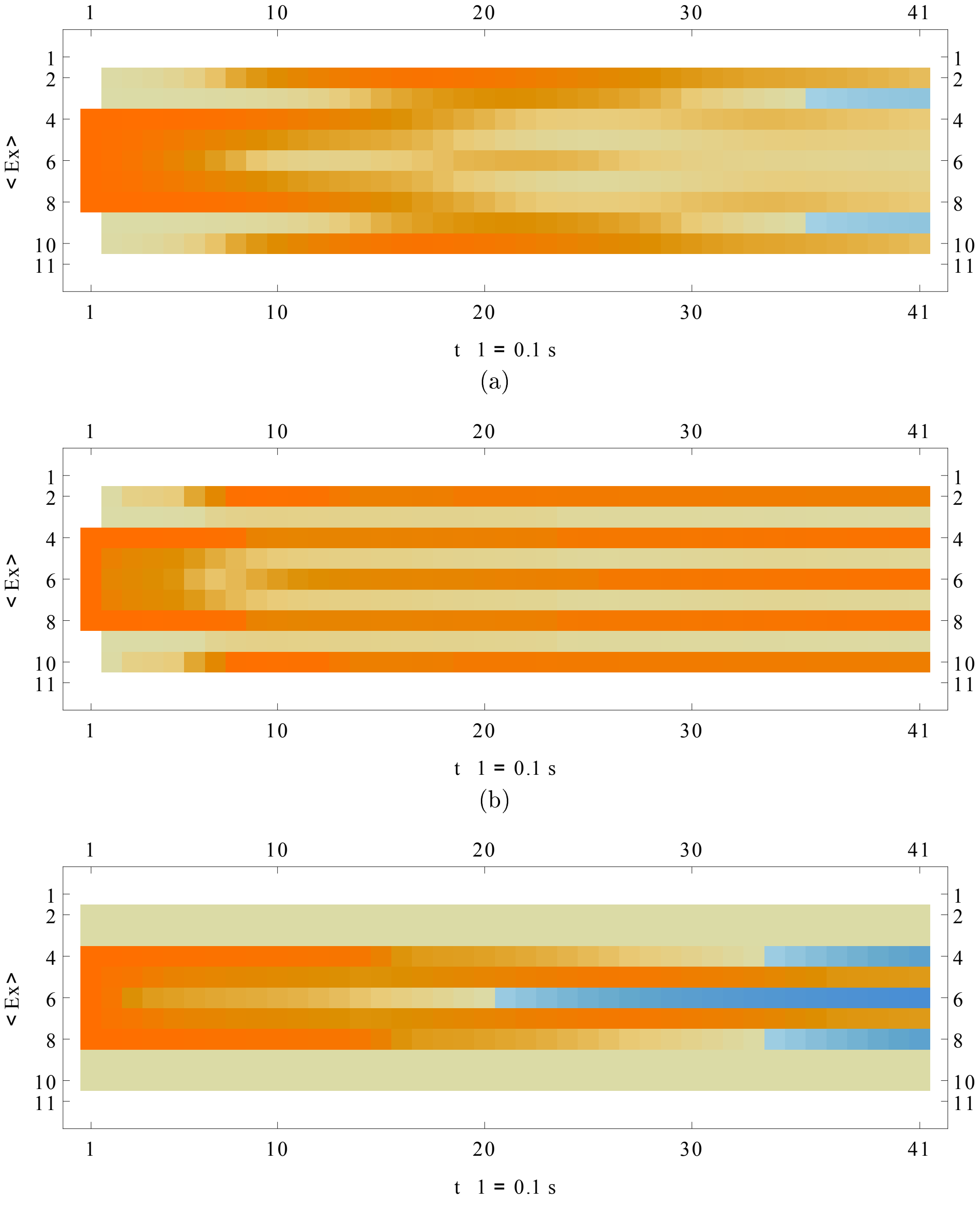

(a)

(b)

(c)

Figure 6.1.2: Time evolution of the state $|\psi_{string}\rangle$ with a string of length $l = 5$ surrounded by the vacuum. In the figures are shown the time trends of the mean electric field $\langle E_{x,x+1}\rangle$ on each link with different values of the parameters m and g. (a) $m = 0.1, g = 1$. (b) $m = 1, g = 3.9$. (c) $m = 7, g = 7$. In all plots zero values are displayed as white, positive values as reddish, negative values as bluish.

representation of the static states, to the passage from the initial string state to a two-mesons state shown in 6.1.1b, by means of a dynamic creation of a new particle-antiparticle pair in the middle.

- when m and g define a transition point of the previous phase diagram, the initial string evolves in a pairs state, i.e. a state in which all the masses are excited forming charge-anticharge pairs. In this case, however, we do not have a clear separation of two mesons in the vacuum, but collective excitations in the whole system.

- when m and g are in the "vacuum" phase, instead, the string has an internal dynamics (the electric fields on links tend to "rotate" between positive and negative values), but it remains strongly confined, as we can see in Fig. 6.1.2c: in this case the large mass and the large coupling constant suppress the string breaking. In fact, if m assumes large values the creation of new particles is completely disadvantaged from the energetic point of view. In the same way, if g is large, the initial string contains too much "electrical" energy, which can not be trasformed in two matter exicitations (recall that the total energy, of course, must be preserved). In addition, large values of m and g suppress the vacuum fluctuations, as we have seen by a static point of view in the previous chapter, so the vacuum between the two initial charge of the string remains stable against particle-antiparticle creation and the string breaking does not occur.

At this point, we can have a qualitative interpretation of the phase diagram of our model from a dynamical point of view: the meson/antimeson phase of our static analysis may be connected to the string breaking phenomenon and consequently we can think of it as a *confined phase,* in which the confinement of the charges exists. Conversely, the vacuum phase may be regarded as a deconfined phase, in which the particles are allowed to exist as free excitations, rather than only within bound states.
We can conclude with an important consideration: we have shown that the Z_3 lattice model for QED is able to capture the confinement of the electrical charges in a given range of the values of the parameters m and g, reproducing in this case the results of the massive Schwinger model for (1+1)d QED. Outside of this range, the vacuum remains stable against particle-antiparticle creation.

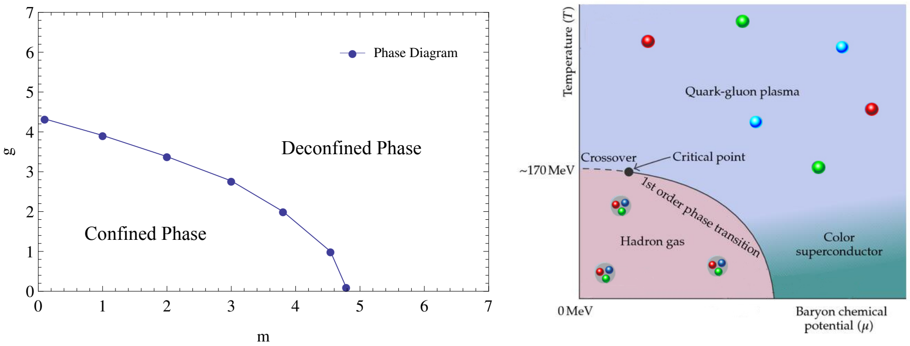

(a) (b)

Figure 6.2.1: (a) Phase diagram of the Z_3 lattice model for QED (b) Phase diagram of the QCD.

6.2 An important outlook

As a result of the dynamical analysis of the previous section, we can consider the phase diagram of Fig. 4.4.2 in terms of a confined phase and a deconfined phase (Fig. 6.2.1a). This is an important and interesting property in order to use a Z_n lattice model to build a quantum simulator (for example with ultracold atoms) able to capture non-quantitative aspects of quantum field theories such as QED or, as a long term outlook, for QCD.

Let us consider the case of QCD: recent studies both theoretical and numerical [23] suggest that the QCD phase diagram exhibits a particular phase transition between confined/deconfined phases with changes in temperature T and in baryion chemical potential μ, as we can see in Fig. 6.2.1b. In the confined phase at low energies, the quarks prefer to form bound states called hadrons, either in the form of three-quarks qqq states called baryons, such as protons and neutrons, or quark-antiquark $q\bar{q}$ states called mesons, like pions. As we increase the temperature, the bound states will eventually break up. Quarks and gluons become weakly coupled due to asymptotic freedom (the coupling constant decreases with increasing energy scale), forming a state called quark-gluon plasma (QGP) [20].

So, even if only qualitatively, we have an important analogy with our model, which, in this sense, could be a good starting point for building a quantum simulator for more general field theories.

In this sense, a further study of the dynamics will be performed for $L > 5$ by using the tDMRG, i.e. the time dependent “version” of the DMRG-algorithm.

Conclusions

In this master degree thesis we have performed a quantum simulation of (1+1)D QED through a Z_n lattice gauge theory. In particular, we have presented an useful construction to implement the model at numerical level.
We have developed a *Mathematica*-algorithm able to engineer the gauge symmetries and to constrain directly the system in the physical subspace. Thanks to an exact diagonalization for small sizes, this program has allowed us to obtain important information on the physical properties of the system and to have a clear interpretation of the results obtained by the DMRG-algorithm (used for larger sizes).
We have identified a suitable order parameter for studying the behavior of the system by varying two important parameters: the mass and the coupling constant. In this way, through a systematic study, we propose a static phase diagram of the model with two different regions: the first ("vacuum phase"), for large values of the previous parameters, in which, as expected, the ground-state coincides with the vacuum, i.e. a state without mass or electric field excitations; the second ("meson/antimeson phase"), for smaller values of the parameters, in which the ground-state is characterized by the formation of mesons and antimesons, i.e. particle-antiparticle pairs with two possible configurations of the internal electric field.
We have studied the stability of our phase diagram by performing a finite size scaling of the order parameter. Thanks to this analysis, we can reasonably expect that the property of the phase diagram remains very similar when we consider very large sizes.
We have analyzed some important quantities such as free energy, energetic gap and Von Neumann entropy, highlighting the possible presence of a phase transition between the two mentioned regions. This analysis represents an interesting starting point for further researches in order to investigate all details of this transition, which, according to the data at our disposal, seems

to involve a critical phase and a gapped phase.

We have studied the symmetries of the model, introducing a suitable formalism in order to show the properties of some important states, such as the staggered vacuum or the meson/antimeson components. Also, we have investigated a spontaneus charge-simmetry breaking in relation to the transition of our phase diagram.

We have performed an implementation of the *Mathematica* algorithm in order to study the real-time dynamics of the system. In particular, we have analyzed the string-breaking, a non perturbative effect, closely related to the confinement, that (1+1)QED shares with the QCD and that usually can not be accessed using classical simulation due to effects of the sign problem. In this framework, we have shown that the Z_n model is able to capture the phenomenon in a range of the values of the previous parameters that corresponds to the "meson/antimeson phase". This gives us, from a dynamical point of view, a qualitative interpretation of our phase diagram in terms of a confined phase, in which the confinement of charges exists, and a deconfined phase, in which the particles are allowed to exist as free excitations.

The implementation of the dynamics at numerical level, which has been performed, represents also an interesting "platform" for the study of other dynamical effects of (1+1)QED (for example, meson-meson scattering, time evolution of exotic states, etc): in this sense, a further study will be performed by using the tDMRG, i.e. the time dependent "version" of the DMRG-algorithm.

Appendix A

Mathematica algorithm

In the section 4.3, we have presented the results of the exact diagonalization of our model for small sizes ($L = 2, 3, 4, 5$). This diagonalization has been performed using an algorithm developed in *Mathematica.*

The core of this program consists in the construction of the Hamiltonian matrix restricted to the physical Hilbert subspace, by using the ordered basis of Fig. 4.1.3, by taking into account the Hamiltonian decomposition of section 4.2 and by considering the fact that when we connect two couples, the right link of the first couple must be equal to the left link of the second couple. This constraint implies that each state of our ordered basis can be connected to only four states (relative to the next couple). For example, the state $|1\rangle$ can be connected to the states $|3\rangle, |6\rangle, |7\rangle, |10\rangle$, the state $|2\rangle$ to $|1\rangle, |4\rangle, |8\rangle, |11\rangle$ and so on for the other states.

For computational purposes it is therefore convenient to insert all this possible couplings between couples in a single matrix that we have called "St":

$$St = \begin{bmatrix} 1 & 3 & 6 & 7 & 10 \\ 2 & 1 & 4 & 8 & 11 \\ 3 & 2 & 5 & 9 & 12 \\ 4 & 1 & 4 & 8 & 11 \\ 5 & 2 & 5 & 9 & 12 \\ 6 & 3 & 6 & 7 & 10 \\ 7 & 3 & 6 & 7 & 10 \\ 8 & 1 & 4 & 8 & 11 \\ 9 & 2 & 5 & 9 & 12 \\ 10 & 1 & 4 & 8 & 11 \\ 11 & 2 & 5 & 9 & 12 \\ 12 & 3 & 6 & 7 & 10 \end{bmatrix} \tag{A.0.1}$$

in each row we have the state of the ordered basis (first column) and its possible couplings on the right.

In this way, in order to construct the physical Hamiltonian, it is possible to perform the tensor products of section 4.2 with the following code (reported for $L = 5$):

```
For[i = 1, i < 13, i++,
    For[j = 1, j < 13, j++,
     For[k = 1, k < 5, k++,
      For[l = 1, l < 5, l++,
             m = St[[i, k + 1]];
             n = St[[j, l + 1]];
          For[u = 1, u < 5, u++,
           For[v = 1, v < 5, v++,
                 e = St[[m, u + 1]];
                 h = St[[n, v + 1]];
            For[p = 1, p < 5, p++,
             For[q = 1, q < 5, q++,
                   r = St[[e, p + 1]];
                   s = St[[h, q + 1]];
               For[alfa = 1, alfa < 5, alfa++,
                For[beta = 1, beta < 5, beta++,
                     delta = St[[r, alfa + 1]];
                     gamma = St[[s, beta + 1]];
```

```
        a = 4*(4*(4*(4*(i-1)+k-1)+u-1)+p-1)+alfa;
        b = 4*(4*(4*(4*(j-1)+l-1)+v-1)+q-1)+beta;

Hph[[a,b]] = Hph[[a,b]] +
A[[i,j]]*B[[m,n]]*C1[[e,h]]*D1[[r,s]]*C2[[delta,gamma]]

]]]]]]]]]]
```

in which Hph is the physical Hamiltonian (for $L = 5$ is a 3072×3072 matrix), initially defined with all elements equal to zero. $A, B, C1, D1, C2$ are 12×12 matrices corresponding to the five operators (one for each couple) of the tensor products which appear in the Hamiltonian decomposition (for example, for the first kinetic term relative to the first couple, it results $A = \mathbb{K}+\mathbb{K}^{\dagger}$, $B = \mathbb{I}$, $C1 = \mathbb{I}$, $D1 = \mathbb{I}$, $C2 = \mathbb{I}$). a and b are respectively row and column indexes: they are calculated using a generalization with five operators of the relations of the tensor product between two matrices[1]. Clearly, the whole cycle is repeated for each term of the decomposition, varying the assignment of the matrices $A, B, C1, D1, C2$.

It can be noted that the algorithm does not perform simply the tensor product between $A, B, C1, D1, C2$ (by doing it, we would go out from the physical Hilbert subspace), but a particular form of it that takes into account only the physical couplings contained in the matrix St. In fact, the indexes (m, n), (e, h), $(r, s,)$, $(delta, gamma)$, relating, respectively, to the second, third, fourth and fifth couple, are calculated taking into account the state of the previous couple in the chain.

More precisely, the process can be viewed in this way: the first couple of the chain can be in anyone of the 12 states of the ordered basis, so the matrix A, which represents the term of the tensorial product relative to the first couple, is entirely evaluated for $i, j = 1, 2, \ldots 12$. When we added the second couple to the right, each state of the initial ordered basis is split in four states, corresponding to the possible couplings that it can form with the states of the second couple. This couplings are represented in the program by the indexes m and n, which, for each i and j, correctly identify the states of the second couple that must be "attached" to the states of the first couple. It is obtained in this way a new ordered basis for the two adjacent couples with

---

[1] Given a $m \times n$ matrix R and a $p \times q$ matrix S their tensor product is a $(mp) \times (nq)$ matrix with elements defined by $C_{\alpha,\beta} = R_{i,j} S_{k,l}$ in which $\alpha = p(i-1) + k$ and $\beta = q(j-1) + l$.

$12 \times 4 = 48$ elements. The corresponding Hamiltonian matrix is then built on this new basis with the product $A[[i, j]] * B[[m, n]]$. At this point, adding to the right a new couple, each state of the basis is split in four elements: in this way, it is obtained a new ordered basis for the three adjacent couples with $48 \times 4 = 192$ elements. The Hamiltonian matrix is then built as $A[[i, j]] * B[[m, n]] * C1[[e, h]]$, by taking into account the correct couplings of the third couple through the indexes e and h. This process is repeated for all following couples in order to construct the Hamiltonian in the physical Hilbert space.

The same algorithm can be used to construct the matrix relative to any observable of the system, such as the electric field on links or the number operator.

Appendix B

DMRG algorithm

The density matrix renormalization group (DMRG) is a numerical variational technique devised to obtain the low energy physics of quantum many-body systems with high accuracy. It was invented in 1992 by Steven R. White and it is nowadays the most efficient method for 1-dimensional systems [36].
One of the main problem in the analysis of a quantum many-body system lies in the dimension of its Hilbert space, which generally grows exponentially with size, making very difficult an exact diagonalization. For example, in the model that we have analyzed in this thesis work, the dimension of the physical Hilbert space grows with the number of the lattice sites N according to the relations $d = 3 \times a^N$ with $a = 2$. The DMRG method allows to reduce the degrees of freedom by a truncation of the Hilbert space, keeping only the most probable eigenstates. This procedure is performed in order to determine a target state of the system, which is generally a good approximation of the ground-state. The process can be also repeated to determine a certain number of excited states, although in this case the accuracy is lower.
In principle, the DRMG algorithm can calculate all ground state properties (energies, correlation functions, etc.) at any temperature and all the observables of the system, although the convergence of these quantities depends on details of the system, such as boundary conditions and dimensionalty.
Suppose we consider our Z_n lattice model on a chain with N sites (N-even). The DMRG algorithm proceeds in the following way.

1. the starting point consists in considering a small "version" of the system, i.e. a chain of lenght l (here, we refer to the number of sites) with an Hamiltonian H_l and a D-dimensional Hilbert space. In the study of our

model, we have setted $l = 8$ and, consequentially, $D = 3 \times 2^8 = 768$. This small "version" of the system is solved exactly;

2. this initial block is expanded by one site to the right. This "new" block of lenght $l+1$ is called *system* (S) and is described by the Hamiltonian H_{l+1}. Clearly it has an Da-dimensional Hilbert space;
3. the system S is reflected in order to form a new specular block, which is called *environment* (E). This new block is attached to S, obtaining a *superblock* which overall contains $2l+2$ sites;
4. it is considered an interaction between the two internal blocks in order to reproduce the interaction between different sites in the original Hamiltonian. In this way, it is obtained an Hamiltonian H_{2l+2} for the superblock;
5. the program proceeds to diagonalize H_{2l+1} and to determine its ground-state $|\psi\rangle$ and the density matrix of the superblock $\varphi = |\psi\rangle \langle\psi|$;
6. in order to extract informations on the system S, its reduced density matrix is calculated as $\rho_S = Tr_E(\rho)$. It is diagonalized, by keeping only the M eigenstates which correspond to the highest eigenvalues (M is an input parameter of the algorithm, called *number of Dmrg states* and, clearly, it must have $M \geq D$ for a good approximation). The same procedure is repeated for the environment, by using $\rho_E = Tr_S(\rho)$;
7. the set of these M eigenstates is chosen as an approximate basis of the Hilbert space of the system S. Its Hamiltonian in this "reduced" space is calculated as $\tilde{H}^S_{l+1} = A^\dagger H_{l+1} A_l$, in which A is the $(Da \times M)$-matrix that contains (as column) the states of the approximate basis. In this way, we obtain an $(M \times M)$ Hamiltonian matrix for the system S. The same is done for the environment, obtaing an $(M \times M)$ Hamiltonian $\tilde{H}^E_{l+1}$;
8. at this point, the system S becomes now the starting block for the whole procedure described, using as initial Hamiltonian $\tilde{H}^S_{l+1}$, which makes the Hamiltonian of the resulting superblock sufficiently small to be diagonalized. Note that, even if the size of S from time to time increases, its Hilbert space is always approximated with an M-dimensional space. This is the core of the DMRG (truncation);

9. the algorithm is iterated until we obtain two blocks of length $(\frac{N}{2} - 1)$ and two sites between them, i.e. a system S and an enviroment E of the lenght $\frac{N}{2}$. For each of these, we have a reduced M-dimensional Hilbert space (with a basis of eigenstates) and a $(M \times M)$ Hamiltonian matrix. During each iteration, the Hamiltonians of the system and the environment and the related basis of eigenstates are stored;

10. at this point, in order to improve the approximation, the first block (on the left) is incremented by one site at the expense of the right block, which is reduced in order to maintain the total lenght of the chain fixed. In this way, we obtain a superblock with fixed lenght N, with a system of lenght $\frac{N}{2}+1$ and an environment of lenght $\frac{N}{2}-1$. Then, the previous steps are repeated. This procedure is called *left-to-right phase.*

11. When the size of the first block is such that the right block can be exactly diagonalized by using M states, the role of the left and right block (and of their Hamiltonians) in the iteration is reversed: the right block starts to grow at the expense of the left block. This procedure, called *right-to-left phase*, finishes when the left block can be exactly diagonalized by using M states.

12. The set of the *left-to-right phase* and the *right-to-left phase* constitutes a *sweep.* Three sweeps are generally enough to have a good approximation.

The computation time of the DMRG-algorithm increases significantly with M: the more states we keep, the better is the approximation but the computational cost can become very high. In our analysis we have used a number of Dmrg states between 2000 and 4000, in relation to the total length of the chain.

Bibliography

[1] A. Aspuru-Guzik, A. D. Dutoi, P. J. Love, and M. Head-Gordon. Simulated quantum computation of molecular energies. *Science*, 309, 2005.

[2] D. Banerjee, M. Dalmote, M. Muller, E. Rico, P. Stebler, U.J. Wiese, and P. Zoller. Atomic quantum simulation of dynamical gauge fields coupled to fermionic matter: From string breaking to evolution after a quench. *Phys. Rev. Lett.*, 109:175302, 2012.

[3] T. Banks, L. Susskind, and J.B. Kogut. Strong coupling calculations of lattice gauge theories: (1+1)-dimensional exercises. *Phys. Rev. D*, 13:1043, 1976.

[4] V. Barone. *Relatività*. Bollati Boringhieri, 2004.

[5] P. Calabrese and Jonh Cardy. Entanglement entropy and quantum field theory. *J.Stat.Mech*, 0406:06002, 2004.

[6] S. Chandrasekharan and U.-J. Wiese. Quantum link models: A discrete approach to gauge theories. *Nucl. Phys. B*, 492, 1997.

[7] Lu D., N. Xu, R. Xu, H. Chen, J. Gong, X. Peng, and J. Du. Simulation of chemical isomerization reaction dynamics on a nmr quantum simulator. *Phys. Rev. Lett.*, 107, 2011.

[8] P.A.M. Dirac. The quantum theory of the electron. *Proceedings of the Royal Society of London. Series A, Containing Papers of a Mathematical and Physical Character*, 117.

[9] U. R. Fischer and R. Schutzhold. Quantum simulation of cosmic inflation in two-component bose-einstein condensates. *Phys. Rev. A*, 70, 2005.

[10] E. Fradkin. *General Field Theory.* University of Illinois at Urbana-Champaign.

[11] K. Fujikawa. Path-integral measure for gauge-invariant fermion theories. *Phys. Rev. Lett.*, 42:1195, 1979.

[12] I. M. Georgescu, S. Ashhab, and Franco Nori. Quantum simulation. *Rev. Mod. Phys.*, 86, 2014.

[13] M. Greiner, O. Mandel, T. Esslinger, T. W. Hansch, and I. Bloch. Quantum phase transition from a superfluid to a mott insulator in a gas of ultracold atoms. *Nature*, 415, 2005.

[14] P. Hauke, D. Marcos, M. Dalmonte, and P. Zoller. Quantum simulation of a lattice schwinger model in a chain of trapped ions. *Phys. Rev. X*, 3:41018, 2013.

[15] F. Hebenstreit, J. Berges, and D. Gelfand. Real-time dynamics of string breaking. *Phys. Rev. Lett.*, 111:201601, 2013.

[16] M. Henkel. *Conformal Invariance and Critical Phenomena.* Springer, 1999.

[17] H.Weyl. *The theory of groups and quantum mechanics.* Courier Dover Publications, 1950.

[18] D. Jaksch and P. Zoller. The cold atom hubbard toolbox. *Annals of Physics*, 315, 1998.

[19] S. Kuhn, J.I. Cirac, and M. Banuls. Quantum simulation of the schwinger model: A study of feasibility. *Phys. Review A*, 90:42305, 2014.

[20] Weicheng Lv. Deconfinement phase transition in qcd. 2008.

[21] F. Mandl and G. Shaw. *Quantum Field Theory.* Jonh Wiley and sons, revised edition, 2001.

[22] D. Marcos, P. Rabl, E. Rico, and P. Zoller. Superconducting circuits for quantum simulation of dynamical gauge fields. *Phys. Rev. Lett.*, 111:110504, 2013.

[23] B. Mohanty. Qcd phase diagram: Phase transition, critical point and fluctuations. *Nuclear Physics A*, 830:889c–907c, 2009.

[24] I. Montway and G. Munster. *Quantum Fields on a Lattice.* Cambridge University Press, 1994.

[25] H.B. Nielsen and M. Ninomiya. Absence of neutrinos on a lattice: Intuitive topological proof. *Nuclear Physics B*, 193:173, 1981.

[26] S. Notarnicola. Quantum simulators for Abelian lattice gauge theories. Master's thesis, Università degli studi di Bari "Aldo Moro", 2013.

[27] S. Notarnicola, E. Ercolessi, P. Facchi, G. Marmo, S. Pascazio, and F.V. Pepe. Discrete abelian gauge theories for quantum simulations of qed. *Journal of Physics A: Mathematical and Theoretical*, 48:30, 2015.

[28] MPI of Quantum Optics. Neue ordnung in der quantenwelt.

[29] E. Peskin and V. Schroeder. *An introduction to quantum field theory.* Addison-Wesley Publishing Company, 1995.

[30] H.J. Rothe. *Lattice Gauge Theory - An Introduction.* World Scientific, third edition, 2005.

[31] J. Schwinger and B.-G. Englert. *Quantum mechanics: symbolism of atomic measurements.* Springer Berlin, 2001.

[32] R. Soldati. *Introduction to Quantum Field Theory.* 2013.

[33] W. O. Straub. *Weyl spinors and Dirac's electron equation.* 2005.

[34] L. Susskind. Lattice fermions. *Phys. Rev. D*, 16:3031, 1977.

[35] A. Trabesinger. Quantum simulation. *Nature Physics*, 8, 2012.

[36] Steven R. White. Density matrix formulation for quantum renormalization groups. *Phys. Rev. Lett.*, 69:2863, 1992.

[37] U.-J. Wiese. *An Introduction to Lattice Field Theory.* Institut fur Theoretische Physik - Universitat Bern.

[38] U.-J. Wiese. Ultracold quantum gases and lattice systems: Quantum simulation of lattice gauge theories. *Annalen der Physik*, 525:777, 2013.

[39] K. Wilson. Confinement of quarks. *Phys. Review D*, 10:2245, 1974.

Acknowledgements

I really thank my supervisor prof. Elisa Ercolessi for the great support, her continuous guidance and for the opportunities given to me during this project.

Thanks to prof. Fabio Ortolani for his competence and availability.

I would like to thank prof. Saverio Pascazio, prof. Faolo Facchi, Dr. Marcello Dalmonte, Dr. Francesco Pepe for the helpful discussions and their precious advice.

Giuseppe Magnifico